Rotational forming of thin SS316L sheets

M. Offerman
2022

madern TU Delft

Cover Image: Creasing and cutting custom-made rotary tool for liquid packaging
Source: https://madern.com/services/rotary/

Rotational forming of thin SS316L sheets

Research into a new rotational forming stainless steel bipolar half plate production method for Proton Exchange Membrane hydrogen fuel cells

by

M. Offerman

A thesis presented for the degree of

Master of Science
Offshore and Dredging Engineering
at the Delft University of Technology,

to be defended on 13 December 2022

Student number:	4728289		
Graduation committee:	Dr. C.L. Walters,	TU Delft,	Committee chairman
	Dr. M. Zeestraten,	Madern,	Company supervisor
	Dr. A. Asgari,	TU Delft,	Committee member
	Dr. J. Jovanova,	TU Delft,	Committee member

Abstract

Bipolar half plates (BPPs) are important parts of Proton Exchange Membrane (PEM) hydrogen fuel cells. Metallic BPPs are generally produced by stamping or hydro forming. However, these processes are not continuous and relatively slow compared to rotary forming. Rotary forming is a continuous process and could potentially be a faster BPP production method.

The BPPs are plastically deformed in bending and membrane modes. It is necessary to determine the bending and membrane strain because differentiating them can aid in the design of future BPP rotary forming production methods. Bending strain predominantly could lead to fractures on the outside of the bend. Membrane strain causes material thinning and could potentially lead to necking. These deformation modes need to be well understood so that the highest forming levels are achieved with a high level of geometrical consistency without exceeding material failure limits.

The goal of this research is to determine the bending and membrane strain of 0.1 mm thick SS316L sheet material formed by rotary forming. This is done by experimental testing and analysis. From the experimentally deformed material, cross-sections are made and analysed. The thickness and bending strain are measured from these cross-sections. The experimental results are compared to FEA simulations.

An important assumption is plane strain and it is experimentally validated. Plane strain FEA models are used to further understand the problem. The FEA simulations are validated, using the single channel strain experiments. Simulations with channels aligned with the cylinder axis are validated with a maximum thickness error of 3%. However, channels perpendicular to the axis are validated with an error of 8.9%. The FEA simulations are then used to further analyse equivalent plastic strain, stress, springback and final shape. The maximum equivalent plastic strain is 0.34. The maximum VonMises stress is 1200 MPa and maximum springback is 0.075 mm. The final shapes along the cylinder axis meet the experimental results the best.

The bending and membrane strain are experimentally measured and simulated in Abaqus CAE. The bending and membrane strain highly depend on channel orientation and indentation depth. However, the bending strain is greater than membrane strain for both experiments and simulations.

This research should be extended to investigate more complex geometries and designs. This is of course a more realistic example for BPPs.

Preface

This report concludes my Offshore and Dredging Engineering Master with a specialisation in Structural Analysis and Design at the Delft University of Technology. My research has been carried out at and under supervision of the research and development department of Madern.

I would like to express my gratitude towards Madern for providing me this opportunity and allowed me to work on this project. Special attention goes towards the graduation committee, in particular Dr. Carey Walters, who introduced me to Madern and this project. Furthermore, I would like to thank Dr. Martijn Zeestraten, who is the head of the R&D department at Madern and my daily supervisor, for his supervision, passion for rotary conversion and all the fruitful discussions we had on this interesting topic. Additionally, I would like to thank Dr. Ali Asgari for his help with Abaqus, determining the mechanical properties and his general addition to my work. Last but not least, I would like to thank Wei Jun, Mohammed and Apostolos for your help, coffee and welcoming me in your office at the Delft university of Technology. Without all your help and insights I would not have been able to solve all the challenges we faced during this project.

I would like to thank my family and friends dear to me, whom unconditionally supported me throughout life, and encourage me to pursue my ideas and dreams. Their tremendous support is invaluable, and for that I am very grateful.

M. Offerman
Rijswijk, September 2022

Contents

List of Tables

List of Figures

List of Symbols

Roman symbols

Symbol	Description	Units
A	Amplitude	[m]
C	Circumference	[m]
C_{cs}	Material constant	[-]
E	Young's modulus	[Pa]
e^-	Negative electron	[-]
f_l	Loading distance	[m]
f_{ul}	Unloading distance	[m]
H_2	Hydrogen	[-]
H_2O	Water	[-]
K_γ	Springback coefficient	[-]
L	Cylinder length	[m]
L_0	Original length	[m]
L_d	Deformation length	[m]
M	Moment	[Nm]
O_2	Oxigen	[-]
P	Force	[N]
P	Material constant	[-]
p	Pitch	[-]
Q	Resistivity	[-]
R	Radius roller	[m]
R_d	Radius die	[m]
R_p	Radius push	[m]
R'	Radius	[m]
r'	Radius	[m]
r_b	Radius bead	[m]
s	Light intensity	[-]
T_d	Deformation time	[s]
T_r	Rotational time	[s]
t	Thickness	[m]
Δt	Change in thickness	[-]
t_0	Original thickness	[m]
t_1	Deformed thickness	[m]
u	In-plane displacement	[m]
v	Web speed	[m/s]
$\vec{X}_{tool}^{i+1}$	Tooling shape	[-]
x	X coordinate	[-]
y	Y coordinate	[-]
y	Distance to neutral axis	[m]
$\Delta\vec{y}^i$	Shape error	[-]

Greek symbols

Symbol	Description	Units
γ	Contrast	[-]
γ_l	Loading angle	[rad or °]
γ_{ul}	Unloading angle	[rad or °]
ε	Mechanical strain	[-]
$\dot{\varepsilon}$	Strain rate	[-]
ε_{eng}	Engineering strain	[-]
ε_{true}	True strain	[-]
θ	Angle	[rad or °]
$\Delta\Theta$	Angle ratio	[-]
$\Delta\theta$	Angle	[rad or °]
ρ	Radius of curvature	[m]
σ	Stress	[Pa]
σ_d	Dynamic stress	[Pa]
σ_s	Static stress	[Pa]
σ_y	Yield stress	[Pa]
Φ	Carrier phase modulation	[-]
$\Delta\Phi$	Carrier phase variation	[-]
ω	Angular velocity	[s^{-1}]

Abbreviations

Abbreviation	Description
ASTM	American Society for Testing and Materials
BBP	BiPolar half Plate(s)
CAD	Computer Aided Design
DA	Displacement Adjustment
DIC	Digital Imaging Correlation
DMA	Dynamic Mechanical Analysis
FEA	Finite Element Analysis
FLD	Forming Limit Diagram
HER	Hollow Embossing Rolling
K&B	Karafillis and Boyce
LSCM	Laser Scanning Confocal Microscopy
PEM	Proton Exchange Membrane
SCO	Surface Controlled Overbending
SDA	Smooth Displacement Adjustment
SPT	Small Punch Test
SS316L	Stainless Steel 316 L
WLI	White Light Interferometry

1 Introduction

1.1 Background

Madern International provides rotary converting solutions for general folding, liquid packaging, and tobacco industries. With their knowledge of rotary converting machines, Madern wants to expand their product lines. As the world is more and more evolving and innovating to become more environmentally friendly, it is looking for fossil fuel alternatives. Hydrogen shows potential as an alternative energy carrier. This means that companies are investing in new and innovative products and production methods for hydrogen conversion and production.

Madern's expert knowledge of rotary conversion production methods and techniques can be reinvented or adapted to serve a growing need of the hydrogen market. Hydrogen conversion happens in fuel cells. "Proton Exchange Membrane" (PEM) fuel cells use bipolar half plates (BPPs) on either side of a membrane to convert hydrogen and oxygen to water. Electricity is produced during this conversion process, and is used to power any process that requires electrical power.

Madern received requests from clients to explore possibilities of metallic BPP production using the rotary conversion process. BPPs are made from thin stainless steel sheets and could possibly be made with a rotary conversion production technique. This is where BPP production meets the expertise and knowledge of Madern and Delft University of Technology. This research is complementing the joint research program between Madern and the Delft University of Technology: Rota-BPP.

Conventional production methods are relatively slow compared to the production rate that could potentially be achieved with "Hollow Embossing Rolling" (HER). In particular, rotary conversion could provide a solution for the production rate. However, rotary conversion is a relatively new production method for BPP production (Porstmann et al., 2020). This means that research still needs to be done, and steps still need to be made in order to implement rotary conversion on an industrial scale.

1.2 Problem definition

BPPs have complex channel geometries. Every PEM fuel cell producer designs and uses its own channel geometry, to specifically meet their requirements. The channels are conventionally cold stamped or hydro formed into a flat metal sheet. Dimensional control, surface finish and geometrical consistency are key challenges for metal BPPs that are produced using conventional production methods. These challenges should also be considered when using the rotary conversion method. Figure 1.1 shows an example of complex BPP geometries.

PEM fuel cells allow a chemical reaction to occur between a cathode and an anode. This chemical reaction can only take place if fuel is allowed to flow through the fuel cells. Therefore, efficient fuel flow is of importance for the fuel cell performance. This means that the BPP surface finishing should minimally influence fuel flow.

The channels are relatively narrow and high, and therefore, material has to bend and stretch significantly to be able to take a desired shape. This means that getting material into a desired shape can bring up challenges. The material failure limit determination follows from geometrical requirements and the material capacity to resist necking or fracture. Thin stainless steel sheets are formed to comply with a design, bearing in mind, the material forming limits. BPPs undergo bending, (deep) drawing and stretching when they are formed and these processes cause stress and deformation. The final deformation shape has an equilibrium between membrane and bending stress in a material. Thus BPP forming leads to strain hardening, plastic and elastic deformations.

This means that if these processes are not managed well or the design is not sufficient, it could lead to failure.

Material deformation happens through bending, (deep) drawing and stretching and these processes cause elastic and plastic deformations. In this case, elastic deformation is called springback, and it causes material to partially form back to its initial shape. Drawing and stretching cause membrane stress and (local) material thinning, which can lead to undesired effects such as necking, fractures and (edge) wrinkling. Therefore, it can be valuable to determine the bending and drawing contributions in this process. Bending and membrane strain are related to springback and plastic deformation. When their separate contributions are linked, it could lead to valuable information for determination of material failure limits and geometrical consistencies.

Rotary conversion is mainly used in the cardboard packaging industry. However, it is not common practise to deform stainless steel by rotary conversion. Especially, the geometry and thickness of the SS316L sheets, that are used as BPPs, could cause complications.

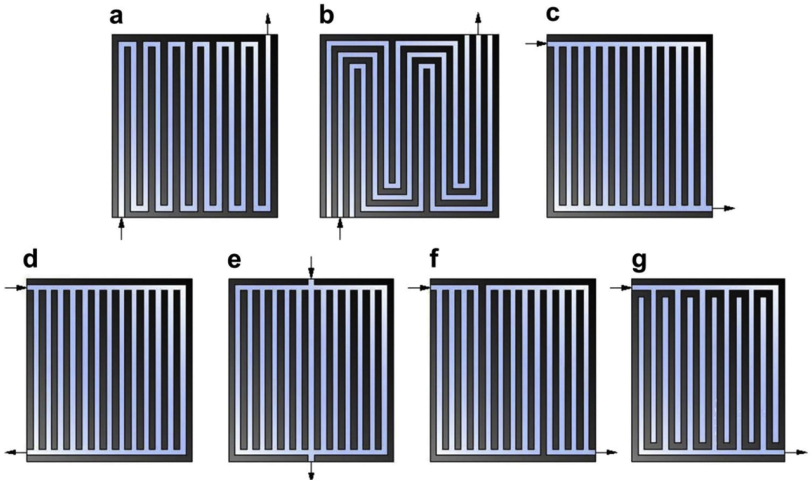

Figure 1.1: *Bipolar half plate geometries (Wilberforce et al., 2019).*

1.3 Objective and research questions

The control, restriction or avoidance of the challenges mentioned in Section 1.2 could be key to further investigate and develop the rotary conversion production method. The final goal is to provide a proof on the concept to implement BPP rotary conversion production method. However, this could take years and is too big a scope for this research. Therefore, the scope of this research is narrowed down to investigating the bending and membrane strain in the BPP production process. The following research question will be answered:

"What are the bending and membrane strain components of a single channel in 0.1 mm thick SS316L sheet formed by rotary conversion?"

To answer this question, special attention is given to the following sub questions:

- What are the main mechanical properties?
- How much thickness strain is experienced during experiments?
- How to simulate the process in FEA?

1.4 Research methodology

This research is separated into two distinct parts. First, a literature review is done to gain a general understanding of the existing research and debates on the topic. Possible gaps in knowledge

and unresolved problems, in which this research may contribute are identified. After the literature review, the research question will be answered by assessing the bending and membrane strain for thin stainless steel sheets.

1.4.1 Part I - Literature review

A literature review is performed towards the assessment of the bending and membrane strain in the rotary conversion BPP production method. The literature review includes:

1. A general explanation of the functions and production methods of BPPs.
2. A description of specific metal sheet forming process.
3. A description of how strain and mechanical properties are determined.
4. A general introduction to springback.

1.4.2 Part II - Determination bending and membrane strain

Research is done towards determining the bending and membrane strain in the rotary conversion of BPPs. This thesis includes:

1. Determination of mechanical properties
   (a) Stress-strain curve
2. Strain and strain rate experienced by the material during forming
3. Assessment of plane strain or plane stress assumption
4. Finite element analysis (FEA) simulation model
5. Experiment rotary forming of stainless steel
6. Validation of FEA simulations

1.5 Thesis outline

This thesis is split up in several chapters with each its own method and objective. Chapter 2 describes this research theoretical foundation. Chapter 3 describes the strain rate calculation and mechanical properties testing. Chapter 4 describes the experiments for plane strain verification and strain measurements. Chapter 5 describes strain and how it is measured. Chapter 6 describes the FEA set-up and validation. Chapter 7 describes the discussions. Finally, the conclusion and recommendations are described in Chapter 8. The thesis outline is graphically represented in Figure 1.2.

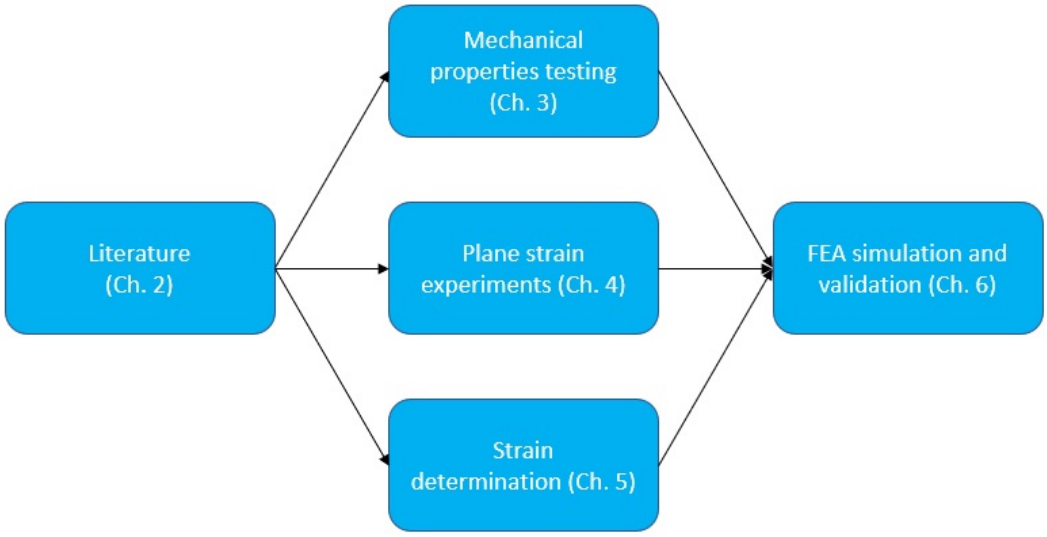

Figure 1.2: *Graphical representation thesis contents.*

2 Literature

The literature review provides insight in available literature and identifies research gaps. This chapter gives a brief explanation of the concept of BPPs and how they are constructed. Furthermore, this chapter provides more insight in metal sheet forming processes, strain measurement, mechanical properties and a brief introduction to springback.

2.1 Bipolar half plate

Researching fundamental principles, requirements and properties of BPPs lead to the identification of critical research areas. Within these research areas benefits, disadvantages and challenges of the new BPP production method can be identified and improved. This section gives a brief explanation of BPP principles, production method, materials and flow field structure and it is explained why rotary conversion could be an improvement.

2.1.1 Principles of BPP

The BPP is an important part of the PEM fuel cell and it has many functions. The most important functions are, distribution of fuel gas and air, heat removal, conduction and leak prevention (Middelman et al., 2003). The hydrogen conversion process depends on many factors, such as temperature, pressure, conductivity and many more. The chemical reaction and transport in PEM fuel cell technology is described in more detail by Berning and Djilali (2003). However, the basics of PEM fuel cell technology is based on a relatively simple chemical reaction shown below:

$$2H_2 + O_2 \longrightarrow 2H_2O \tag{2.1}$$

At the anode side, two hydrogen atoms are split into four positive protons and four negative electrons. At the cathode side, oxygen reacts to positive protons and consumes negative electrons to form water. The anode and cathode processes are shown below:

$$2H_2 \longrightarrow 4H^+ + 4e^- \tag{2.2}$$

$$O_2 + 4H^+ + 4e^- \longrightarrow 2H_2O \tag{2.3}$$

According to Vishnyakov (2006) “The electrolyte, separating electrodes and reactions, should only allow protons to pass which means that electron current flows outside the fuel cell to produce electrical energy.” This means that negative electrons are released and cause an electrical current. This principle is illustrated in Figure 2.1. The generated electrical current could be used to power an electric motor or to charge a battery (Pollet et al., 2016).

Pollet et al. (2016) stated “The PEM fuel cell is one of the most elegant types of fuel cells, which is fed hydrogen, which is oxidised at the anode, and oxygen that is reduced at the cathode. The protons released during the oxidation of hydrogen are conducted through the proton exchange membrane to the cathode. As the membrane is not electrically conductive, electrons released from hydrogen travel along the electrical detour provided, and an electrical current is generated.” This means that the chemical reaction only takes place if hydrogen, oxygen, water and conduction of electricity are managed well.

The BPP mainly functions as a gas distributor for anode (H_2) and cathode (O_2). Furthermore, it provides electrical conduction for the chemical process. Hence, the BPP should have a good

electrical conductivity and low gas permeability. A schematic overview of the chemical reaction is shown in Figure 2.1. Multiple fuel cells are stacked to increase the fuel cell energy density (Pollet et al., 2016).

According to Tsuchiya and Kobayashi (2004) BPPs account for almost 80% of the fuel cell weight. BPPs account for 45% of the total fuel cell production costs. It is expected that, the production costs can be reduced to 37.4% over the years (Tsuchiya & Kobayashi, 2004). However, this research is applied on the current production methods. More cost effective production methods will make a (large) positive impact on the overall fuel cell production costs.

It is expected that rotary conversion or "Hollow Embossing Rolling" (HER) cause quality and durability problems compared to graphite BPPs. Porstmann et al. (2020) raised quality and durability concerns for stainless steel BPPs. However, the main advantage of the HER production method is high production rates. The production rates of HER are much higher than other production methods mentioned by Porstmann et al. (2020). Unfortunately, there are important trade offs for the production processes. This research is written to gain insights in the advantages and disadvantages of the production processes. However, the rest of the research is mainly focused on the HER production method.

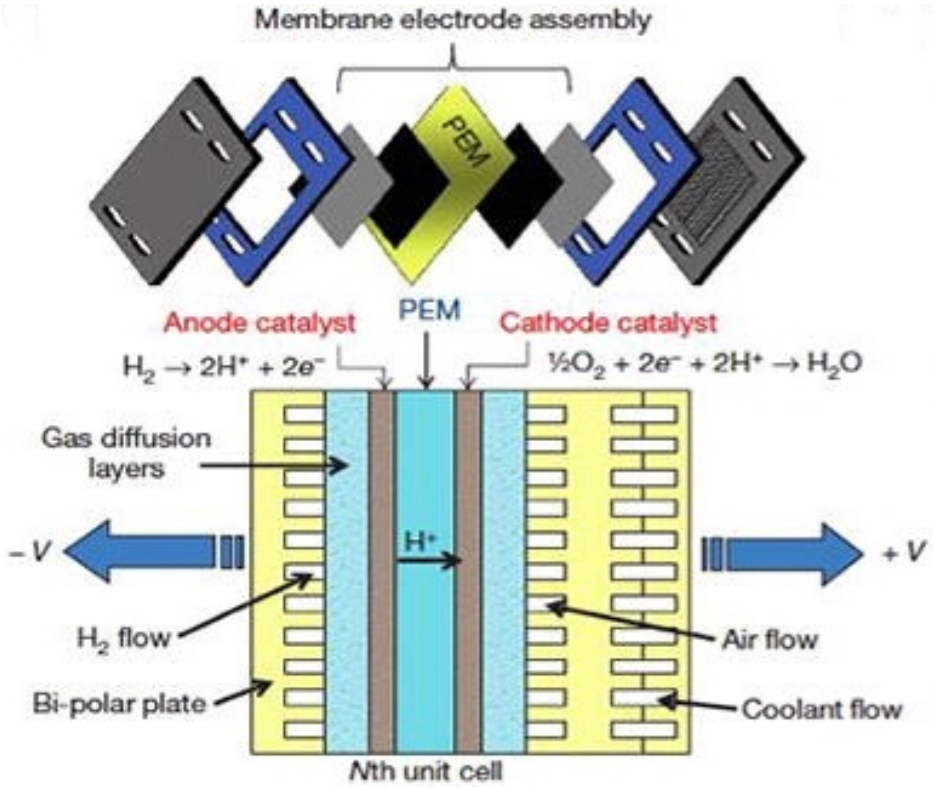

Figure 2.1: *Chemical reaction in a PEM fuel cell (Y. Wang et al., 2020).*

2.1.2 Production methods

BPPs are the main components of a PEM fuel cell, and they account for around 30% of material and production costs (James et al., 2018). If the costs could be reduced, it could lead to an overall cost reduction of the PEM fuel cell production. The overall production cost reduction improves the economical position of PEM fuel cells and could give an impulse to the hydrogen market.

Porstmann et al. (2020) describes and categorises BPP production methods. This production methods overview shows which methods are currently used, and it shows their advantages and disadvantages. In the next sections each production method is elaborated.

2.1.2.1 Hollow embossing

The hollow embossing (HE) process forms metal sheets using two rigid counter dies that are pressed against each other. Often, the sheet metal is clamped on the sides. The metal sheet is deformed by the pressing force of the dies. This is a relatively fast production process when compared to moulding or hydroforming (Porstmann et al., 2020). The HE production process is shown in Figure 2.2.

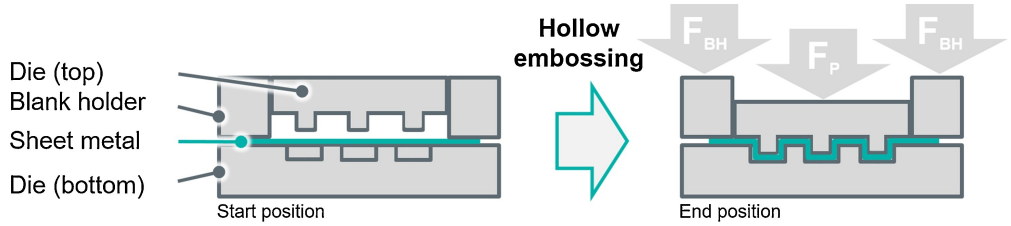

Figure 2.2: *Hollow embossing (Porstmann et al., 2020).*

2.1.2.2 Hydroforming

The hydroforming process forms metal sheets using a pressurised fluid. The base material is placed on a lower mould. Then the upper mould moves down and clamps the base material. After that, a fluid is pumped in the lower die which deforms the base material. Figure 2.3 shows a schematic drawing of the hydroforming process.

The advantage of this process is that the material forming capacity is better utilised. The pressures are distributed evenly over the moulded piece. The disadvantage is that it is a relatively slow process when it is compared to HE (Porstmann et al., 2020).

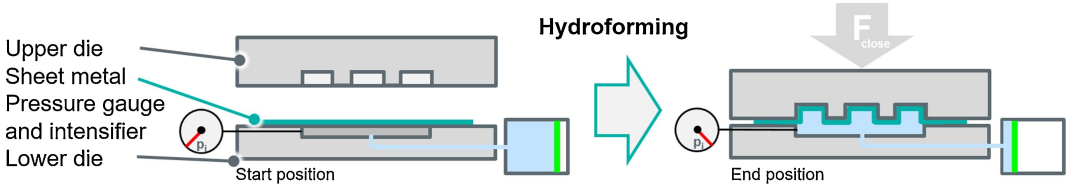

Figure 2.3: *Hydroforming (Porstmann et al., 2020).*

2.1.2.3 Hollow embossing rolling (rotary conversion)

The HER process uses rotating dies that deform base material in a rotating motion. The upper cylinder is often the die and the lower cylinder is the anvil. The die and anvil rotate in the same direction as the metal sheet is moving. With every rotation a part of the metal sheet is embossed. This process is not limited to only one embossed piece per rotation it could be multiple embossings per rotation. The engraving and diameter of the cylinder determine the dimensions of the embossing. Figure 2.4 shows the HER process.

Amongst others Porstmann et al. (2020) states that the HER process is suitable for the BPP production on an industrial scale. Another statement is that if high production rates are of importance then the HER production process shows great potential. However, technical challenges are still yet to overcome. According to Porstmann et al. (2020) “The necessity of reducing unwanted side-effects, such as wrinkling and springback as well as the transfer of the collected knowledge into real geometries with regard to complexity and dimensions represent challenges to be solved and thus the future development potential.”

Bauer et al. (2019) concludes that the forming side effects such as wrinkling and springback are visible for all specimen. However, an improved setup of the numerical analysis shows promising

results in comparison to the computer aided design (CAD) geometry.

Zhang et al. (2017) compares analytical models to experiments for springback and thinning analysis of the HER production method. The analysed models consist of shell and solid elements. Another conclusion was that the model with the shell elements in combination with a small patch of solid elements gave a good representation of the material thinning. However, the full shell model represented the material thinning insufficiently. Overall it was concluded that a model with shell elements and a small patch of solid elements throughout the thickness represents an accurate and cost effective representation of the HER production method.

Abeyrathna et al. (2019) concludes that local material thinning occurs and is greater than predicted by FEA. Local material thinning is related to practical measures such as roll gap, tool alignment, tool inaccuracy and poor surface finishing. The experiments identified potential improvements for the HER production method. However, product dimensions and tool tolerances are very small which could lead to expensive machines and setups.

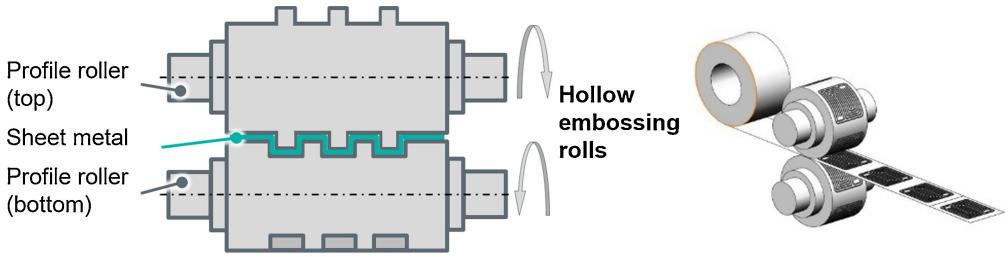

Figure 2.4: *Hollow embossing rolling (Porstmann et al., 2020).*

2.1.3 Material

BPPs are mainly produced from composite based or metallic based materials. Composite based BPPs cannot be produced by rotary conversion (Porstmann et al., 2020). Although composite BPPs exist, they are not researched in this report. This section describes the advantages and disadvantages of metallic BPPs.

Metallic BPPs are lighter and more compact and thus allow for higher density fuel cells. This means that more BPPs can be stacked in a similar sized fuel cell which increases the efficiency (Porstmann et al., 2020). This principle is shown in Figure 2.5.

The main disadvantage of metallic BPPs is that it is less corrosion resistant than graphite BPPs. As Porstmann et al. (2020) stated “Therefore, metallic BPPs are, from an economic point of view, not replaceable by composite BPPs yet, but alternative metal alloys like stainless steel combined with advanced coating systems (graphite coating) tailored for fuel cell use are intensely investigated.” This means that coated stainless steels do not have the same lifetime as the graphite BPPs. When a BPP has a corroded layer on its surface, the BPP electrical resistance increases which influences the fuel cell output in a negative way. Another problem with corrosion is, that the flow in the BPP is disturbed (Metha & Smith-Cooper, 2003).

Another challenge is the reduction of shape deviations on surfaces of metallic BPPs. The surface finish depends very much on the production process (Porstmann et al., 2020).

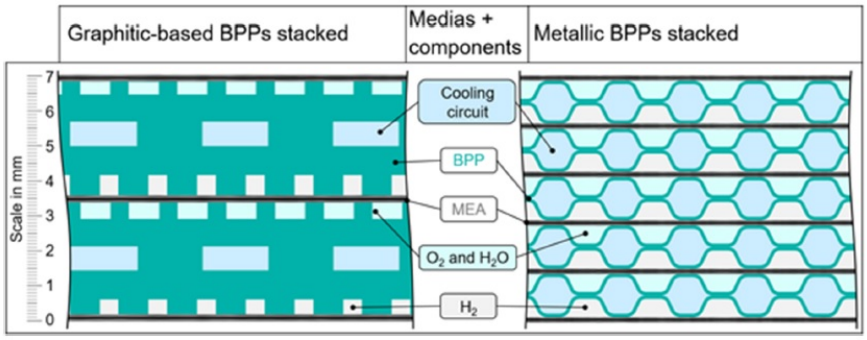

Figure 2.5: *Graphite vs metallic BPP (Porstmann et al., 2020).*

2.1.4 Flow field structure

According to Porstmann et al. (2020) "The flow field design has a significant influence on the performance and the efficiency of the entire fuel cell system, because the specific design of the flow field structures are responsible for the quality of the media transport." Each fuel cell manufacturer has their own flow field design. The fuel cell manufacturers make their own flow field design based on their requirements and restrictions. Table 2.1 shows a schematic overview of possible flow field structures and their advantages and disadvantages.

Table 2.1: *Flow field structures (Porstmann et al., 2020).*

Parallel straight type	Single channel serpentine-type	Parallel or multi-path serpentine-type (with 3 channels)
		
⊕ Low pressure drop ⊕ Possibility of switching the mass flow to neigh-bouring channels ⊖ High risk of failure of reaction surface due to channel blockage (bad water removal abilities)	⊕ Low risk of failure of reaction surface due to channel blockage (good water removal) ⊖ High pressure drop over flow length ⊖ High pressure loss due to obstacles	⊕ Combination of the advantages of purely parallel and meandering river field structures Disadvantages remain similar to the single channel serpentine, but to a lesser extent

2.2 Strain

Strain, amongst other parameters, determines the deformation and failure limits. This section describes what strain is, how strain measurements are done and how they are implemented in this research.

Strain describes quantitatively the degree of specimen deformation. Usually strain is called "engineering strain" or "conventional strain". Uniaxial strain, described by Ling (1996), relates the elongation between engineering strain (ε_{eng}), original length (L_0) and deformed length (L_d):

$$\varepsilon_{eng} = \frac{L_d - L_0}{L_0} \tag{2.4}$$

2.2.1 Strain types

The next three sections discuss three types of strain: thickness, bending and membrane strain. The conservation of volume is considered applicable for all cases and it relates the thickness, bending and membrane strain.

2.2.1.1 Thickness strain

Strain in thickness direction contains either a reduction or a increase in (local) material thickness. Stretching leads to width and thickness reduction and compression leads to width and thickness increasement. The engineering thickness strain is calculated as follows:

$$\varepsilon_{t,eng} = \frac{t_1 - t_0}{t_0} \tag{2.5}$$

where t_1 is the new thickness and t_0 is the original thickness. The engineering strain is converted to true strain with the following equation:

$$\varepsilon_{t,true} = ln\left(1 + \frac{t_1 - t_0}{t_0}\right) \tag{2.6}$$

2.2.1.2 Bending strain

Pure bending causes strain away from the neutral axis. However, the neutral axis is not lengthened or shortened. Bending strain is defined as the maximum surface strain on the specimen outer fibres due to application of a bending moment. The bending strain away from the neutral axis is calculated by:

$$\varepsilon_{ben} = \pm\frac{y}{r} \tag{2.7}$$

where, y is the distance from neutral axis to outer fibre and r is the radius of curvature. The maximum bending strain occurs at maximum y is either positive or negative. If the neutral axis is in the middle of the beam, then the maximum of y is half of the thickness. When y is zero then the bending strain is zero. This equals to strain on the neutral axis.

Hibbeler (2010) describes a relation between internal bending moment and beam curvature. Figure 2.6 shows an undeformed and a deformed beam. In this figure, dx is undeformed length, ds' is strain in the arc, y is distance from neutral axis to outer fibre and is positive from the neutral axis upwards, r is radius of curvature, $d\theta$ is angle of curvature, O' is centre of curvature and M is positive internal bending moment.

The bending strain distribution is linear and symmetric over the specimen thickness. Strain at the neutral axis is zero. For a positive bending moment, the top surface strain is positive and the bottom surface strain is negative. This translates to a tensile strain above the neutral axis and compressive strain below the neutral axis. Bending strain can either be positive or negative according to the convention shown in Figure 2.7.

Hibbeler (2010) adopts a convention, which stated that bending strain, at a positive bending moment, is negative and vice versa. This convention is shown in Figure 2.8.

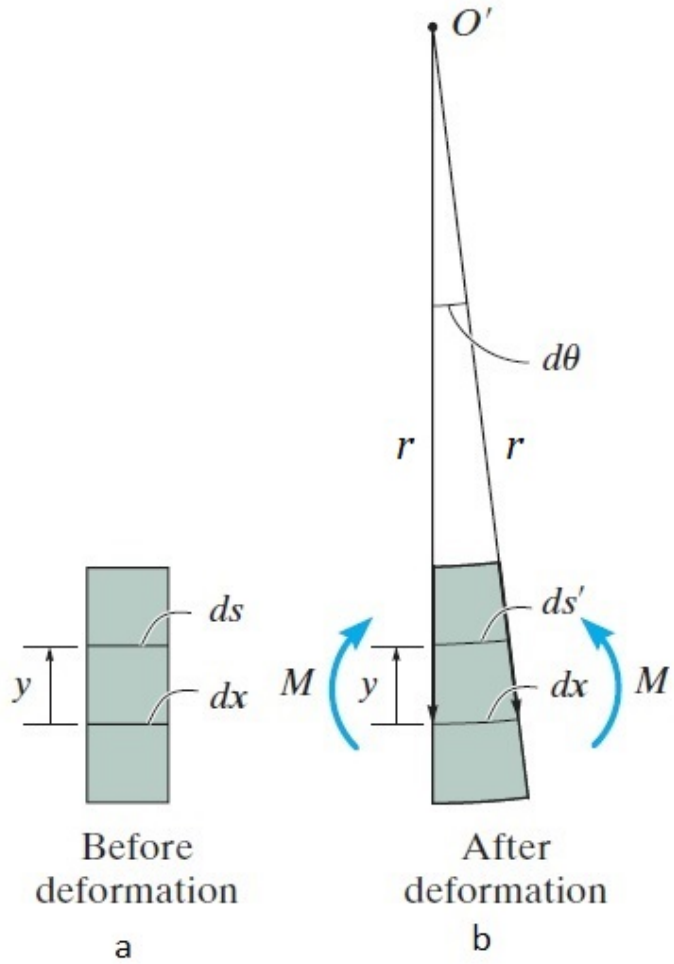

Figure 2.6: *Bending moment: (a) undeformed beam and (b) deformed beam under a positive bending moment (Hibbeler, 2010).*

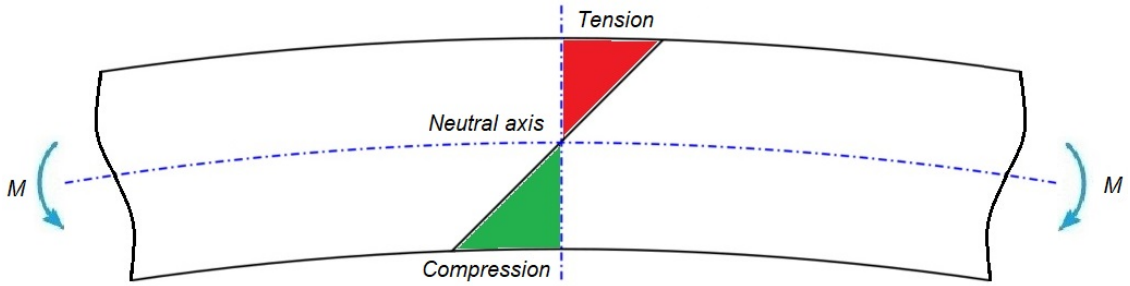

Figure 2.7: *Bending strain distribution for a negative bending moment with above the neutral axis tensile strain (red area) and below the neutral axis compressive strain (green are).*

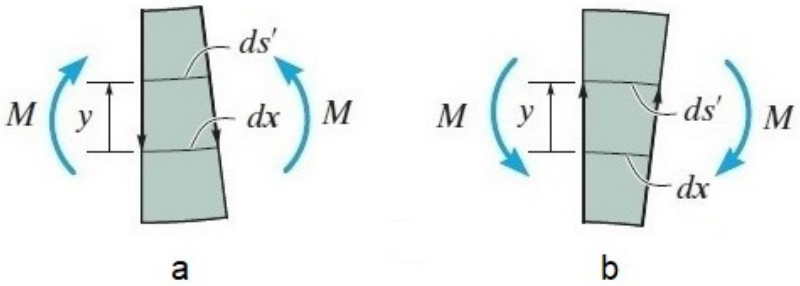

Figure 2.8: *Bending moment: (a) positive bending moment results in negative strain and (b) negative bending moment results in positive strain. Based on (Hibbeler, 2010).*

2.2.1.3 Membrane strain

Strain occurs is three directions length, width and thickness. Strain in thickness direction is already discussed in subsubsection 2.2.1.1. Membrane strain is strain in length or width direction due to material tension or compression. Tension causes width reduction and length increasement and compression causes width increasement and length reduction.

Figure 2.9 shows a specimen subjected to material tension. This causes specimen lengthening and width reduction. If the width reduction occurs locally, it can lead to a local cross-sectional area reduction, which can lead to necking. Figure 2.10 shows the necking principle, where A is the area reduction upon necking. Material is more likely to fail on a neck because the rapid cross-sectional area reduction leads to a rapid increase in stress.

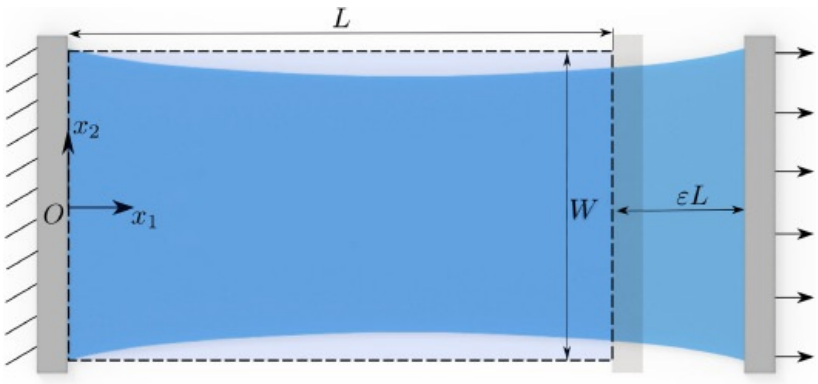

Figure 2.9: *Uniaxial tension leading to membrane strain. Based on (Fu et al., 2019).*

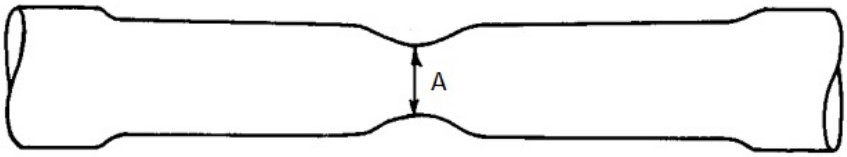

Figure 2.10: *Necking principle (H.Chen, 1971).*

2.2.2 Measurement techniques

Two measurement techniques are discussed in this section. An optical microscope and a confocal chromatography microscope technique.

2.2.2.1 Optical microscope

The optical microscope uses light and one or multiple lenses to enlarge an image. Compound microscopes are the most used microscopes and can magnify an image up to 2000 times. These microscopes use a two lens system which consist of an eyepiece or ocular and an objective (Marques, 2015).

The ability of real colour imaging is an advantage of optical microscopes. As well as that specimen pre-treatment is not necessary before microscopic analysis. Another advantage is that the microscope is fast and adaptable to the specimen size and geometry (Marques, 2015).

The disadvantage is that the optical microscope has a low resolution because of the light diffraction limits. The resolution is in the order of sub-micron or a few hundreds of nanometres (Marques, 2015).

2.2.2.2 Confocal chromatography microscope

The confocal chromatography microscope is a special kind of optical microscope that represents surface imaging in 3D. The 3D imaging can be done with a number of techniques but only two will be discussed in this subsection: Laser Scanning Confocal Microscopy (LSCM) and White Light Interferometry (WLI).

According to Marques (2015) "Both methods are able to measure surface heights from nanometres to millimetres. The biggest difference between these two technologies is the acquisition method. In LCSM only one point is measured at a time and WLI performs a vertical scan along the Z-axis so each point of the surface goes through the focus point and X and Y directions are acquired at each Z-axis step. WLI provides a time effectiveness advantage over other confocal methods by scanning all three axes at the same time." These two methods allow 3D work piece analysis. This is a big advantage over 2D scanning methods and allows measurement in z-direction as well.

2.2.2.3 Thickness measurement

Marques (2015) punched a flat circular form specimen to the form shown in Figure 2.11. After deformation, the specimen is cut along the measurement points in order to perform the thickness measurements. Figure 2.12 shows the cut specimen. Ideally, this is done by wire cutting but it can be cut with a mechanical saw as well. Using the least damaging sawing process is preferred. After cutting the specimen, the thickness is measured with a caliper. Depending on the material thickness, the caliper accuracy should be sufficient. Marques (2015) used a caliper with a 0.05 mm resolution. The thickness measurements should be repeated several times on a number of specimens on multiple measurement points in order to measure the thickness.

Elyasi et al. (2017) cut the specimen with a wire cutting machine. After cutting, the specimen was embedded in clear epoxy resin. The surface was polished to be able to see the profile and measure the profile thickness distribution. The thickness and profile was examined by microscope. Another possibility is to measure and examine the profile channel filling properties. From the cross-section, the profile shape can be examined and compared against the desired shape. Figure 2.13 shows the embedded specimen.

Talebi-Ghadikolaee et al. (2022) described the BPP thickness distribution. Due to variation in metal flow, the thickness distribution deviates from the sides towards the middle. Channels closer to the edge seem to have higher thicknesses, and this happens in longitudinal, transverse and diagonal directions. This is caused by the fact that channels closer to the edge are allowed to draw in more. Channels further away from the edges, are behaving like draw beads for adjacent channels. This causes the thickness distribution to convergence towards the BPP middle. Figure 2.14 shows the thickness distribution over the channels.

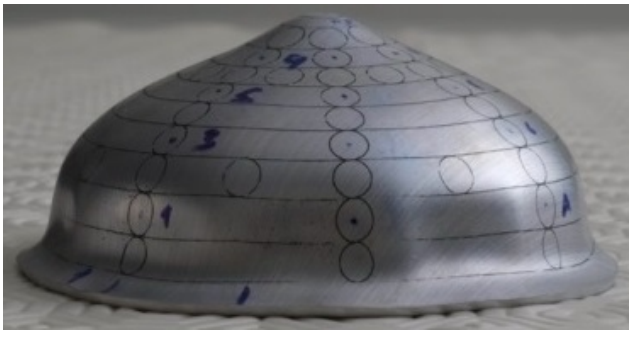

Figure 2.11: *Punched specimen (Marques, 2015).*

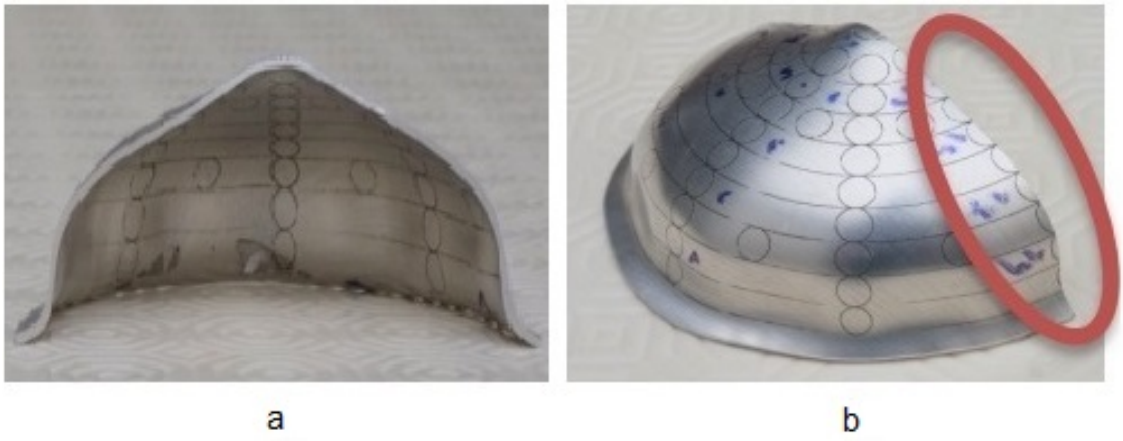

Figure 2.12: *Cut specimen: (a) cross-section and (b) non centred cut due to mechanical saw (Marques, 2015).*

Figure 2.13: *Wire cut cross-section mounted in epoxy (C. Wang et al., 2022).*

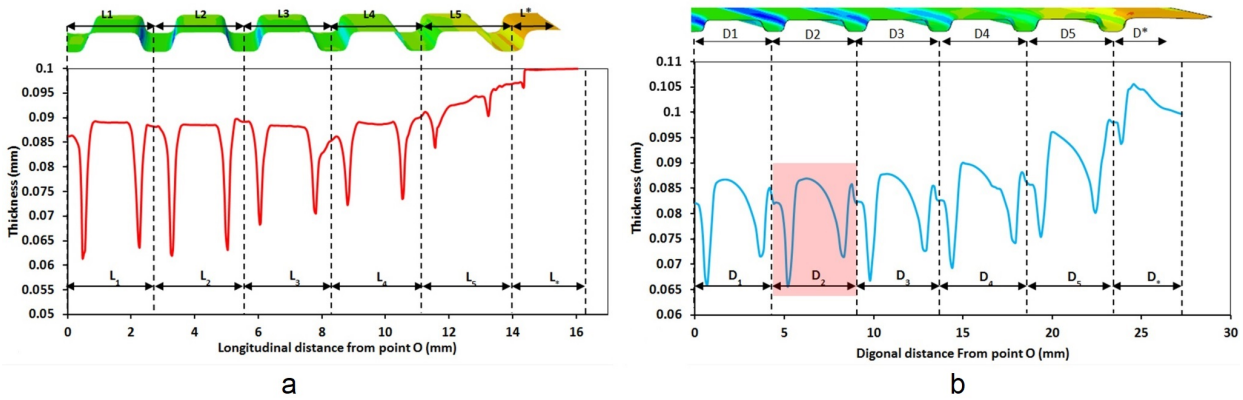

Figure 2.14: *Thickness distribution: (a) longitudinal direction and (b) diagonal direction (Talebi-Ghadikolaee et al., 2022).*

2.2.2.4 Grid

Surface strain can be measured by comparing the initial grid spacing to the deformed situation. In this way surface strain in 2D is measured. However, strain in thickness direction is not measurable with a surface grid.

A grid can be applied in many different ways. For example, engraving, laser etching and many other ways. However, this research focuses on laser etching.

The laser beam etches material from a (flat) surface. For this research, only stainless steel is considered. However, the laser beam can etch any surface material. The laser beam etches a grid on the surface, and with this grid, it should be possible to measure strain.

Figure 2.15 shows the laser etching principles. A (light) source generates a laser beam. The beam is then diverted by a mirror to a lens. The lens focuses the beam onto a surface. The laser beam etches the surface and as the laser head moves across the specimen it creates a grid (Hwang et al., n.d.).

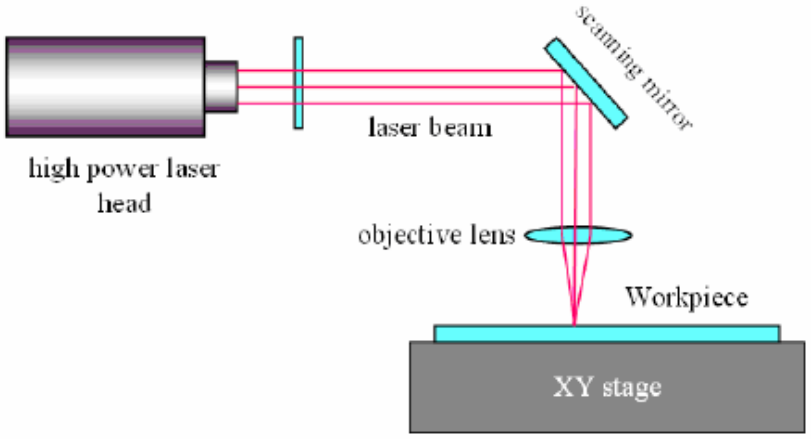

Figure 2.15: *Laser etching method (Hwang et al., n.d.).*

Grid pattern

Grids come in all different shapes and sizes. However, for this research only two patterns are considered. Therefore, this section is split up into two subsections. The first section discusses a circular grid and the second section discusses a square grid.

Circular dots grid

Circulars grid exists of small circular dots or crosses that are etched on the surface. The grid spacing is specific for each work piece. After deformation, a 3D scanned model is made. The 3D model is made using scanning or photographic technology. Then a software program uploads the 3D model and makes a digital grid. The next step is calculating the surface strains and make a forming limit diagram (FLD). This is done by hand or by using special software (Shi & Liang, 2012). In Figure 2.16 the model and digital 3D representation is shown.

The advantage is that surface strains and FLDs are calculated from the digital 3D model. This method is very good for grid and strain visualisation.

The downside is that advanced software and scanning or photographic hardware is necessary. Another downside is that the work piece size is limited by what the scanning or photographic hardware can handle (Shi & Liang, 2012).

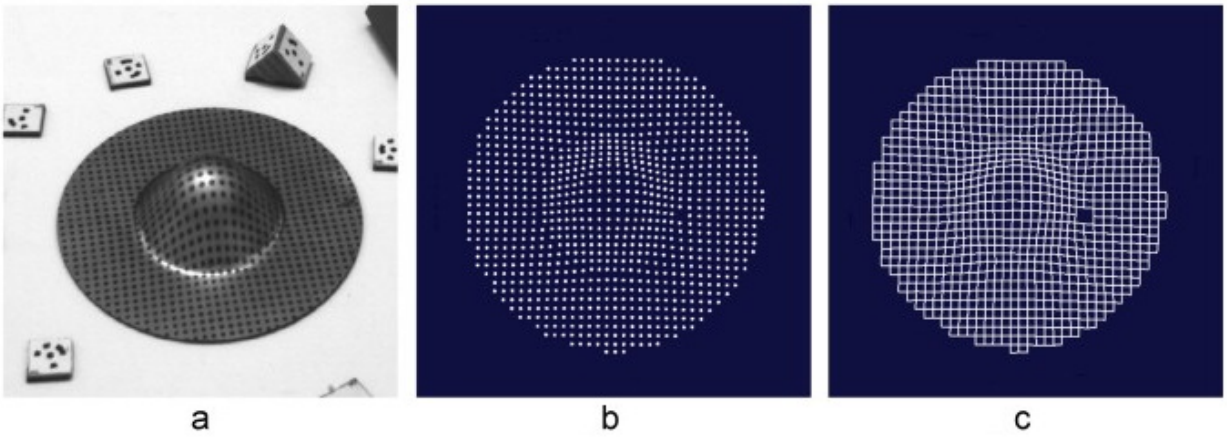

Figure 2.16: *Circular grid pattern: (a) the stamped part, (b) reconstruction of the grid nodes and (c) grid generation (Shi & Liang, 2012).*

Square lines grid
Straight orthogonal lines form squares on the work piece surface. A laser etches horizontal and vertical lines. The line spacing is specific for each work piece. The etch depth is determined by the laser beam intensity and speed. The slower the laser beam, the deeper the etch. The faster the laser beam, the shallower the etch (Mäntyjärvi et al., 2008). Figure 2.17 shows the square grid.

The main advantage is that scanning and conversion to a digital grid is not necessary. The surface strain analysis can be done manually using a microscope. Therefore, advanced software and scanning or photographic hardware is not necessary. On the other hand, it is possible to scan and analyse this grid. The manual work piece analysis is more time consuming. If multiple work pieces are analysed, it can be beneficial to use software and scanning hardware (Mäntyjärvi et al., 2008).

The downside is that damage to the surface is greater than the circular grid. Therefore, the damaged surface should influence the work piece analysis as little as possible. The laser set up should be that it does the least amount of surface damage while ensuring a visible grid. The laser intensity and speed determines the surface damage magnitude (Mäntyjärvi et al., 2008).

Figure 2.18 shows a cross-section of the work piece surface. This work piece is etched by a laser beam, and it shows a typical damage situation to the work piece surface.

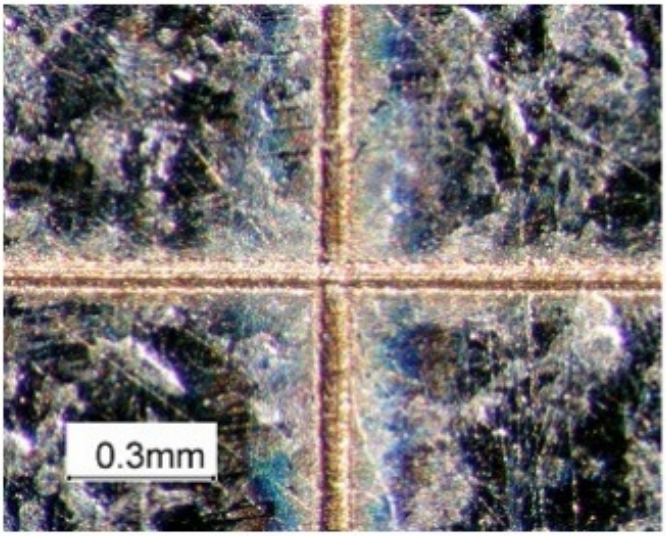

Figure 2.17: *Straight square grid pattern (Mäntyjärvi et al., 2008).*

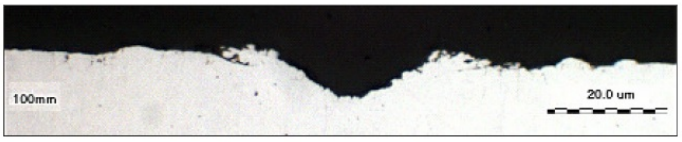

Figure 2.18: *cross-section etch (Mäntyjärvi et al., 2008).*

2.2.3 Strain distribution

Strain can be measured with several different methods. These methods are described in the following subsections.

2.2.3.1 Grid method

Badulescu et al. (2009) describes strain calculation using the grid method. A fringe pattern is applied on the specimen. Then a camera captures the fringe patterns light intensities.

Strain is derived from displacements according to four steps. Firstly, initial and final phase distributions are determined from the fringes. This is done by spatial or temporal phase shifting

procedures. Secondly, phase difference and displacements are deduced. Thirdly, the displacement field is spatially filtered. Finally, the spatially differentiated displacement field is numerically differentiated (Badulescu et al., 2009).

According to Badulescu et al. (2009) the last two steps can be merged together by using a derivative filter. The strain distribution can be determined directly from the fringe pattern. Several numerical models are designed to determine the strain. These numerical models are described in more detail by Sciammarella and Kim (2003).

2.2.3.2 Automated grid method

Sirkis and Lim (1991) describes an image processing automated grid method to determine strain and displacement. This technology uses solid state video technology and pattern recognition software. The grid used by Sirkis and Lim (1991) exists of circular spots that are placed at a predefined distance from each other. Figure 2.19 shows the grid on the specimen.

The process is described by Sirkis and Lim (1991) "A charge coupled device video camera and a personal-computer-based image-processing system are used to digitise the spot locations after each deformation increment. The spots are located with a histogram-based grey level threshold and their precise positions are found using a centroid algorithm. Each spot is uniquely identified in each of the sequence of images by the spot position relative to its neighbours." This means that the camera takes pictures at set intervals and captures the specimen deformation. Then, the position of each spot is determined. In the end the grid deformation leads to the specimen strain.

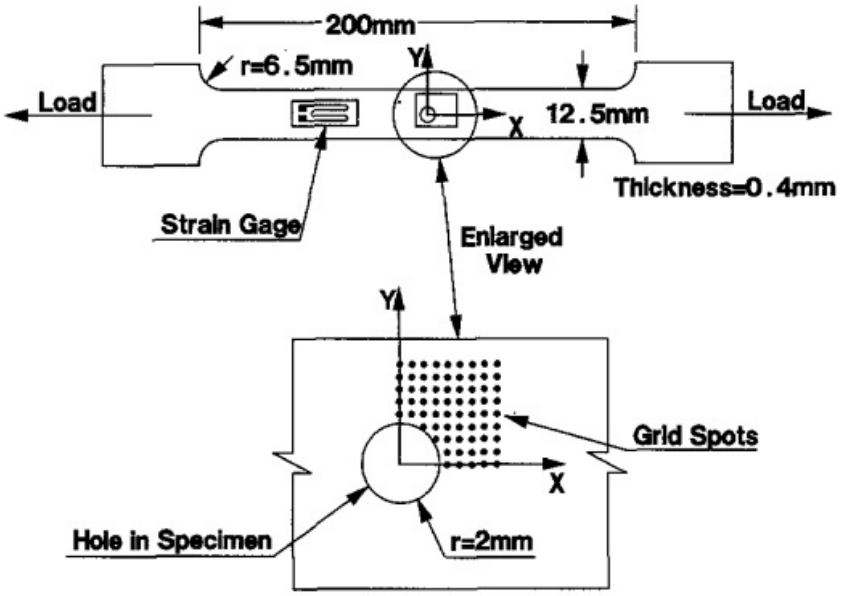

Figure 2.19: *Perforated strip with grid (Sirkis & Lim, 1991).*

2.3 Metal sheet forming

There are many sheet metal forming processes and they have their challenges and limits with regards to bending, drawing and stretching. During metal sheet forming all sorts of processes happen inside the metal. These processes are well described for conventional BPP production processes. However, it requires more research for rotary conversion BPP production. This section describes the processes in thin sheet metal forming.

2.3.1 Definition of sheet metal forming

Banabic et al. (2000) describes sheet metal forming as a combination of bending and drawing. Whereby drawing is split up into stretching and deep drawing. This is elaborated in the following sections. Figure 2.20 shows the processes in diagram form.

Marciniak et al. (2002) describes more common metal forming processes. These processes are blanking, piercing, bending, stretching, hole extrusion, stamping, (deep) drawing, coining, ironing, tube and fluid forming. However, these forming processes are very complex but they all make use of a few elemental operations. These operations are stretching, drawing, bending, bending under tension and sliding over a tool. Each basic operation process can be analysed and described by a "mechanics model" (Marciniak et al., 2002).

It would take an enormous amount of time to describe all forming process variations and details. Therefore, the next two sections describe only the fundamental operations behind these processes.

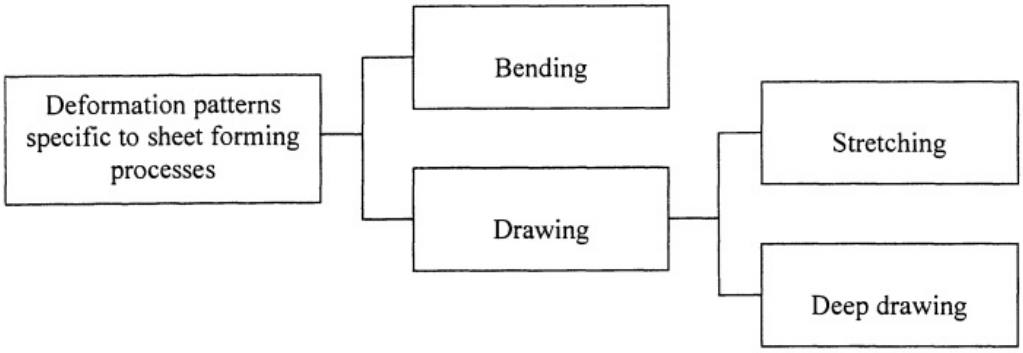

Figure 2.20: *Metal sheet forming diagram (Banabic et al., 2000).*

2.3.2 Bending

Bending is material forming by bending it into a desired shape. This can be done in many forms but for this research it is categorised in two operations, pure bending and stretch bending. The pure and stretch bending operations are described in the next following subsections.

2.3.2.1 Pure bending

Figure 2.21 shows an pure bending example where a sheet is bent over a straight line. Plastic deformation only occurs in the bend region, and material away from the bend is not affected or deformed. If the material is not ductile enough, cracks can occur on the outside of the bend (Marciniak et al., 2002).

The bend region contains partially plastically and elastically deformed material. The elastic part causes the final bending angle to reduce after bending. This phenomenon is called "springback" because the material partially springs back into its original shape. Springback will be elaborated in Section 2.5. Therefore, the determination and consistency of bending angles can be difficult (Marciniak et al., 2002).

Figure 2.22 shows examples of pure bending techniques that are used in the metal sheet forming processes. The pure bending formability limit is expressed as the bending angle upon fracture occurrence. This is the maximum bending angle before the specimen is classified as failed. The maximum bending angle is always larger than the final angle of the specimen. This is due to springback (Banabic et al., 2000).

Banabic et al. (2000) performed a standardised test to determine pure material bending. Figure 2.23 shows the test used by Banabic et al. (2000).

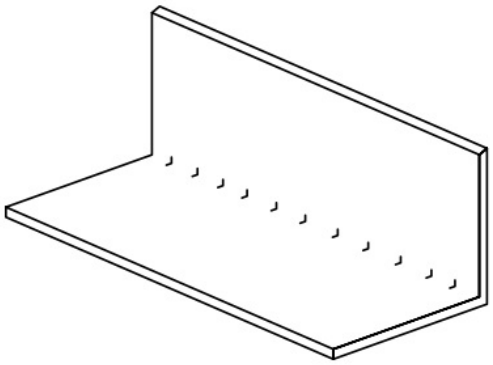

Figure 2.21: *Straight bend (Marciniak et al., 2002).*

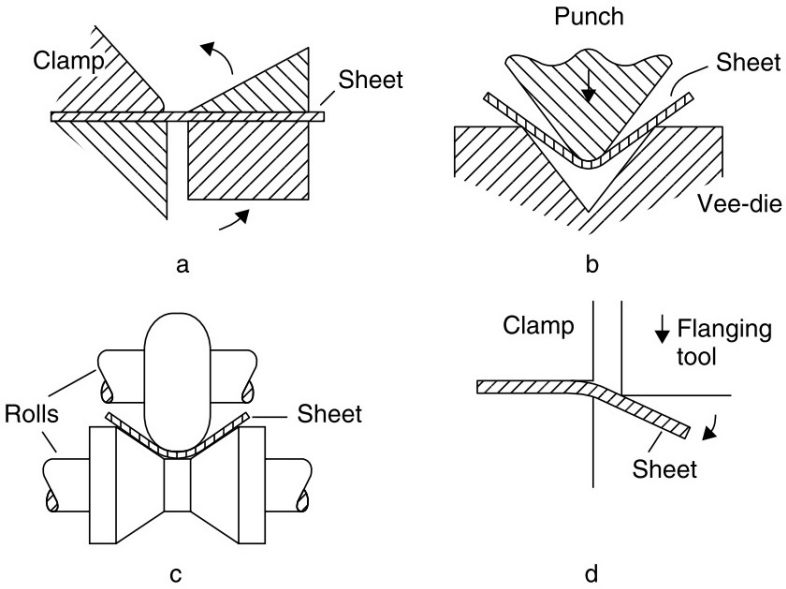

Figure 2.22: *Variations of pure bending: (a) folding machine, (b) press brake bending, (c) roll forming and (d) flange wiping (Marciniak et al., 2002).*

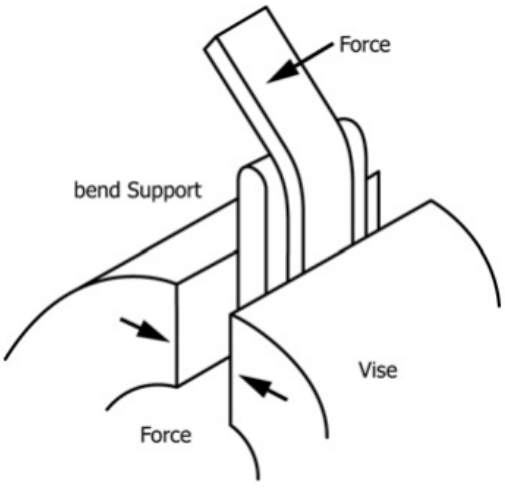

Figure 2.23: *Semi-guided bend test of thin specimens: ASTM E 290 ("ASTM E290-14", 2019).*

2.3.2.2 Stretch bending

Bending and stretching are now combined. This means that, both material in the bend area as material away from the bend area is affected by plastic deformation. Ueda et al. (1981) researched bending of channels and noticed mainly three problematic areas: springback, undesirable sectional shape deformation and flange buckling.

The stretch bending forming limits can be determined using the stretch bend test described by Demeri (1981). Lock bead fix the material in place. Lock or draw beads make sure material cannot draw inwards. This means that material is not only subjected to bending. The test purpose is to measure the punch depth at maximum force. Test results are highly dependent on punch radius and sheet thickness (Banabic et al., 2000). Figure 2.24 shows the stretch bend test.

Lock beads can fix material, but it can also be held in place by a blankholder that applies a certain force or pressure on the specimen sides. This allows material to stretch and draw in up to a certain degree. However, controlling this process is difficult, as it relies on force or pressure and friction.

Marciniak et al. (2002) shows that shrink and stretch behaviour occur for bending curved sheets or bending a curved sheet over a straight line. A flat sheet that is bent with a positive radius, shows flange shrinkage. For negative bending radius, the flange shows stretching. A double curved sheet can show both flange stretching and shrinkage. Figure 2.25 shows this principle.

Gu et al. (2016) researched stretch bending of a stainless steel Z-profile. The Z-profile is bent over a radius of 3000 mm and simultaneously stretched by 10% of its original length. They identified serious section distortion in the form of: flange sagging, sidewall obliquing inward and bottom plate upwarping. However, stretch bending reduces springback a lot of undesirable distortion was introduced. Figure 2.26 shows the introduced distortions of the Z-profile after stretch bending. Conservation of volume implicates the cross-sectional area has to reduce due to overall profile stretching. This caused profile distortion, where the side wall shrinkage had the most influence.

A lot of research is done to understand and investigate what causes stretch bending for metal sheet forming processes. However, not a lot of research is done to understand the contribution of bending and membrane strain. Rotary conversion introduces bending and membrane strain into formed steel, which cause undesirable side effects such as distortion and springback. Therefore, it could be beneficial to understand what the bending and membrane strain does to optimise the reduction of unwanted side effects.

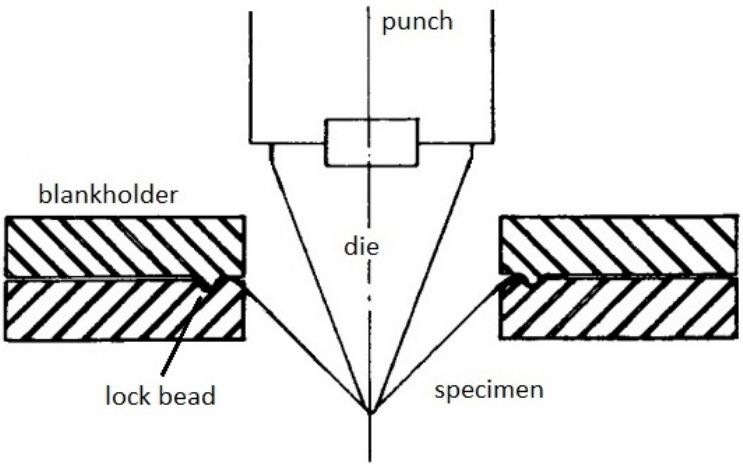

Figure 2.24: *Stretch bend test (Demeri, 1981).*

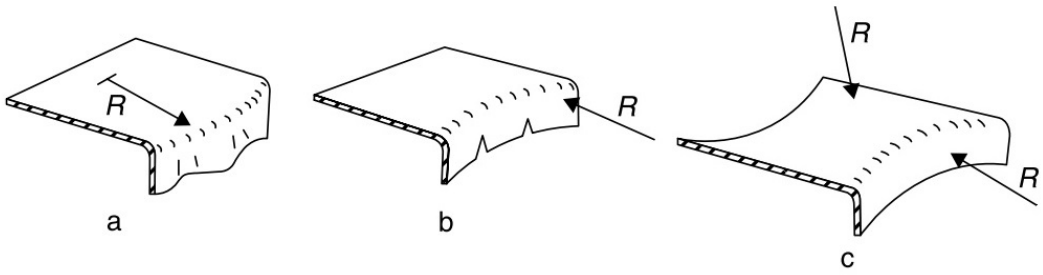

Figure 2.25: *Variations of stretch bending: (a) shrinking flange, (b) stretch flange and (c) flange on a curved sheet (Marciniak et al., 2002).*

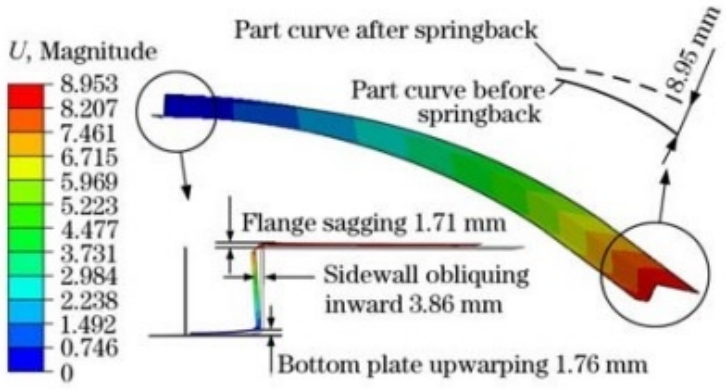

Figure 2.26: *Z-profile stretch bending (Gu et al., 2016).*

2.3.3 Drawing

Draw die forming or stamping shapes material by stretches material over a die while allowing the material to draw in from the sides. This means that there is a balance between drawing and stretching. Figure 2.27 shows the drawing principle.

There are many forms of drawing, but for this research, it is specified and split up into two operations, stretching and deep drawing. These two operations are elaborated in the next two subsections.

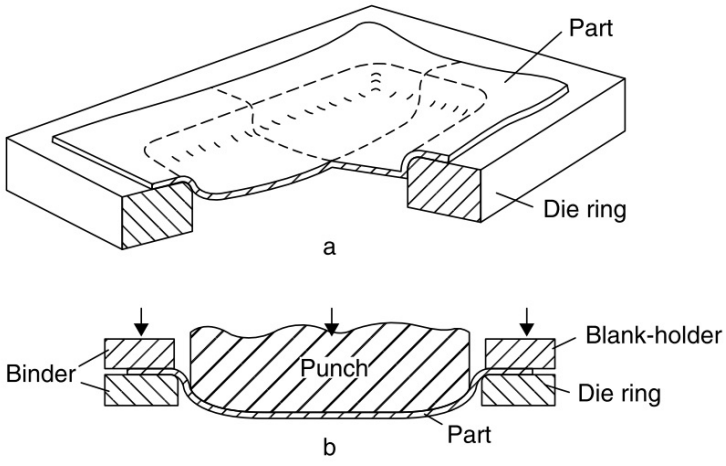

Figure 2.27: *Schematic representation of the drawing process: (a) typical part formed over a die ring and (b) section of tooling drawing (Marciniak et al., 2002).*

2.3.3.1 Stretching

Banabic et al. (2000) explains material stretching as both a positive strain in the major as well as in the minor strain direction ($\varepsilon_1 > 0$ and $\varepsilon_2 > 0$). Whereby ε_1 is major strain and ε_2 is minor strain.

A punch pushes into a specimen with a force. The punch stretches the material and with this action generates tensile stress and or strain. The forces cause the specimen to deform. The contact stress between the punch and the specimen is much lower than the material yield stress (Marciniak et al., 2002). Figure 2.28 shows a very simplistic stretching process form.

The Erichsen test can be used to measure and express stretch forming limits. In 1914, Erichsen performed a thin steel sheet forming limits test described by Erichsen (1914). A punch pushes into a specimen, and the punch depth is measured in millimetres. The Erichsen index expresses the punch depth.

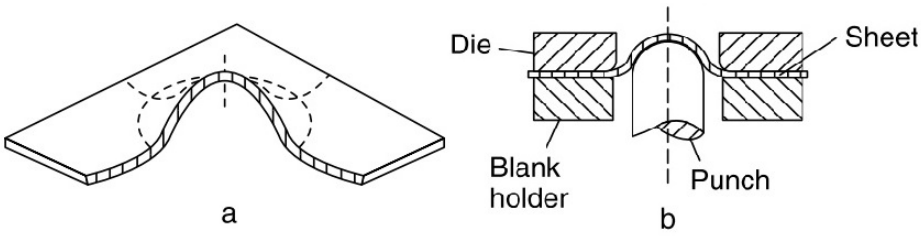

Figure 2.28: *Pure stretch punch: (a) stretched specimen by a dome and (b) schematic drawing of punch stretch set up (Marciniak et al., 2002).*

2.3.3.2 Deep drawing

Banabic et al. (2000) explains deep drawing as a positive strain in major strain direction and a negative strain in minor strain direction ($\varepsilon_1 > 0$ and $\varepsilon_2 < 0$). Parts that are formed by drawing are mostly shallow parts. Therefore, to form deeper parts, the material should be drawn inwards more than in “normal” drawing. Figure 2.29 shows the forming of a simple cup.

The blankholder function is to limit the draw-in amount and prevent flange buckling. The blankholder clamps down on the flange with a force of the same order as the punch force (Marciniak et al., 2002).

Lubrication between die and material is important because material should be allowed to flow or draw in from the sides. If friction is too high, the material cannot draw in and material discontinuities could occur. Friction should be low in order to optimise the process. This is to minimise extra edge deformation and stress (Marciniak et al., 2002).

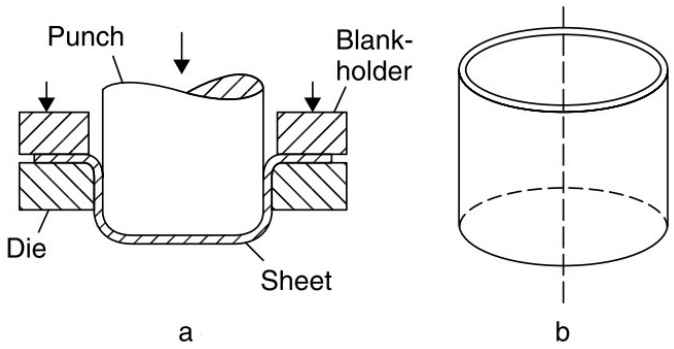

Figure 2.29: *Deep drawing punch: (a) section of deep drawing tooling and (b) drawn cup (Marciniak et al., 2002).*

2.4 Mechanical properties

This section described how SS316L mechanical properties are measured from literature. First, the test methods are described. After that, the important parameters such as yield strength, stress-strain curve and ultimate strength are described. However, in Chapter 3, the mechanical properties are tested and then compared to literature results.

2.4.1 Testing methods

Haroush et al. (2015) determines the mechanical parameters using two tests: a tensile test and a small punch test (SPT). The specimen thicknesses are 0.2 and 0.1 mm. The following two subsections describe the tests.

2.4.1.1 Tensile test

The specimens are cut using a electronic discharge wire cutting machine according to ASTM standard E 8M-04 ("ASTM E 8M-04", 2022). The specimens are preloaded in the low elastic region before the start of the tensile test. The tensile test pulls on the specimen until failure and measures the strain and force. Figure 2.30 shows the specimen geometry for the tensile testing.

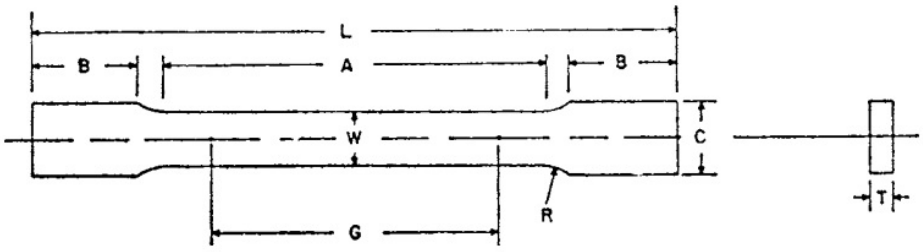

Figure 2.30: *Tensile test specimen geometry ("ASTM E 8M-04", 2022).*

2.4.2 Yield and ultimate strength

The yield and ultimate strengths were extracted from the small thickness tensile test described in subsubsection 2.4.1.1. Haroush et al. (2015) performed the experiments five times for each thickness and the average results are shown in Table 2.2.

Table 2.2: *Results tensile testing (Haroush et al., 2015).*

$t\ [mm]$	$\sigma_y\ [MPa]$	$\sigma_{uts}\ [MPa]$	$\varepsilon_{max}\ [\%]$
0.1	270	650	50.6
0.2	280	654	62.5

2.4.3 Stress-strain curve

A stress-strain curve relates the stress to the corresponding strain. The engineering or total strain consists of an elastic and a plastic part. The elastic strain is:

$$\varepsilon_{elastic} = \frac{\sigma}{E} \tag{2.8}$$

where σ is stress, and E is Young's modulus. The total strain is the sum of elastic and plastic strain.

Figure 2.31 shows a plot of the stress-strain curves for SS316L with thicknesses 100 and 200 µm. Note that the engineering stress and strain should be converted to true stress and strain. The reason for this is that FEA simulation software does not determine the stress and strain using the initial area or specimen length.

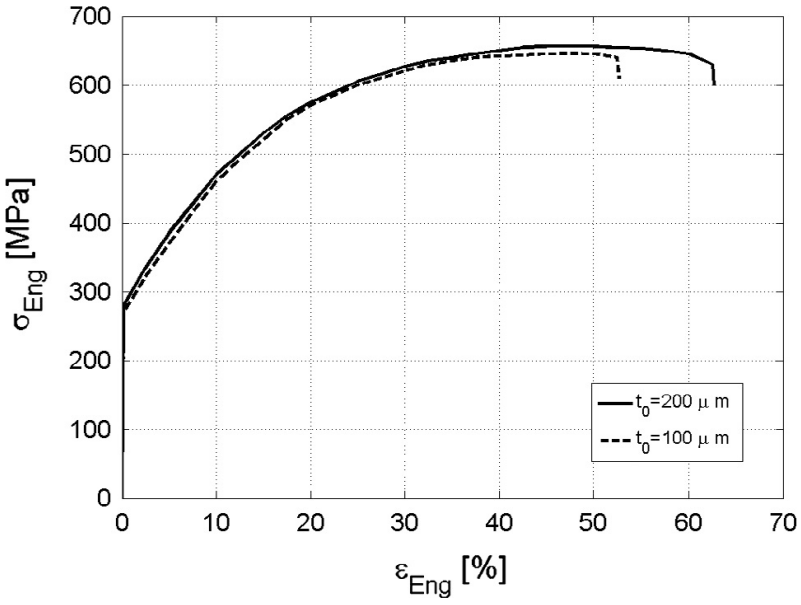

Figure 2.31: *Stress-strain curve (Haroush et al., 2015).*

2.5 Springback

Springback is an important side effect of metal sheet forming. However, it is not the focus of this research, but it is important to understand the basics. Springback could cause problems in the foreseeable future for rotary forming BPP production methods. Springback causes problems for the desired BPP shape and quality. Ensuring the correct geometry is crucial for gas flow in the BPP and this is crucial for the fuel cell performance. Therefore, it is crucial to measure and predict springback in the forming process. When the springback is identified, avoiding or compensating measures can be taken. This section discusses the basic springback definition.

2.5.1 Definition of springback

Amongst others, Carden et al. (2002) defines springback as "the elastically-driven change in shape of a part upon unloading after forming." Adding to that, Gan and Wagoner (2004) states "Springback of sheet metal parts after forming causes deviation from the designed target shape and produces downstream quality problems and assembly difficulties." This means that springback affects the quality and dimensional accuracy of formed metal components. However, a portion of this deformation is elastic, and when the specimen is unloaded, it tends to partially deform back to its original shape. Figure 2.32 shows a bending only springback situation. This figure shows that the initial die bending angle is not the same as the final bending angle. This is due to the springback properties of metal (Narayan, 2012).

Figure 2.33 shows a typical stress-strain curve for springback bending. This figure shows the plastic and elastic stress and strain upon loading and unloading. If the loading is larger than the yield stress, the material undergoes strain hardening and the deformation is plastic. Upon unloading, the plastic deformation stays and the elastic deformation goes back to zero. However, this is only the case for a uniaxially loaded specimen. The slope of the unloading curve is equal to the slope of the elastic loading curve (Trzepiecinski & Lemu, 2017).

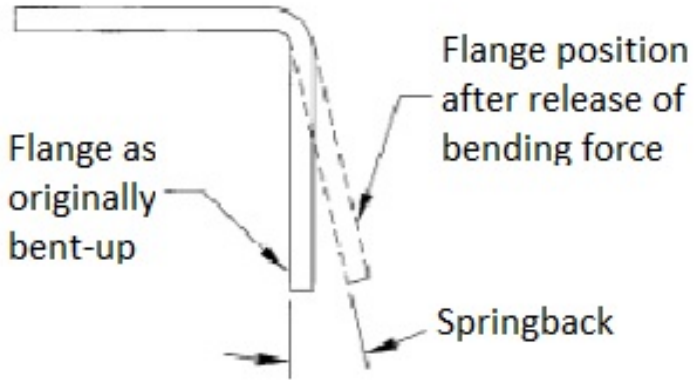

Figure 2.32: *Springback (Chikalthankar et al., 2014).*

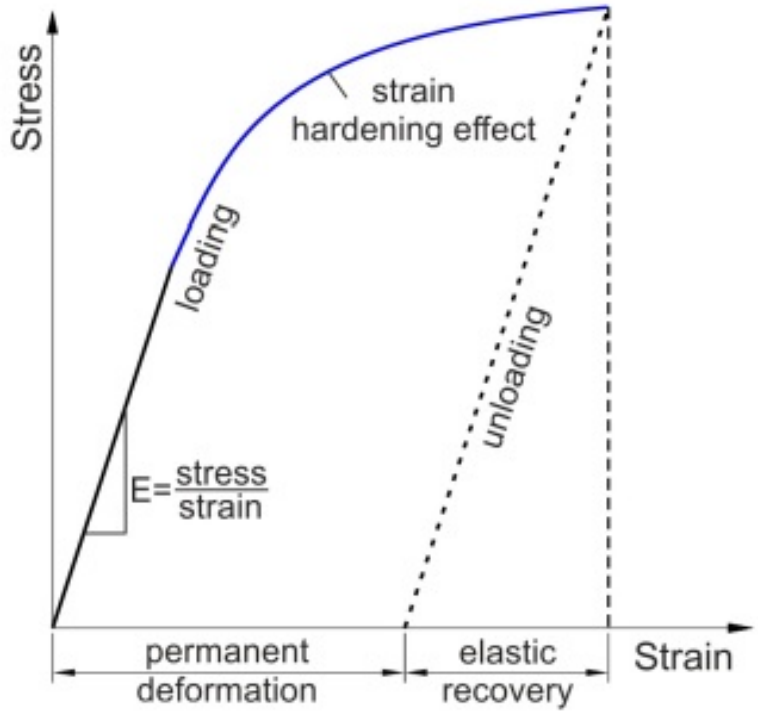

Figure 2.33: *Stress-strain curve uniaxial springback bending (Trzepiecinski & Lemu, 2017).*

3 Mechanical testing

Mechanical properties are measurable physical properties that a material exhibits upon force application. Typical properties are: strength, fatigue limit, toughness, ductility. This chapter describes how and why the mechanical properties are useful to determine. SS316L test pieces are tested to gain knowledge about the mechanical properties. The mechanical properties are then converted and are used as input for FEA simulations.

3.1 Orientation

Cylinder, channel, die and sheet orientation are important factors to address. In rotary forming, there are two main forming directions, axial and perpendicular to the axis. These are revered to as cross-web and web direction. In this report there are three different coordinate system used: sheet, channel and cylinder coordinate systems.

The sheets have three main directions: web, cross-web and thickness. The web direction is perpendicular to the rotational axis. Cross-web is along the rotational axis and thickness is in the sheet thickness direction.

The formed channel directions are in: channel, cross-channel and thickness. However, a channel can be formed in either web or cross-web direction.

Figure 3.1 shows the fundamental cylinder, channel and sheet directions. Where R is the radius and L is the cylinder length. In Figure 3.1 the channel is formed in web direction.

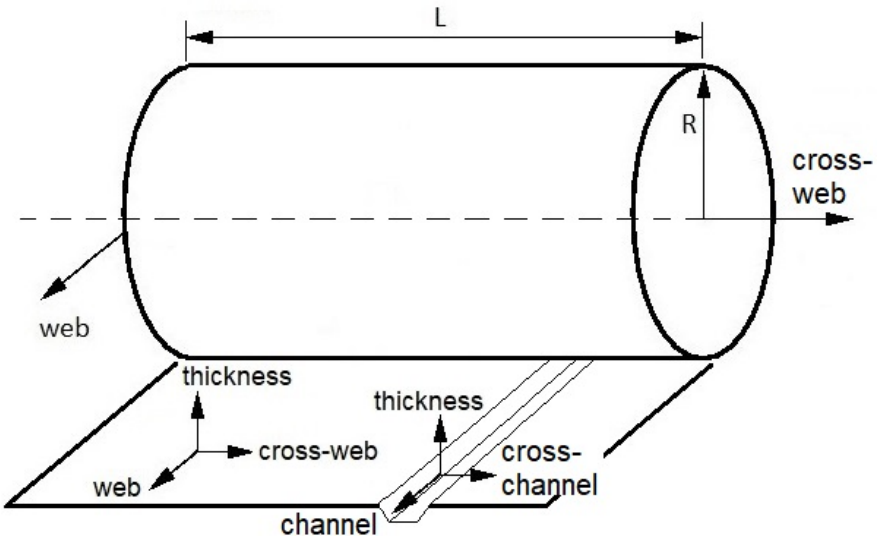

Figure 3.1: *Orientation cylinder, channel and sheet.*

3.2 Strain rate

Strain rate is the time derivative of strain, and it has an influence on the stress-strain curve of steels (Langdon & Schleyer, 2004). Strain rate is important for deforming of steel. Most elastic plastic materials have a form of strain rate sensitivity, whereby the strain rate influences certain mechanical properties.

3.2.1 Strain rate calculation

Rotary conversion is expected to have high strain rates because it is a relatively fast process. This means that the steel gets small amounts of time to deform. The strain rate is based upon a desired production rate which should be achievable by rotary conversion. The cylinder is partitioned in segments which house a die. Usually, the upper cylinder houses male dies and the lower cylinder houses female dies.

The cylinders are turned by hand in the experiments described in Chapter 4. However, the desired production rate could be much higher. It is based on current production rates which are achieved by the packaging industry. Strain rate is calculated as follows:

$$\dot{\varepsilon} = \frac{\varepsilon_{max}}{T_d} \tag{3.1}$$

where ε_{max} is maximum plastic strain and T_d is deformation time. The strain goes from zero to maximum strain over an amount of time T_d. The initial contact point between the male die and sheet is the start of the process. Strain at the initial contact point is zero. The process ends when θ is zero. At θ is zero, strain has reached its maximum. The positive rotation direction is counter clockwise. Figure 3.2 illustrates this process.

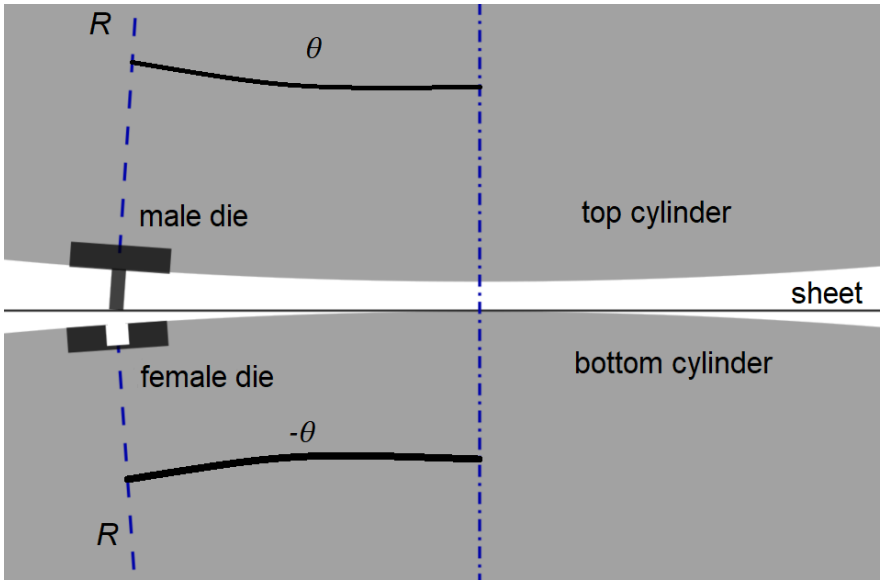

Figure 3.2: *Initial contact point between male die and sheet with corresponding angle θ.*

The maximum strain occurs when the die penetration is at its maximum. The maximum strain is calculated in Chapter 5.

The angle θ is solved with trigonometry and it can be described with the triangle shown in Figure 3.3. Where S is the inclined side, Y is the vertical side, X is the horizontal side and θ is the same angle as in Figure 3.2.

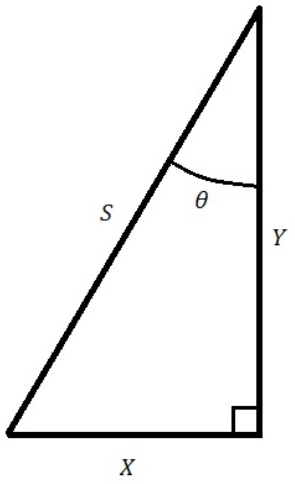

Figure 3.3: *Triangle representation of the strain problem.*

S is defined as follows:

$$S = R + t_s + H_s \tag{3.2}$$

where R is the cylinder radius, t_s is the shim thickness and H_s is the male die height.

Y is defined as follows:

$$Y = R + G_c - t \tag{3.3}$$

where R is the cylinder radius, G_c is the cylinder gap and t is the sheet thickness. Now the angle θ is calculated as follows:

$$\theta = cos^{-1}\left(\frac{Y}{S}\right) \tag{3.4}$$

The angular velocity is:

$$\omega = \frac{v}{R} \tag{3.5}$$

where v is the web speed.

The deformation time is a function of angle θ and angular velocity ω and is calculated as follows:

$$T_d = \frac{\theta}{\omega} \tag{3.6}$$

The ε_{max} and T_d are plugged into Equation 3.1 and the final results are shown in Table 3.1.

Table 3.1: *Result strain rate calculation.*

ε_{max} [-]	T_d [s]	$\dot{\varepsilon}$ [s^{-1}]
0.131	0.030	4.37

3.2.2 Strain rate correction

Strain rate affects the mechanical properties. Obtaining tensile test results for stress-strain curves at high strain rates are difficult or impossible. Therefore, the stress-strain curves can be corrected by some pre-developed models like Cowper-Symonds (Cowper & Symonds, 1957). In 1957, Cowper and Symonds developed a function which relates the static and dynamic yield stresses as shown below:

$$\frac{\sigma_d}{\sigma_s} = 1 + \left(\frac{\dot{\varepsilon}}{C_{cs}}\right)^{\frac{1}{P}} \tag{3.7}$$

where the parameters $\dot{\varepsilon}$, σ_d and σ_s are the strain rate, dynamic and static yield strengths and C_{cs} and P are material constants.

Langdon and Schleyer (2004) tested the strain rate effect experimentally and compared it to literature results from Burgan (2001). The tests were done for 2 to 4 mm SS316L sheets. The values for σ_d are calculated using $\dot{\varepsilon}$ from Table 3.1. Table 3.2 shows the final results. The next section describes the tensile strength and testing.

Table 3.2: *Cowper-Symonds parameters (Langdon & Schleyer, 2004).*

$material$	σ_s $[MPa]$	σ_d $[MPa]$	C_{cs} [-]	P [-]
SS316L	270	443.9 - 497.5	429 - 2721	4.1 - 5.8
SS316L	270	533.1	240	4.74

3.3 Tensile strength

Tensile strength of steel is mostly expressed with two specific parameters: yield and ultimate strength. The yield strength describes a stress point after which a material starts to deform plastically. Material deforms elastically up to the yield stress and after reaching this point it is deformed plastically. Normally the yield strength for SS316L ranges from 170 up to 300 MPa. According to Haroush et al. (2015) the yield strength is 270 MPa.

Ultimate tensile strength describes the maximum engineering stress of the stress-strain curve. Normally, SS316L tensile ultimate strength ranges from 450 up to 620 MPa. According to Haroush et al. (2015) the ultimate strength is 650 MPa.

Strength is mostly expressed in tensile strength. However, during rotary forming, sheets are not only exposed to tensile stress and strain but also to compressive stress and strain. When a sheet is purely bent, it endures tensile stress and strain on one side of the neutral axis and compressive stress and strain below on the other side.

Tensile testing is a method to determine the mechanical properties. The Dynamic Mechanical Analysis (DMA) Q800 machine is used in this research and it is produced by TA Instruments ("TA Instruments Thermal Analysis", 2010). It can test material in numerous ways such as, dual or single cantilever, 3-point bend, tension, shear, compression and submersion. It is especially made to deal with tiny samples, and has a maximum force of 18 N. Figure 3.4 shows the specimen dimensions. Applying the maximum force of 18 N to the specimen results in a maximum stress of 720 MPa. The tensile tests are performed by the DMA machine.

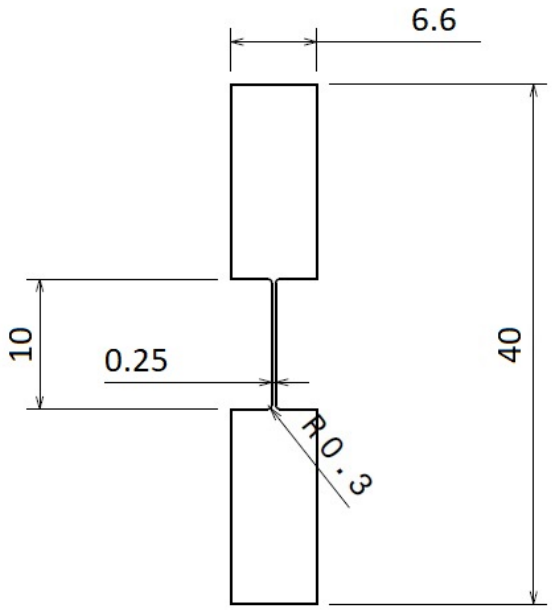

Figure 3.4: *Tensile test sample dimensions.*

3.4 Results tensile testing

Three tensile tests were performed, and the engineering results are shown in Table 3.3. Where t is sheet thickness, σ_y is yield stress, σ_{uts} is ultimate stress and ε_{max} is maximum strain. The yield stresses are taken at 0.02% strain. The results are compared to the results from Haroush et al. (2015) and Langdon and Schleyer (2004).

The engineering stress and strain needs to be converted to true stress and strain, before they are used as input for FEA simulations. The tensile tests were performed with a grip speed of 0.200 mm/min and this corresponds to a strain rate of 0.00033 s^{-1}. Then the results were corrected for a strain rate of 4.369 s^{-1} by using the Cowper-Symonds method. The engineering, true and corrected results are in Figure 3.5. Figure 3.6 shows the tensile test specimen after it has failed.

The true and strain rate corrected yield stress is 384 MPa at 0.002 strain and ultimate stress is 1415 MPa at 0.45 strain. These are the final results and inputs for the FEA simulations. The values tested by the tensile tests are very well relatable to the results from literature. However, the tested values are slightly lower than the values from literature. This could be due to differences in thickness and strain rate.

Table 3.3: *Engineering results from tensile testing and literature.*

$t\ [mm]$	$\sigma_y\ [MPa]$	$\sigma_{uts}\ [MPa]$	ε_{max} [-]	$source$
0.1	267	633	0.56	tensile test
0.1	270	650	0.51	Haroush et al. (2015)
0.2	280	654	0.63	Haroush et al. (2015)
2.0	294	645	0.52	Langdon and Schleyer (2004)
2.0	298	640	0.57	Langdon and Schleyer (2004)

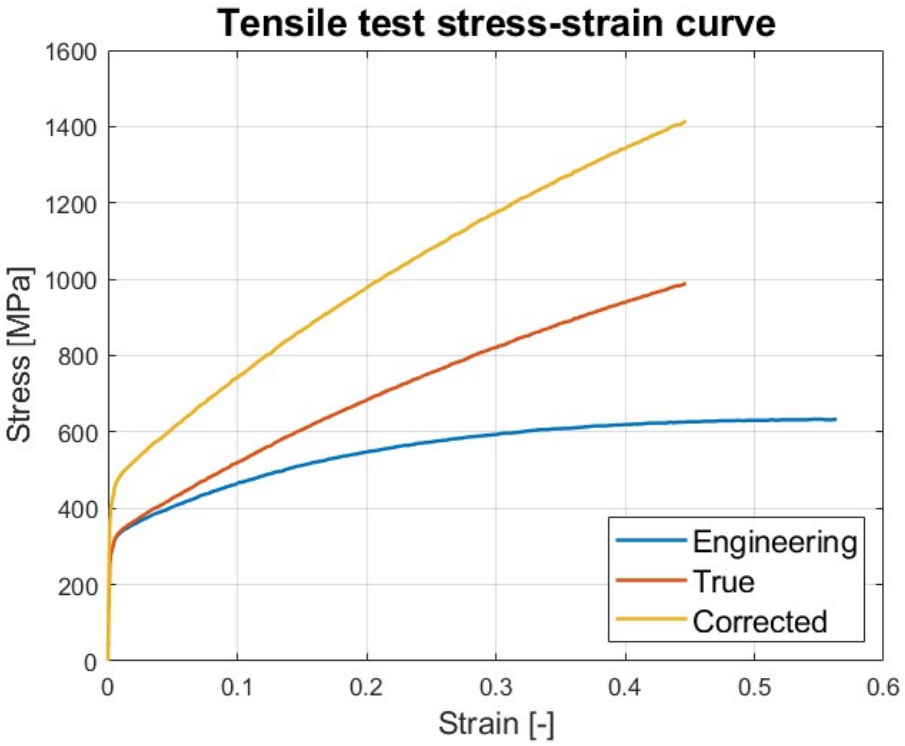

Figure 3.5: *Tensile test stress-strain curves for engineering, true and corrected results.*

Figure 3.6: *Failed tensile test specimen.*

4 Experiments

The single channel experiments are performed to measure strain and verify FEA simulations. Application of plain strain conditions is an important assumption that needs to be verified in a separate experiment. Both experiments are similar as in the dies and set-up are the same. This chapter describes how the two types of experiments are performed.

4.1 Test setup

Madern tests new dies and concepts in a separate test and measurement room. The testing room is temperature regulated because they perform measurements up to very fine margins. One of the test setups at Madern includes two cylinders, each with a 257.96 mm radius. This setup is used for the experiments performed in this research.

The test cylinders are rotated by hand. However, in production, cylinders are driven by an electric motor which maintains a constant speed. The intended production speeds are higher than the test speed. As the testing rotational speed is lower, the forming time takes longer than in the production phase.

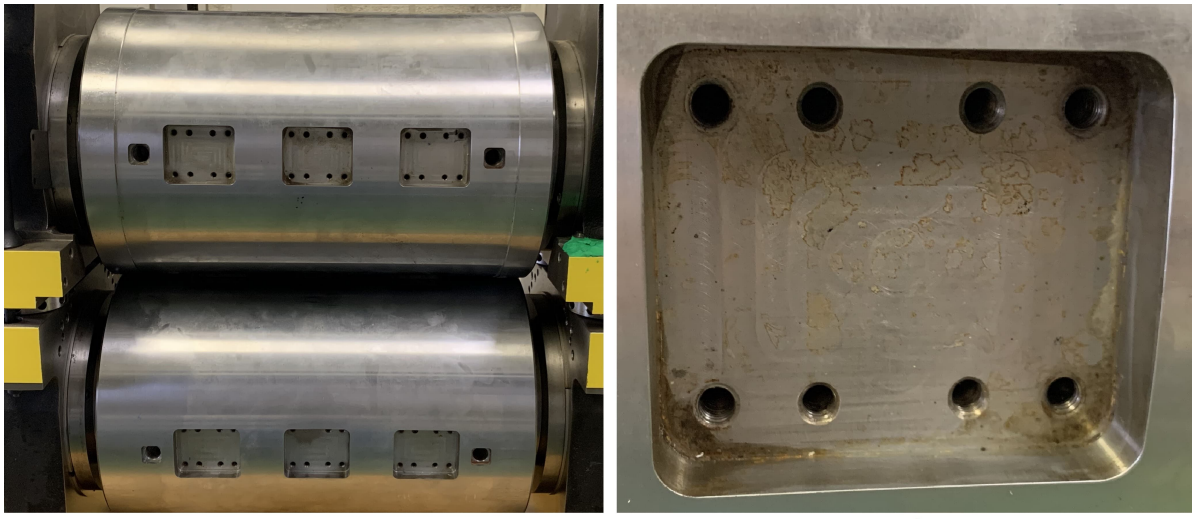

Figure 4.1: *Test setup: (a) test cylinder and (b) cutout.*

The cylinders contain cutouts, in which male and female die segments are fitted. Figure 4.1 shows the test cylinder and a close up of a cutout. The cutout height is 50 mm and the width is 60 mm. The male segment height is 49.99 mm and width is 59.80 mm. The female segment height is 49.99 and width is 59.99 mm and fits flush in the cutout. Die alignment is an important step, and they should be aligned in two directions. The segments are adjusted in cross-web and thickness direction. This is done by adding shims in between the cutouts and segments. Shims are placed behind the segments to adjust the thickness direction alignment and die indentation. The segments can also be aligned in cross-web direction. Shims are little sheets that are put in between the die and the cut-out of the cylinder. In this way, the die indentation is regulated by using different shims with different thicknesses. Usually, the shims are placed behind the male die, before it is mounted in the cylinder. Figure 4.2 shows a 0.10 mm thick shim.

Figure 4.3 show two segment pairs. The top two are male die segments and the bottom two are female die segments. The segments are curved in web or in cross-web direction. The patterns

on left two segments are orientated in web direction and the patterns on the right two segments are orientated in cross-web direction. Normally, these dies are used to crease cardboard and not to deform stainless steel. However, these dies were readily available at Madern. Ideally, new dies should be designed and made to optimise the channels. However, these dies can still provide useful information for the determination of bending and membrane strain. Figure 4.4 shows the die dimensions. “MD” means machine direction and denotes the dies in web direction. “CD” means cross direction and denotes the cross-web direction. All single channel experiments in this research are performed using these dies.

The cylinder gap is 1.55 mm and stays constant over the whole radius and length. The segment heights are shown in Figure 4.4. However, the die penetration depth is adjusted by adding or removing shims. The shims are placed behind the male die and the female die is flush with the bottom cylinder. The penetration depth is calculated as follows:

$$D = H_s - G_c + t_s \tag{4.1}$$

where D is penetration depth, H_s is segment height, G_c is cylinder gap and t_s is shim thickness. The die penetration depth are calculated, and the results are shown in Figure 4.5.

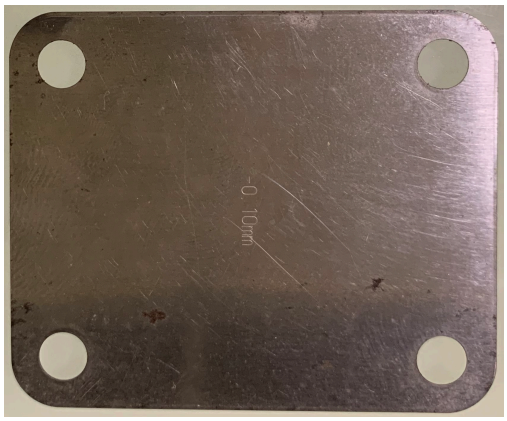

Figure 4.2: *Shim of 0.10 mm thickness.*

Figure 4.3: *Four die segments: The top row shows male dies and on the bottom row shows female dies. The left male and female dies form web channels. The right male and female dies form cross-web channels.*

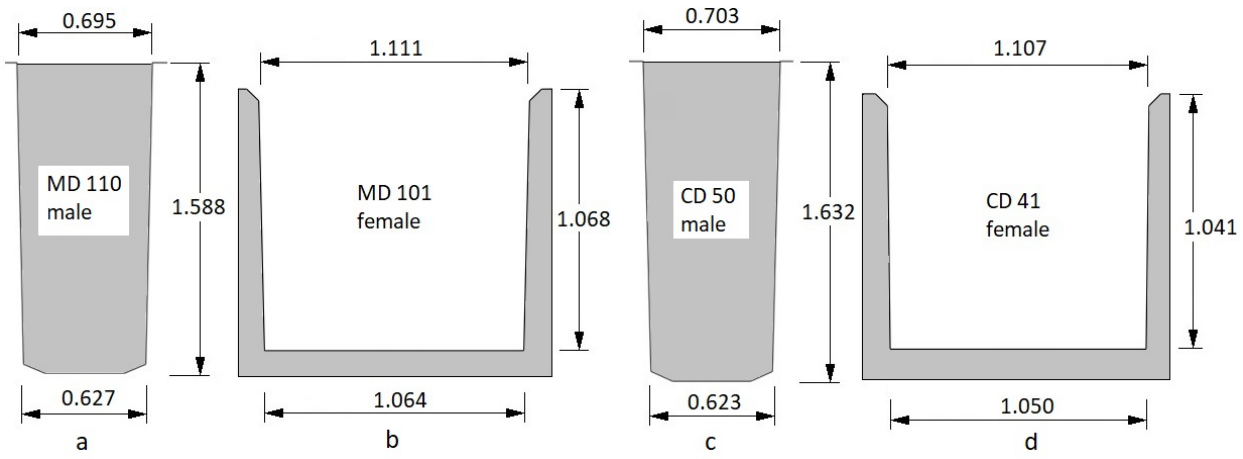

Figure 4.4: *Dimensions dies: (a) male MD 110, (b) MD 101 female, (c) CD 50 male and (d) CD 41 female. (a) and (b) show web direction dies and (c) and (d) show cross-web direction dies.*

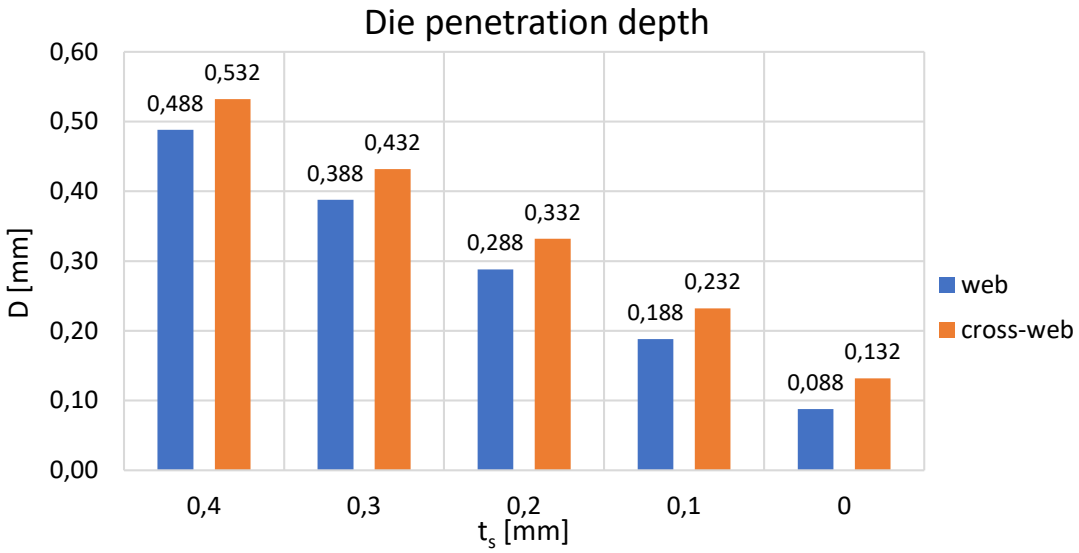

Figure 4.5: *Die penetration depth for different shim thickness.*

4.2 Single channel experiments

The single channel experiments are performed to measure strain and validate the FEA simulations. The dies, described in Section 4.1, are used for the experiments. The experiments are performed using six different configurations. The first differentiation is the channel direction, this is either web or cross-web direction. The second differentiation is shim thickness, this is 0.2, 0.3 or 0.4 mm. This results in six different experimental configurations and results.

The dies are placed in the cylinders. The male dies are placed in the top cylinder with the corresponding shim thickness behind them. The female dies are placed in the bottom cylinder. The sheet gets deformed by the rotating cylinders. When the experiments are done, the strain is measured. This is described in Chapter 5.

4.3 Plane strain condition

If the plane strain assumption is adopted, FEA simulations and strain calculation become simpler. If a specimen satisfies zero or negligible strain in a single direction, and strain is not negligible in the other two directions, then the plane strain condition may be applied. For channels, it is assumed that strain is occurring only across the channel direction. Strain along the channel direction is assumed to be zero or is neglected. This results in a strain tensor as shown below:

$$\varepsilon_c \approx 0 \rightarrow \begin{bmatrix} 0 & 0 & 0 \\ - & \varepsilon_{cc} & \varepsilon_{23} \\ sym & - & \varepsilon_t \end{bmatrix} \tag{4.2}$$

where ε_c is strain in channel direction, ε_{cc} is strain in cross-channel direction, ε_t is strain in thickness direction and ε_{23} is a shear strain component. When plane strain is verified, the FEA simulations, for the single channel experiments, can be done in 2D. The assumption can be verified with experiments and these experiments are elaborated in the next section.

4.4 Plane strain experiments

Experiments are done to verify the plane strain condition. During this experiment, a sheet is deformed by rotary conversion. It is deformed in either web or cross-web direction. The experiments are done for web and cross-web direction separately. The dies, described in Section 4.1, are used for these experiments. The purpose of the experiment is to check if strain is happening in the direction along the channel and in thickness direction. This means that deformation is only happening in the plane that is perpendicular to the channel. Strain along the channel should be negligible or not present. For example, if a channel is formed in web direction, strain should occur in thickness and cross-web direction. However, strain in web direction should be negligible, in order for the plane strain condition to hold.

4.4.1 Grid

A square lines grid is applied on the specimen surface with a grid spacing of 0.15 mm. This is small enough to see changes in the lines. However, it could not be much smaller otherwise the heat and surface damage caused by the laser engraver was too large. The grid size and visibility were achieved by trail and error. Figure 4.6 shows the grid on the surface.

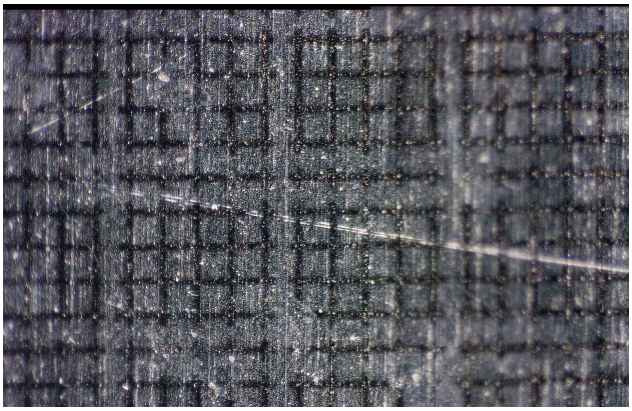

Figure 4.6: *Square lines grid spacing of 0.15 mm.*

4.5 Plane strain validation

The 0.4 mm shims are used in these experiments, because this gives the most deformation. Figure 4.7 shows the plane strain experiment results. The grid spacing is measured parallel and perpendicular to the channel. Measurements five and seven are at the bottom of the channel. However, measurement six is taken in plane. Therefore, a 3D image is made to measure strain across the specimen profile.

Figure 4.8 shows the specimen profile. Measurements two and three show the grid spacing on the channel bottom. Measurement one and four show the grid spacing on the channel side. If the length difference was measured in the plane, it should be concluded that it shrunk by 0.0507 mm. However, if it is measured along the channel, the spacing is 0.1607 mm thus it is enlarged by 0.0107 mm. This results in a strain of 0.0715 which indicates that strain across the channel is present. Strain along the channel is not present as the grid spacing does not change. Therefore, this experiment shows that the plane strain condition is a valid assumption.

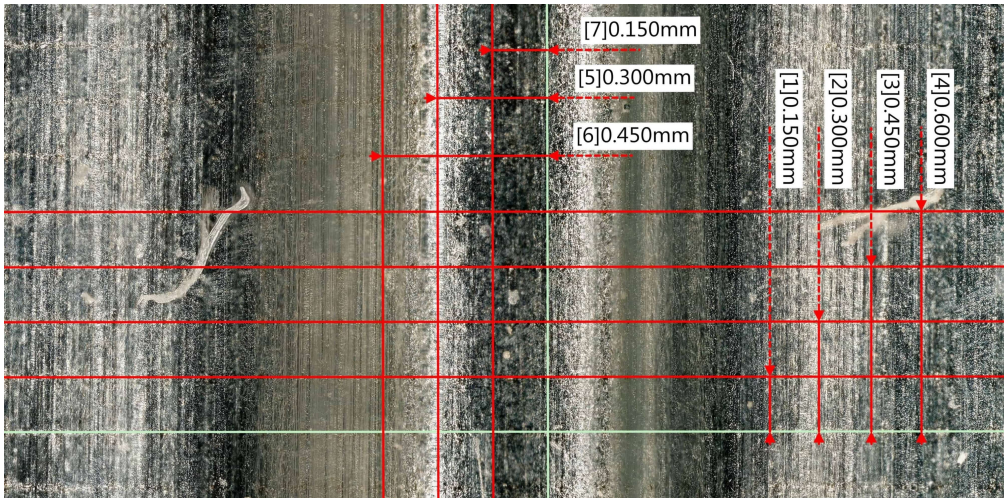

Figure 4.7: *Square grid plane strain experiment.*

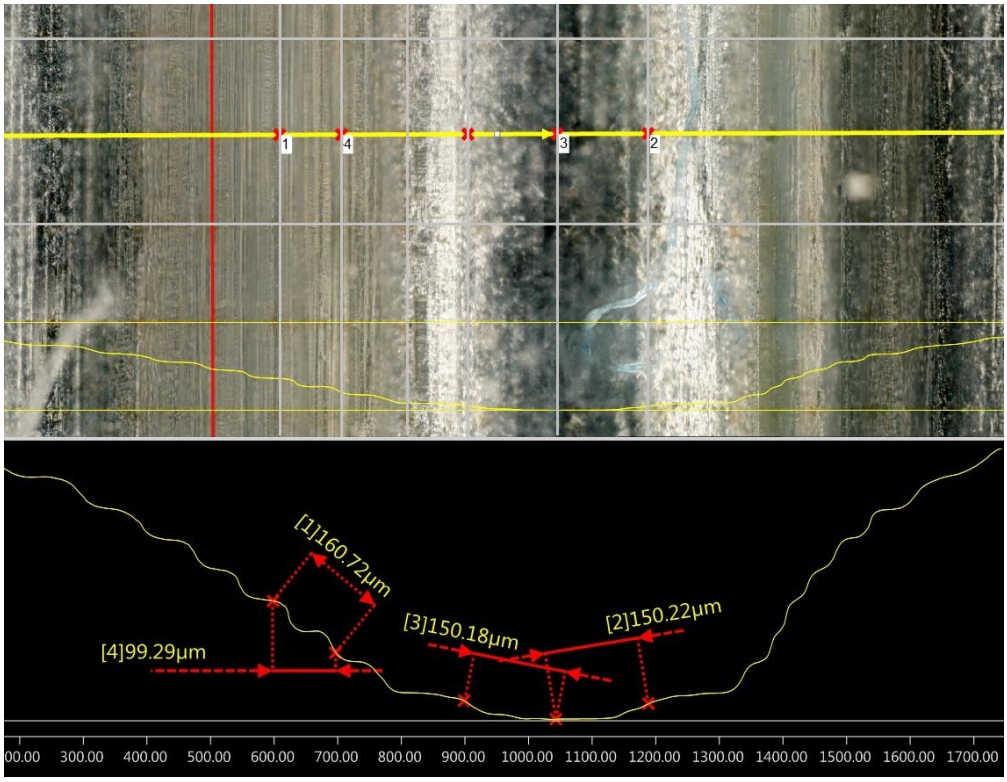

Figure 4.8: *Plane strain profile measurement.*

5 Strain determination and results

Total strain on a cross-section consists of a bending and a membrane component. The bending strain is calculated with the radius of curvature. The thickness strain is measured with help of cross-sections. Then the membrane strain is calculated using conservation of volume. Eventually, strain measurements are used to validate FEA simulations and to determine the bending and membrane strain. Strain is elaborated in the following sections.

5.1 Total strain

There are three main contributions to the overall strain: membrane, bending and thickness strain. Membrane and bending strain occur is either web or cross-web direction and thickness strain only occurs in thickness direction. The total strain is the summation of three contributors:

$$\varepsilon_{total} = \varepsilon_{mem} + \varepsilon_{ben} + \varepsilon_t \tag{5.1}$$

where ε_{total} is total strain, ε_{mem} is membrane strain, ε_{ben} is bending strain and ε_t is thickness strain. The next sections elaborate each individual strain contributor.

5.2 Thickness strain

The thickness strain is measured from the cross-section of experiments described in Section 4.2. The formed specimen are cut and mounted in resin. After mounting, the specimen is polished to reveal a smooth surface edge. This shows the cross-sections and the thickness distribution across the specimen. The polishing is done to even the surface and get rid of any cutting marks or scratches. Then the cross-sectional thickness is measured under a microscope.

The thickness measurements are focused on four areas where the most thinning occurs. The bends of the cross-sections show the most thinning and are numbered from one to four as defined in Figure 5.1.

The true thickness strain is calculated as follows:

$$\varepsilon_t = ln\left(1 + \frac{t_1 - t_0}{t_0}\right) \tag{5.2}$$

where Δt is difference in thickness, t_0 is original thickness and t_1 is measured thickness after deformation. It is converted form engineering to true strain. For these experiments, the thickness strain is always negative because only thickness reductions are measured. Thickness increase is not present in the experiments.

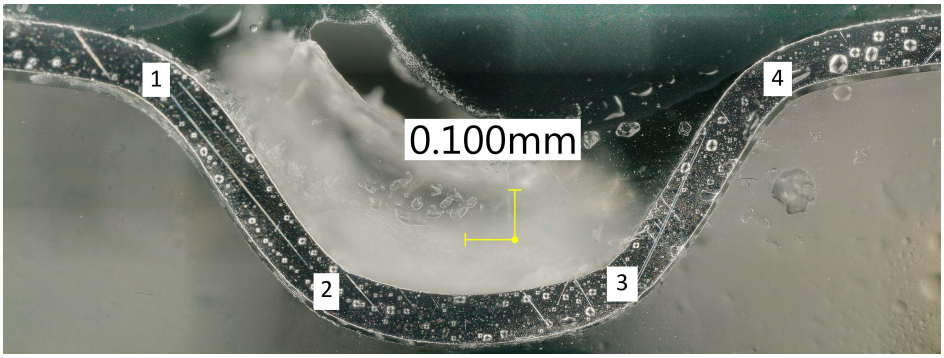

Figure 5.1: *Identification of four bends.*

5.2.1 Thickness strain results

The results are arranged by bend numbers, direction and shim size. In total, six different configurations are experimentally tested. The distinctions are: shims with 0.2, 0.3 and 0.4 mm; thickness; and web versus cross-web direction. The results are measured by making a cross-section from each configuration. From each cross-section, a microscopic picture is taken, and the thicknesses are measured. The pictures have a resolution of 0.0004 mm per pixel. The average thickness is measured at five locations and averaged. These five locations are the undeformed areas before corner one, in between corners one, two, three and four and after corner four. For strain calculation, the thickness at each corner is compared to the average thickness. Figure 5.2 shows the thickness measurements.

All results are shown in Appendix A. The measurements are used to calculate corresponding strain at each corner for each direction and configuration. Figure 5.3 shows the thickness strain in web and cross-web direction for each corner. The channel direction can either be in web or cross-web direction. Which means that in Figure 5.3, 0.2 web means that the channel is formed in web direction and has a shim thickness of 0.2 mm. This convention is adopted for all results.

The web thickness strains are larger than the cross-web thickness strains. 0.2 and 0.3 web behave similar to each other and have low strain for bends one and four and have high strain for bends two and three. However, 0.4 web is almost opposite to 0.2 and 0.3 web. It has low strain for bends two and three and high strain for bends one and four.

The results for 0.3 and 0.4 cross-web are similar to each other. 0.2 cross-web behaves similar to 0.2 and 0.3 web. However, 0.2 cross-web has lower values than 0.2 and 0.3 web.

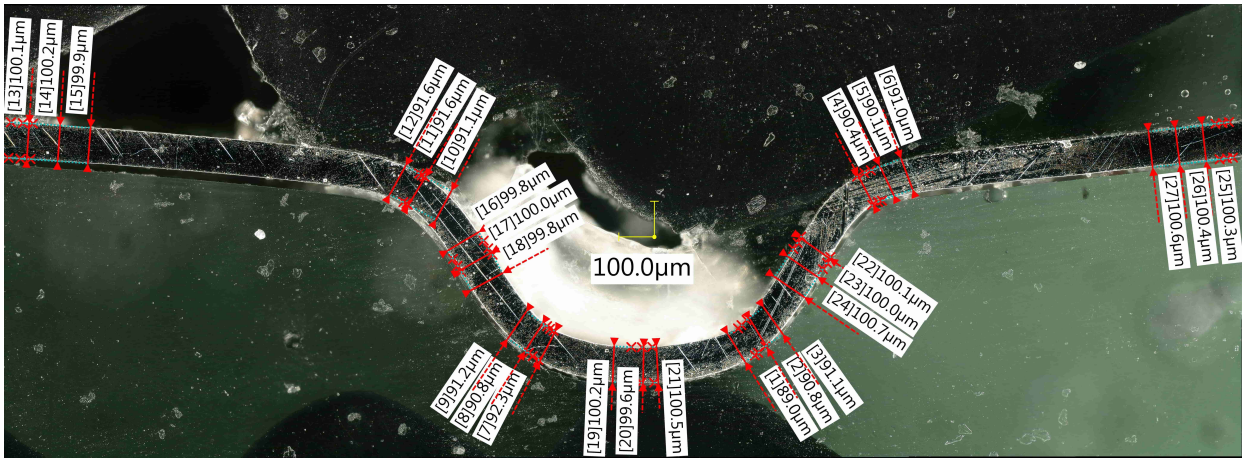

Figure 5.2: *Cross-sectional thickness measurement of a web channel with 0.4 mm shim.*

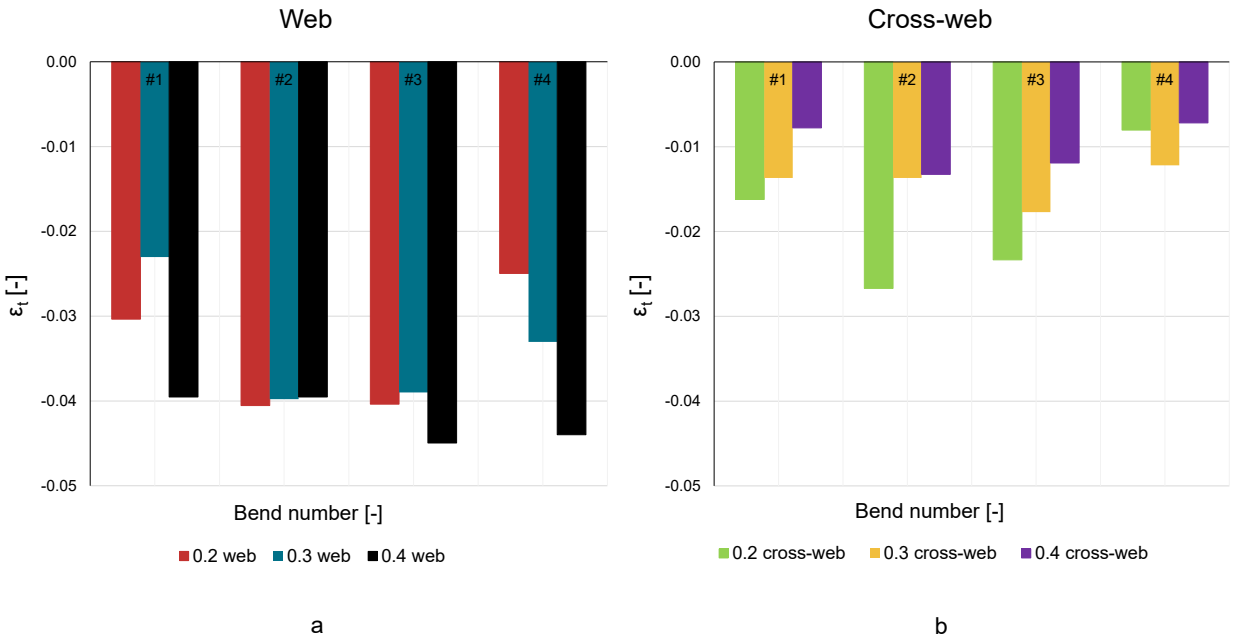

Figure 5.3: *Thickness strain results: (a) web and (b) cross-web results.*

5.3 Bending strain

Pure bending does not cause a neutral axis length difference. However, a combination of bending and membrane stress can cause a neutral axis length difference. This is called “stretch bending” and is described in subsubsection 2.3.2.2. Bending surface strain can either be positive or negative. If the convention described in subsubsection 2.2.1.2 is applied to Figure 5.1, then the first and fourth bends have a negative bending moment and the second and third bends have a positive bending moment. This corresponds to a positive strain in the first and fourth bends and a negative strain in the second and third bends.

Application of an internal bending moment causes a curvature in the specimen. This is the case for uniaxial bending. The bending strain is calculated as follows:

$$\varepsilon_{ben} = \pm\frac{y}{r} \tag{5.3}$$

where y is the distance from the neutral axis to the outer fibre and r is the radius of curvature. The maximum bending strain occurs on the material outside. The sheet thickness is not constant and y changes for each bend. The maximum thickness is 0.1 mm and the maximum y is then 0.05 mm. However, the thickness is reduced due to membrane strain and y is therefore less than 0.05 mm.

The bending radius of curvature is determined using the least squares circle fit. For each experimental configuration, a cross-section is made, and it is digitised. The least squares circle fit method, fits a circle, within a certain interval, on a curved line (Ahn et al., 2001). The specimen is bent in four areas, where each bent area has its own radius of curvature.

The formed sheets are digitised using a computer program that translates pixels to coordinates, by means of selecting several data points. The picture exists of pixels, which are arranged according to a reference x and y axis system. The axis system origin corresponds to the origin of scale bars. The pictures resolution is 0.0004 mm per pixel.

A neutral axis is determined from the data points. Figure 5.4 shows the digitised data points. The red dots correspond to the top surface and the yellow dots to the bottom surface.

Figure 5.5 shows the least squares fit of circles. The red and green circles fit inside a bent area and follow the blue curved neutral axis up to a certain accuracy.

Another strain measurement method is to apply a surface grid and check how the grid deforms under application of a bending moment. When a specimen is only subjected to pure bending, it is expected that the specimen neutral axis is not elongated or shortened. Consequently, the specimen that underwent pure bending should not display stretching signs. To monitor stretching, this method applies a grid on the surface. Because the grid is not on the neutral axis, it can deform slightly as it endures compressive and tensile strain. This means that in the compressive bending area, the uniform grid spacing should be reduced. In the tensile bending area the uniform grid spacing should be enlarged.

However, determining the bending strain with the grid method is less practical than checking the radius of curvature. This is because the grid has to be applied on both sides and the strain has to be measured in compression and in tension. This means that the grid has to be perfectly aligned on both sides to be able to determine the compressive and tensile strains. These two should then be related to the strain in the neutral axis.

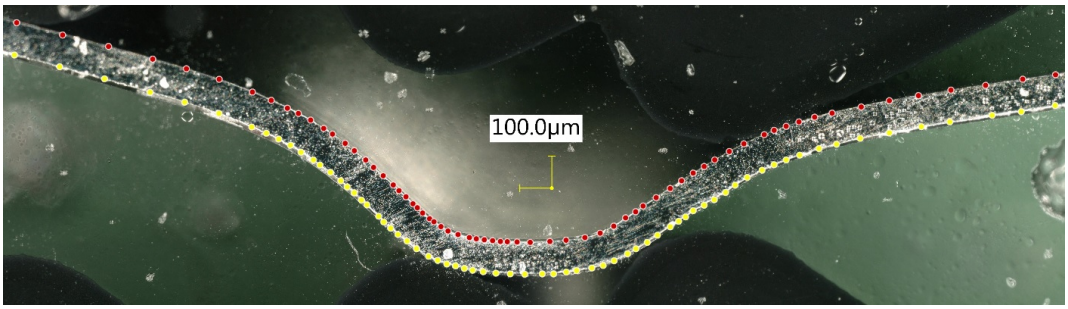

Figure 5.4: *Digitised cross-section for bending strain determination.*

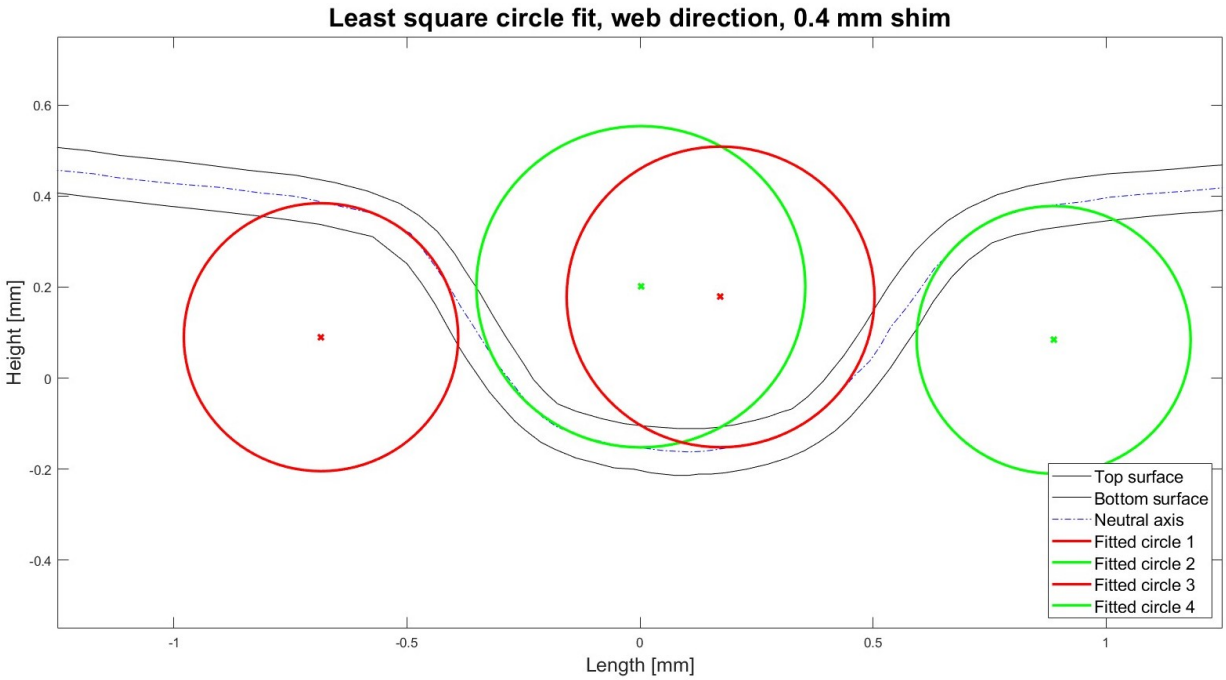

Figure 5.5: *Least squares fit of circle.*

5.3.1 Bending strain results

All bending strain results are shown in Appendix B. However, the bending strain results are summarised in Figure 5.6. For both web and cross-web direction, all strains in bends two and three are negative. The bending strains range from -0.150 up to 0.154. A larger bending radius causes less strain and a smaller bending radius causes more strain.

For web direction, it concludes that bending strain is increasing for increasing shim thickness. This is as expected because when the shim thickness is increased the indentation depth increases as well. However, there is one exception, the strain for bend two 0.2 web is slightly larger than 0.3 web.

For cross-web direction, the pattern is not similar to the web direction. For bends two and three, the 0.3 cross-web shows the largest strain. Bends one and four show opposite behaviour to each other. At bend one, the smallest shim shows the largest strain. At bend four the largest shim shows the largest strain.

The bending strain is calculated by dividing the distance from the neutral axis to the outer fibre, y, by the radius of curvature, r. The determination of y is completely depending on the accuracy of the thickness strain determination. Because it is defined as half on the sheet thickness. The radius of curvature, r, is determined over an interval. This is a partly manual process, in the sense that, the intervals are selected by hand. The interval selection determines the bending strain accuracy. However, the intervals and circle fitment are calibrated by eye. The Matlab script produces a figure and this is used to adjust the intervals.

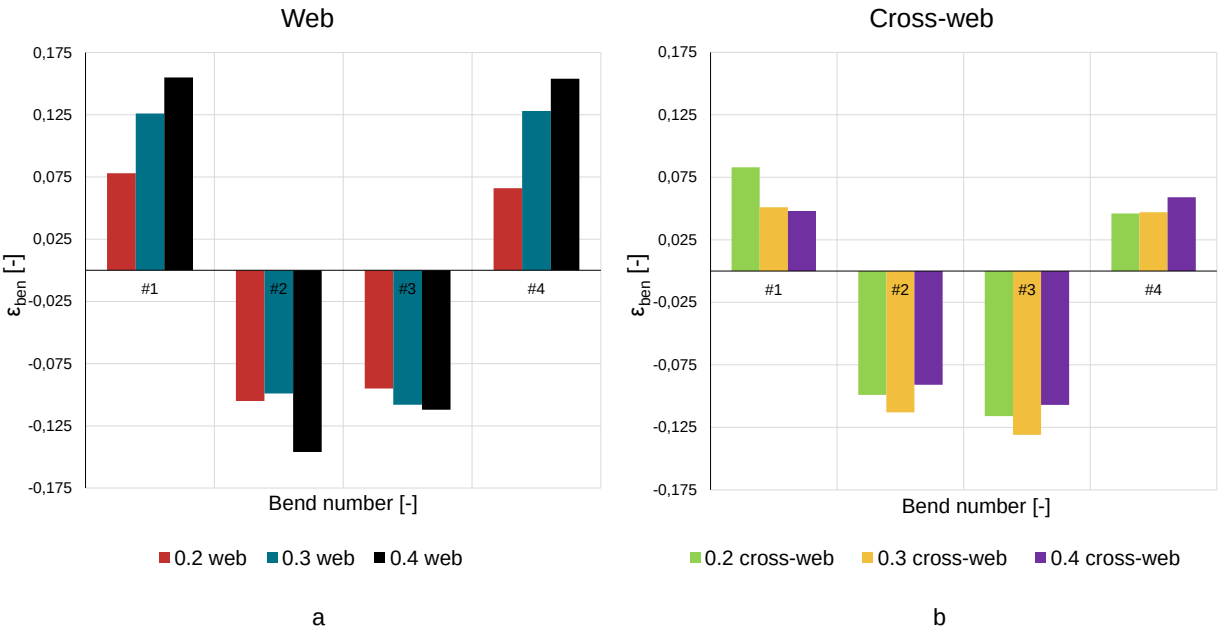

Figure 5.6: *Bending strain results: (a) web and (b) cross-web direction.*

5.3.2 Sheet curvature results

The channels are formed in web or cross-web direction. During this formation process, the sheets are also bent and deformed. Some sheets show more thickness reduction and some more overall sheet curvature depending on penetration depth, channel geometry and channel direction. All sheets are curved around the rotational axis of cylinders. The sheet curvature is compared by determining the angle between straight sides of the sheet. Angles closer to 180 degrees are straighter

than smaller or larger angles. Figure 5.7 shows how sheet curvature is measured.

By comparing the sheet curvature results from Figure 5.8, it is concluded that web channels have less overall sheet curvature than cross-web channels. This is declared by the fact that cross-web channels are allowed to follow the cylinder radius and web channels are restricted by the constant cylinder gap. None of the sheets is perfectly straight and this should be corrected for future designs. The geometrical consistency and straightness determines the BPP performance.

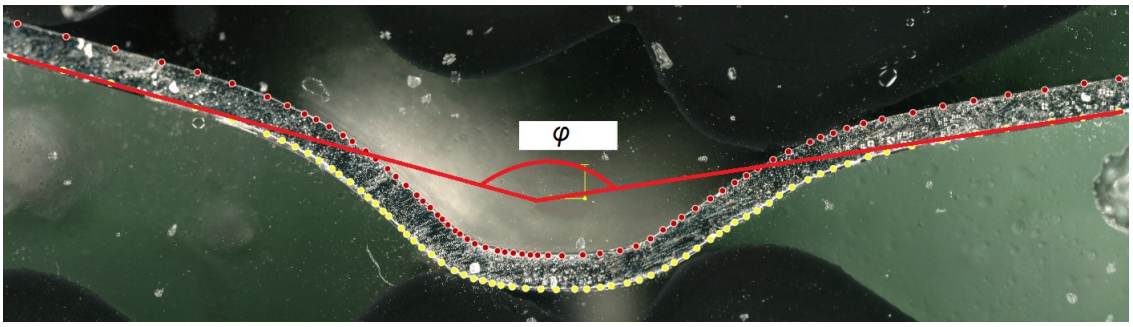

Figure 5.7: *Sheet curvature measurement.*

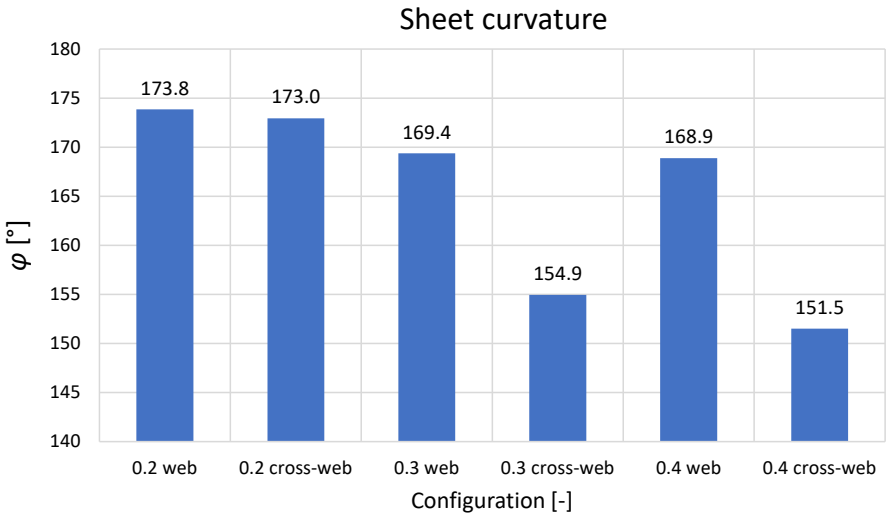

Figure 5.8: *Sheet curvature results.*

5.4 Membrane strain

A tensile test is a good example of pure membrane deformations. Conservation of volume states that, if a specimen is elongated, then the cross-sectional area has to reduce. The deformation is in 3D and therefore it shows strain in 3 directions. The membrane strain is calculated on the neutral axis. Therefore bending strain has no contribution to membrane strain. However, this would not be the case for strain calculation away from the neutral axis. Translate this to normal strain and the equation below holds:

$$\varepsilon_{mem} + \varepsilon_t = 0 \quad \rightarrow \quad \varepsilon_c + \varepsilon_{cc} + \varepsilon_t = 0 \tag{5.4}$$

where ε_t is strain in thickness direction and ε_{mem} is membrane strain and is composed of ε_c is strain in channel and ε_{cc} is strain in cross-channel direction. Applying the plane strain assumption, this equation is transformed from a 3D to a 2D problem. Now consider, the channel direction to have zero strain, then Equation 5.4 is reduced to conservation of area. If strain in channel direction is zero ($\varepsilon_c = 0$), then:

$$\varepsilon_{cc} + \varepsilon_t = 0 \quad \rightarrow \quad \varepsilon_{cc} = -\varepsilon_t \tag{5.5}$$

for this case, ε_{cc} is identified as membrane strain in cross-channel direction and ε_t is thickness strain. Or in more general form:

$$\varepsilon_{mem} = -\varepsilon_t \tag{5.6}$$

Membrane surface strain can be measured by application of a grid. When a specimen only endures membrane strain, it is expected that the grid on the specimen surface shows deformation. For purely membrane strain, if the neutral axis is elongated, then the strain should be uniform throughout the thickness direction.

There can also be local stretching, and this is not a uniform specimen lengthening. In (local) stretching areas, the material is more likely to endure necking because of the (local) cross-sectional area reduction. In a tensile test, necking mostly occurs just before failure, for most SS316L materials.

Membrane strain, over a deformed or curved surface, is difficult to measure with a microscope. This is because the microscope takes an in-plane picture. However, the actual surface is not a plane but deformed out of plane, so strain should be measured over an out of plane surface. This can be done by 3D scanning microscopes. Then a random pattern or point cloud should be identified and the distance between two points should be tracked over the deformed surface. When the original distance between these two exact points was known, strain is calculated. However, this means that the membrane strain is calculated, but only on one surface. For reliable results, the same method should be applied to the other side. To get the neutral axis membrane strain, the results for both surfaces should be averaged.

5.4.1 Membrane strain results

The membrane strain results are shown in Figure 5.9. The membrane strain is approximately equal to negative thickness strain. However, the thickness strain was already negative and that makes the membrane strain positive. Which would indicate material stretching.

The 0.2 and 0.3 web behave similar to each other and to 0.2 cross-web. The 0.2 and 0.3 web have higher strains than 0.2 cross-web. The 0.4 web has higher strains in bends one and four and has lower strains in bends two and three. This behaviour is opposite to the 0.2 and 0.3 web.

The cross-web direction has lower strains than the web direction. The 0.3 and 0.4 cross-web are relatively constant and similar to each other. However, 0.2 cross-web behaves differently.

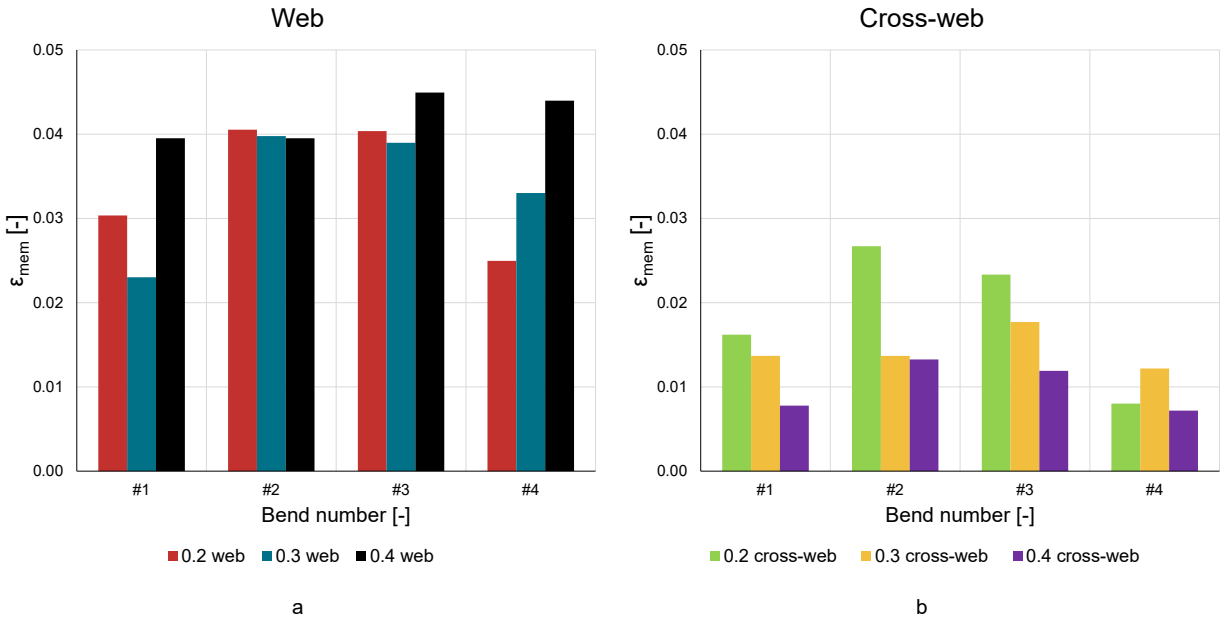

Figure 5.9: *Membrane strain results: (a) web and (b) cross-web direction.*

6 FEA model and results

FEA software simulates specific physical phenomena using a numerical technique. These simulations should provide insights in the mechanical behaviour of SS316L. FEA simulations should reenact the experiment up to a certain degree of accuracy. However, some assumptions and simplifications are made for time and convenience purposes. This means that care should be taken in which simplifications and assumptions are made. The used FEA simulation software is Abaqus CAE 2021 explicit solver and this chapter describes how the FEA process is modelled.

6.1 Assembly

The simulation consists of five parts: the sheet, female die, male die and two cylinders. The dies and sheet need to be assembled to replicate the experiment as closely as possible. The dies are fitted in the cylinder. The simulations are done in 2D because the plane strain assumption is verified in Section 4.5. Figure 6.1 shows the assembly in Abaqus. The dies used in the simulations are modelled to be exact copies of the dies used in the experiments as shown in Figure 4.4.

The intended BPP production process will use large sheets delivered on rolls. Therefore, the length is very large compared to the width and thickness. It could be the case that multiple BPPs are made using one set up. The cylinder could be partitioned in several sections, each with its own die. This means that the cylinder could be one metre wide but a BPP could be 100 mm wide. However, the sheet and die dimensions are kept close to the experiments. For simulation purposes, the sheet width is 60 mm and thickness is 0.1 mm.

The sheet travels at a constant speed through the dies, and it is a self pulling system. This means that when the cylinders start rotating, the sheet is pulled towards the cylinders. It is only fed into the cylinders to start the system it is not continuously fed into the cylinders. The next section describes the rotational cylinder and die movements for the FEA simulations.

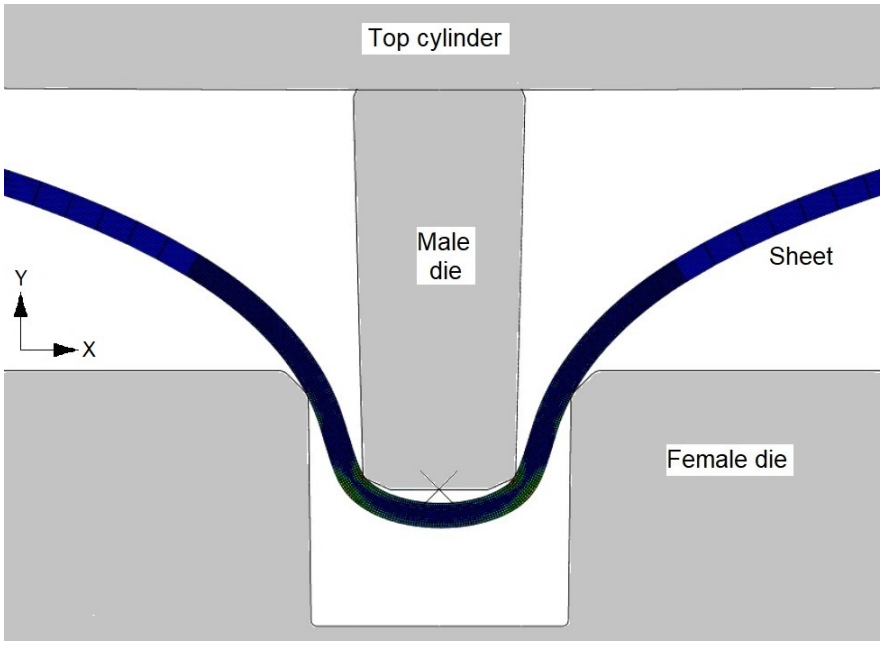

Figure 6.1: *Dies and sheet assembly.*

6.2 Rotary motion

The specimen is formed between two rotating cylinders. Normally, the top cylinder contains a male die and the bottom cylinder a female die. The rotational motion should be incorporated in the simulation. When the web is fixed, the rotational movement is described by a non slipping rolling cylinder across a flat surface. In this rotation, one specific point is followed along the cylinder circumference. However, in FEA simulation, the sheet and female die are held stationary. This means that only the male die motion needs to be modelled in FEA software. Figure 6.2 shows a full rotation. The red dot represents the male die and the blue dot the female die.

The focus lies on the die contact area (halfway through the rotation in Figure 6.2). During simulation, the sheet and female die are fixed in position so only the male die moves. This movement is broken down into a translation and a rotation.

Figure 6.3 is used to describe the x and y movement of the male die. The contact area with the female die is located at the cylinder bottom. The x and y coordinates of the contact area are (0,-R). The x and y coordinates are described as functions of the radius and angle:

$$x = Rsin(\theta) \tag{6.1}$$

$$y = Rcos(\theta) \tag{6.2}$$

The y movement is equal to the die indentation depth and R is the cylinder radius. Then the angle θ is calculated. When θ is known, the x movement is calculated as well. The x, y and θ are needed as input for FEA simulation. This way, the exact die movement is replicated for FEA simulation.

However, this is only applicable if the die contact points lie exactly on the cylinder circumference. If the contact points lie outside of the cylinder circumference, they make a loop-like movement. If the contact points lie inside of the cylinder circumference, they make a wave-like movement. Figure 6.4 shows this principle in an exaggerated form. The male die is compared to situation a in Figure 6.4 and the female die is compared with situation b. The next section describes the FEA setup.

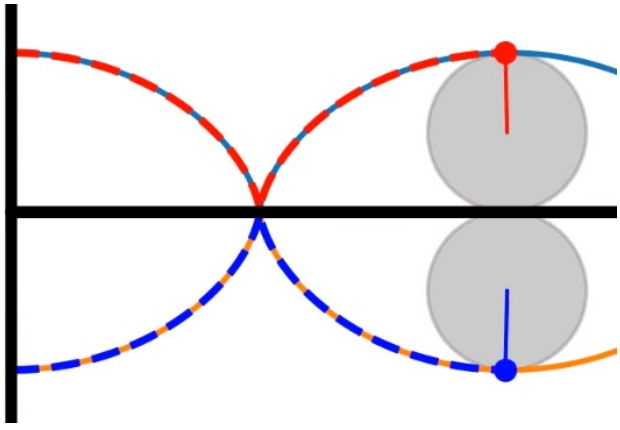

Figure 6.2: *Rotational movement of dies seen from a fixed web.*

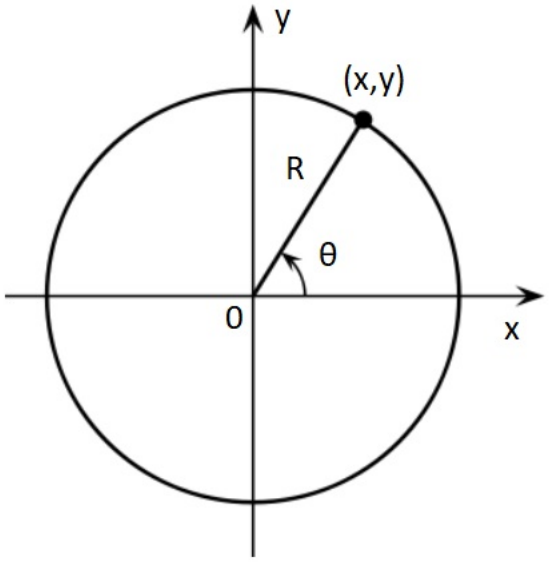

Figure 6.3: *Coordinate system cylinder.*

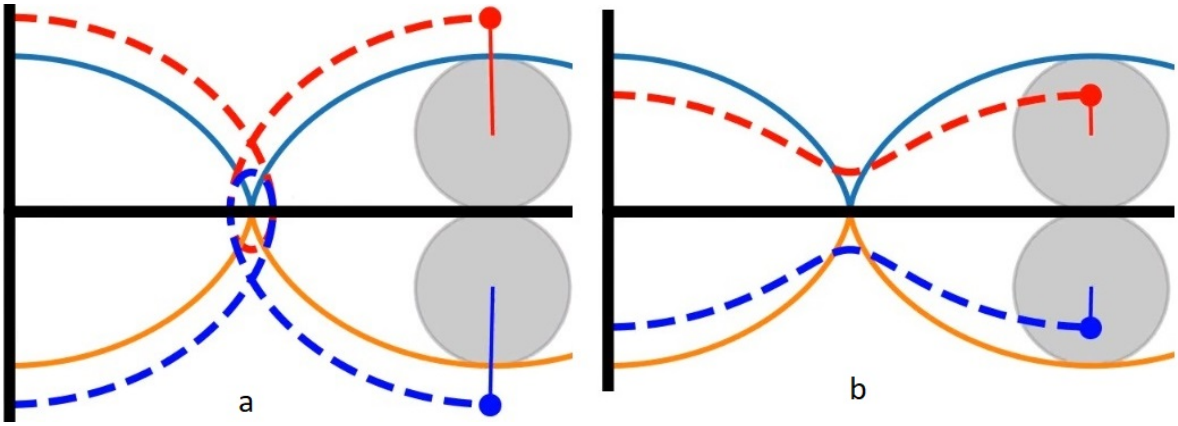

Figure 6.4: *Rotational movement die: (a) extended movement and (b) concentrated movement.*

6.3 FEA setup

There are many settings and setups in FEA software. The most important settings are element types, boundary conditions and contact. They are elaborated in the next subsections.

6.3.1 Element type

The sheet element types are CPS4R: a 4-node bilinear plane stress quadrilateral. The dies are single lined rigid bodies, which require rigid elements. Rigid bodies do not deform and therefore the elements should not deform.

6.3.2 Boundary conditions

Boundary conditions can help simulations become more accurate. For this case, there are no boundary conditions applied to the sheet ends. This means that the sheet is free to move in x, y and rotational directions. The ends are not fixed or restricted but the sheet cannot pass through the die and cylinder. The fact that the ends are free, means that material draw-in is allowed.

A single channel simulation is expected to allow more material draw-in than multiple channels. This is simulated by a model where the sides are allowed to draw inwards. Multiple channels can influence adjacent channels. For example, a channel with adjacent channels on both sides, is expected to restrict material draw-in and enhance material stretching. This is simulated as a single channel with fixed sides.

Correct boundary conditions are essential for simulating multiple forming orientations and configurations. Understanding the physical geometries and processes that occur during rotary conversion are key to good simulations.

6.3.3 Contact

The contact property option, specifies the contact type and stops the sheet from passing through the cylinder or die. It specifies which surfaces collide and interact with each other. For example, the male and female dies interact with the sheet. The contact is set to surface-to-surface contact and is explicit. The mechanical constrain formulation is set to penalty contact method. This allows for friction to be implemented through a friction coefficient. Friction is elaborated in the next section.

6.4 FEA validation

The FEA simulations are validated according to the experiments described in Section 4.2. These experiments result in thickness variations in the deformed sheet and they are measured as described in Section 5.2. The FEA simulations and experiments are compared to each other. The simulations should resemble the experiments, up to a certain degree of accuracy, to be able to use FEA simulation for more extensive research. First, a mesh size convergence study is performed and after that the simulations are validated.

6.4.1 Mesh size convergence study

Many continuous objects have infinite degrees of freedom which makes it difficult to solve using hand calculations. FEA software divides the objects in sections or elements. All the deformed elements together form the final deformed shape of the whole object.

FEA simulation results are mesh size dependent. Therefore, a mesh size convergence study should be performed. The goal of a mesh size study is to map mesh size against results. This means that the mesh size is reduced until the results converge. If the results are converged for a specific mesh size, an even finer mesh only results in more computational time and not more accuracy.

The FEA simulation consists of a sheet, male and female die. The dies are modelled as rigid bodies and the sheet is modelled as a deformable body. The sheet mesh size is varied and compared against the results. The sheet mesh size can vary in through thickness and length directions.

The thickness, in the four corners, is measured and compared to the experiment. The mesh size that represents the experiments with lowest error, is the best mesh size for these experiments. The element height and length have been varied from 0.005 up to 0.02 mm. The sheet length is 60 mm, but it is partitioned into 5 areas. The areas that deforms the most are of interest. This is at or close to the die contact area. The rest of the sheet hardly shows any deformation. The sheet is divided in a fine, medium and large mesh area. Figure 6.5 shows the sheet mesh partitions.

The element height is constant but the element length varies throughout the whole sheet. The element length is varied between these partitions, which is beneficial for computational time. The large element section has a length of 25 mm. The medium element section has a length of 3.5 mm and the fine mesh section has a length of 3 mm. The best results were gained with both element height and length of 0.01 mm. The medium mesh area has a larger element length of 0.14 mm

and the large mesh area has element length of 2.5 mm. Figure 6.6 shows the fine element section of the sheet.

It should be noted that the mesh should follow the correct shape. For example, in rounded corners, there should be enough mesh density to ensure the smoothness of the curve. If this is not the case then discrepancies can occur in the corners. The elements should be spread evenly over the surface in a uniform shape and orientation.

The mesh size convergence study results are shown in Figure 6.7. The mesh for the fine part of the sheet are varied in height and length. The results for 0.01 mm mesh size are very similar to the results for 0.005 mm mesh. However, the computational time for mesh size of 0.005 mm was three times longer. If the results are satisfactory and converged, there is no need for a finer mesh because it will only take more computational time. Therefore, the best results are gained with a mesh size of 0.01 mm.

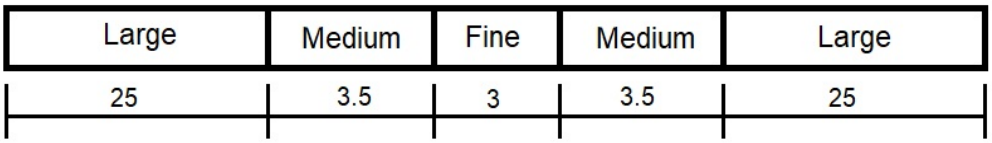

Figure 6.5: *Mesh partitions sheet.*

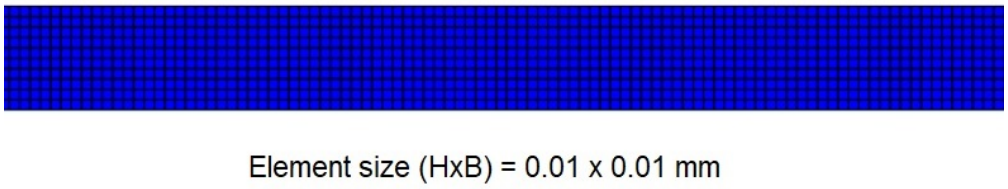

Figure 6.6: *Fine mesh configuration on the middle part of the sheet.*

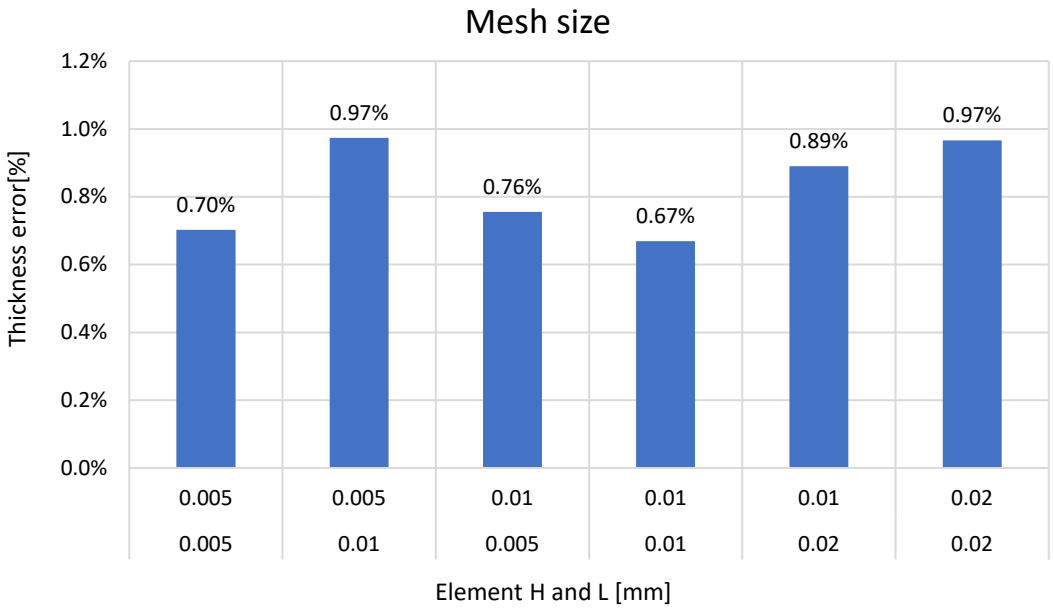

Figure 6.7: *Mesh size convergence study results.*

6.4.2 Friction

In the first set of simulations, the friction between dies and sheet was set to zero friction. For optimum results, the friction should be experimentally measured. However, this is difficult to measure and the tools to measure friction were not available at Madern. During the experiment, no lubrication is applied.

The kinematic friction coefficient, for FEA simulation, is found by trial and error. Starting from frictionless up to a friction coefficient of 0.3. These simulations are based on clean and dry surfaces without lubrication. The error calculation was based on the thickness measurement at the four bends. For each friction coefficient, the simulation thickness is measured and compared to the experimental thickness. Figure 6.8 shows the results. The friction coefficient of 0.15 gained the best results with the lowest error.

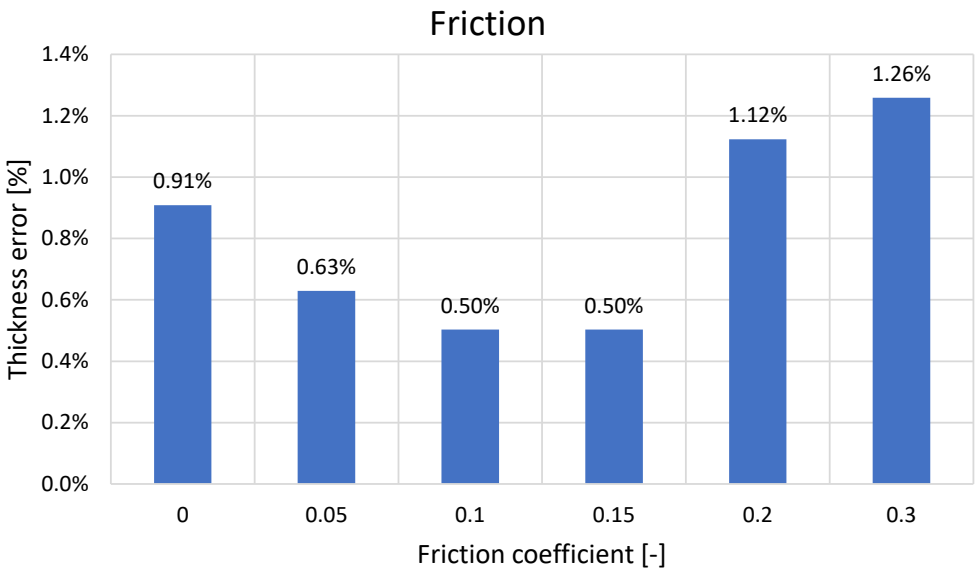

Figure 6.8: *Thickness error for different friction coefficients.*

6.4.3 Thickness

The experiments are simulated in FEA software and need to be validated. The mesh size is now converged and friction is applied thus the simulations can be validated. This is done by comparing the experimental data with FEA data. For the validation, experimental thickness variations are compared to FEA simulations.

The simulations are performed with 0.2, 0.3 and 0.4 mm shim. The thickness reduction in the four corners, as defined in Figure 5.1, is measured, and the average sheet thickness is measured. These measurements are then compared to the experimental results. Best results are gained with a mesh size of 0.01 mm, a friction coefficient of 0.15 and a strain rate of 4.369 s^{-1}. The validation for web and cross-web directions are discussed in the next two sections.

For 2D simulations of web direction channels, it is assumed that the forming process is similar to normal stamping. This means that the dies do not move in X direction or rotate. It is simulated as a die that move in Y direction only. For cross-web direction channels, the dies translate and rotate to simulate the rotary forming process as close as possible.

Figure 6.9 shows the thickness error at each bend. It can be clearly concluded that the cross-web channel results are more accurate than web direction channels. The maximum error for cross-web direction is 3.06% and the maximum error for web direction is 8.83%.

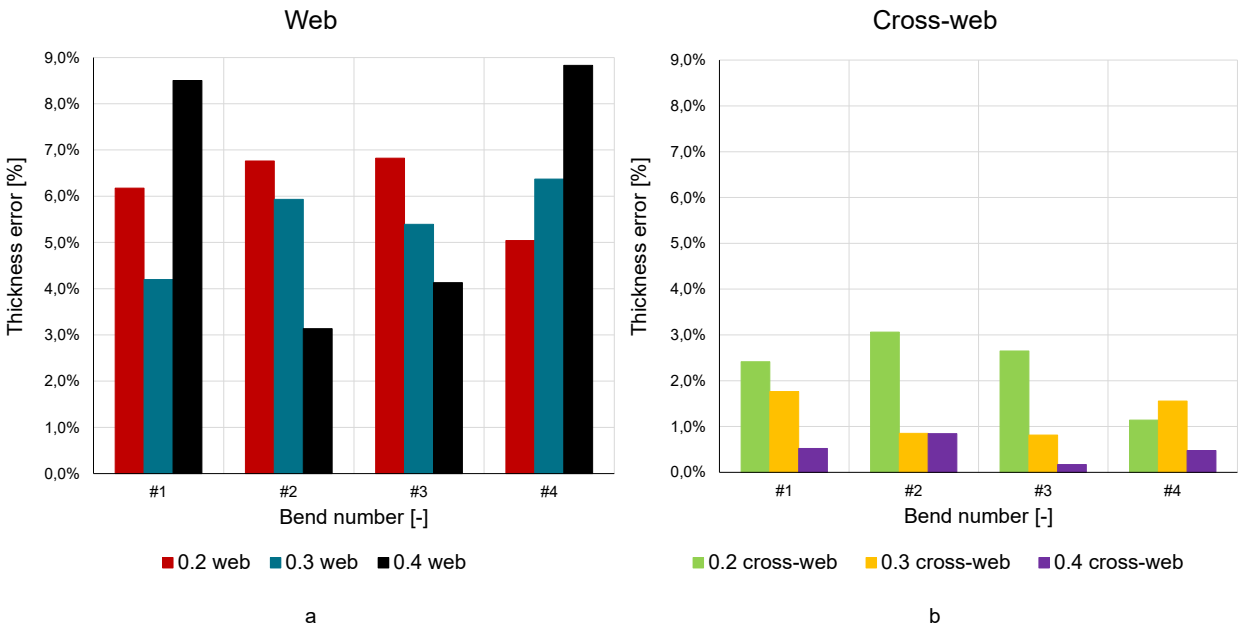

Figure 6.9: *Thickness error results: (a) web and (b) cross-web.*

6.5 FEA results

The FEA deformed shapes are evaluated against the experiments. However, FEA simulation can provide more information than just the experiments. For example, the final experimental and simulation shapes are compared. Another variable is equivalent plastic strain and it compares plastic strain behaviour of experiments and simulations. Furthermore, the simulations show stress magnitudes and concentrations on the specimen. Lastly, springback is evaluated by simulations showing the deformed shape for distinct die indentation depths. These variables are discussed in the next sections.

6.5.1 Shape

In this section the final experimental and simulation shapes are compared. The simulation shape should resemble the experimentally deformed specimen shape. The overall cross-sectional shape is compared to the experiments. The shapes are overlapped in six figures and are shown in Appendix C. The FEA fine meshed sheet area is compared to the experimental final shape. The fine meshed sheet section is approximately 3 mm in length.

Figure 6.10 shows the results for 0.4 mm shim thickness channel in cross-web direction. The black lines resemble the experimental shape and the red lines the FEA shape. It can be concluded that the FEA shape matches the experimental shape relatively good. However, this is not the case for the web direction channels. The FEA simulation of cross-web channels match the experiments a lot better than web direction. This could be due to die misalignment. Another explanation could be that the plane strain condition is not completely valid for web direction. The shapes are overlapping but the original axis systems for simulation and experiments were not located at the same origin. The shapes are aligned and rotated by hand to overlap each other as close as possible.

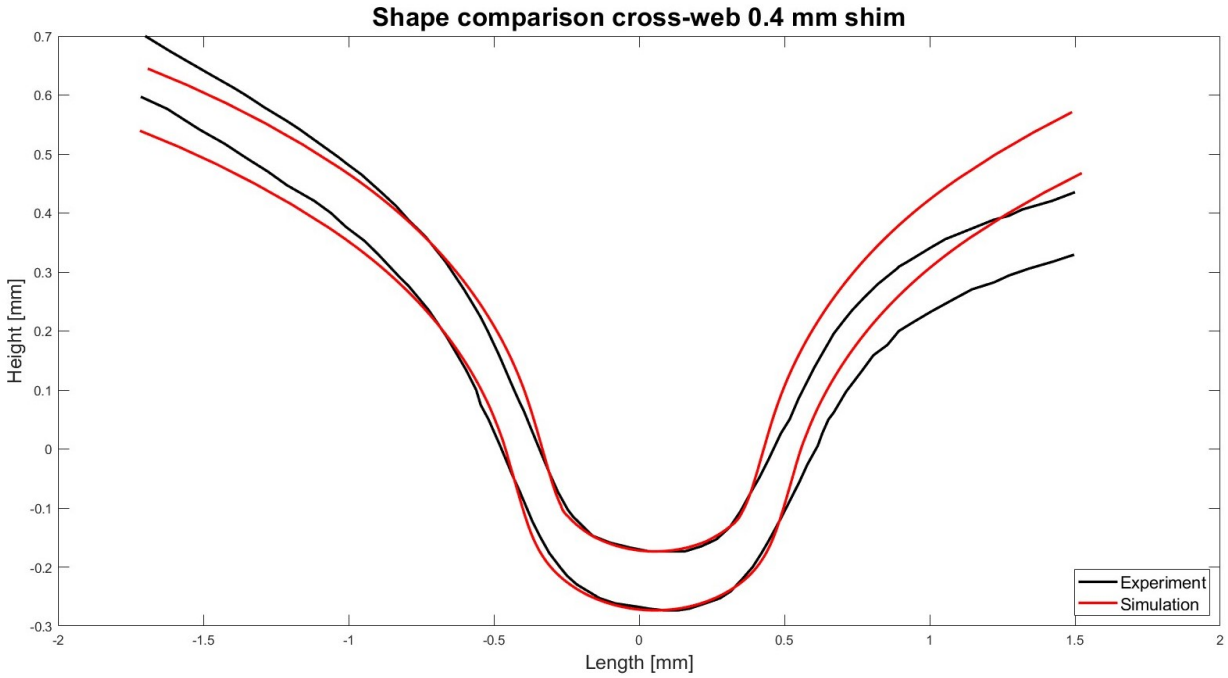

Figure 6.10: *Experimental and FEA shape comparison for a channel in cross-web direction for 0.4 mm shim.*

6.5.2 Equivalent plastic strain

The equivalent plastic strain for simulations and experiments is compared to each other to check the BPP plastic behaviour. It is expected that the equivalent plastic strain for simulations and for experiments should be equal or similar to each other. This shows if the plasticity strain magnitude is similar to each other. The plastic equivalent strain for simulations is the PEEQ values taken from simulations. The plastic equivalent strain for experiments is calculated as follows:

$$\varepsilon_{ep} = \frac{\sqrt{3}}{2}\sqrt{(\varepsilon_c - \varepsilon_{cc})^2 + (\varepsilon_c - \varepsilon_t)^2 + (\varepsilon_{cc} - \varepsilon_t)^2 + 6(\varepsilon_{c,cc}^2 + \varepsilon_{cc,t}^2 + \varepsilon_{c,t}^2)} \tag{6.3}$$

where, ε_c is channel strain, ε_{cc} is cross-channel strain, ε_t is thickness strain and $\varepsilon_{c,cc}$, $\varepsilon_{cc,t}$ and $\varepsilon_{c,t}$ are shear strains. The shear strains are not of interest and the plane strain assumption is applied. This sets channel strain to zero and equals the thickness strain to minus the cross-channel strain. For example, ε_c = 0 and ε_t = - ε_{cc} results in:

$$\varepsilon_{ep} = \frac{\sqrt{3}}{2}\sqrt{(-\varepsilon_{cc})^2 + (\varepsilon_{cc})^2 + (2\varepsilon_{cc})^2} = \frac{\sqrt{3}}{2}\sqrt{6\varepsilon_{cc}^2} \tag{6.4}$$

which is compared to the plastic equivalent strain (PEEQ) results from FEA. The simulation and experimental results are compared at each bend. The maximum PEEQ occurs on the outsides of the bends. The strain from Chapter 5 at bend three is used as input for Equation 6.4. Figure 6.11 show the plastic equivalent strain results.

It can be concluded that for 0.2 web direction the FEA simulation underestimates the strain up to five and a half times compared to the experimental results. For 0.4 web, the FEA results are underestimated up to eight times. The FEA shape of bends one and four are less sharp than the experimental bends. This results in a lower strain for the FEA simulations. Bends two and three are more similar to the experiments. However, for 0.3 web, the FEA strain is larger than the experimental strain results.

For cross-web direction, the FEA plastic equivalent strain is increasing for increasing shim thickness. Which is as expected because more shim equals higher die indentation and this causes more strain. The experimental results are not intuitive either because the strains are not increasing for increasing shim thickness. It is increasing from 0.2 to 0.3 mm shim thickness. However, from 0.3 to 0.4 mm shim thickness the strain is decreasing. It could be due to die misalignment or measurement error.

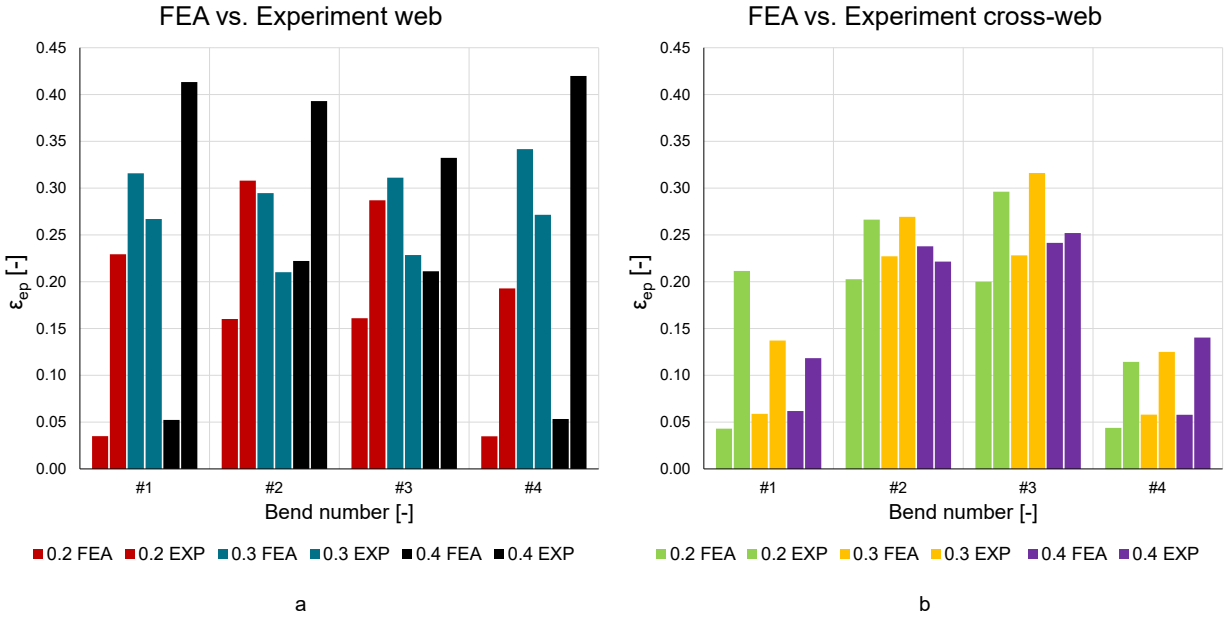

Figure 6.11: *Equivalent plastic strain results for FEA simulations and experiments: (a) web and (b) cross-web.*

6.5.3 Stress

The maximum Von Mises stresses are taken from FEA simulations. In each bend a stress concentration is observed. The maximum stresses are taken in the four bent areas and shown in Figure 6.12.

For web direction, it can be concluded that the stresses in bends one and four are very close to the yield stress. This means that the material just starts to plastically deform in bend one and four. Full plastic deformation is probably not present in bends one and four. However, the stresses in bends two and three are much higher with peaks up to 1100 MPa. In bends two and three almost full plastic deformation is expected.

For cross-web direction, it can be concluded that all stresses are higher than the yield stress. The same trend occurs as in web direction, where the stresses in bends tow and three are much higher than stresses in bends one and four. The peak stress is 1200 MPa and occurs in bend three for 0.4 mm shim.

A reason for the lower stresses in bends one and four could be that the bending radius is larger in these bends. The first and fourth bend shapes are less sharp and therefore the stresses are lower.

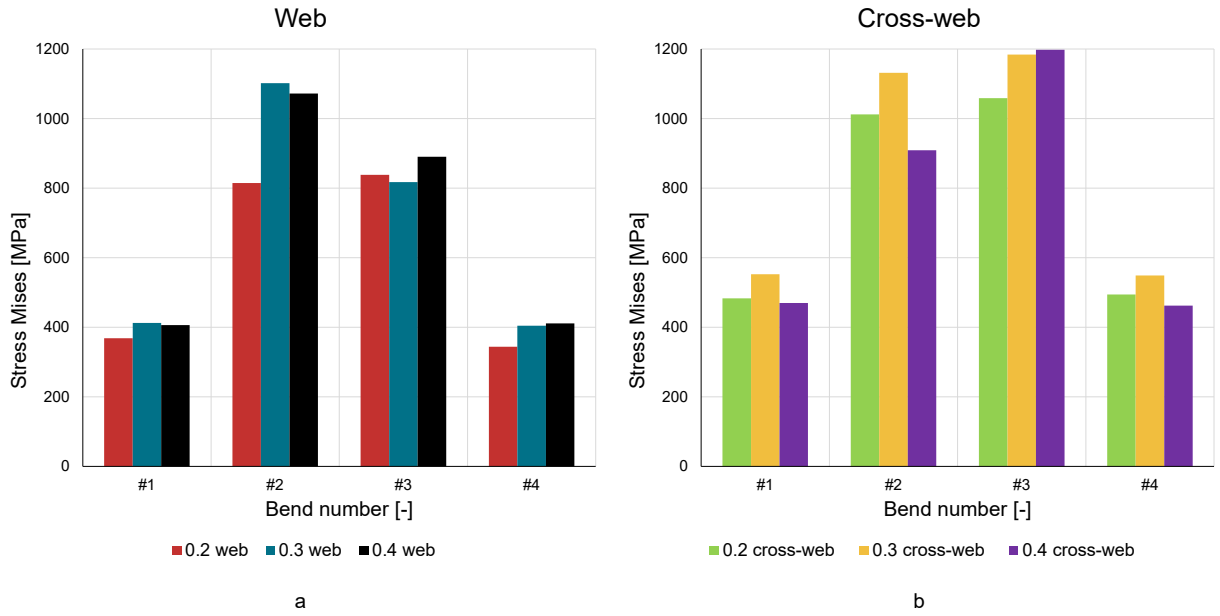

Figure 6.12: *Maximum Von Mises stress at each corner: (a) web and (b) cross-web.*

6.5.4 Springback

The specimen deforms upon loading. When unloading, the specimen partially forms back to its initial shape. In the experimental setup of this research, springback could not be measured. However, in simulation, springback is present upon unloading and could be measured. The simulation is split up into two parts, the loading and unloading part. During the loading part, the sheet is deformed from its initial shape to its maximum deformed shape. During unloading, the dies are retreated and tension on the sheet is released.

Figure 6.13 shows the unloading part of the sheet shape for different die indentation depths. The blue lines represent the male and female die at its largest indentation depth. At D_0, the male die is at its largest indentation depth. Therefore, the deformation is at its maximum. After D_0, the male die moves up again and the sheet moves slightly back to its initial shape. The simulation runs from D_0 up to D_4 and it is represented by the different colour lines. The lines D_3 and D_4 overlap each other meaning that the shape stays constant and spring back has died out. All springback results for different simulations are shown in Appendix D.

Figure 6.14 illustrates the Y translation for different die indentation depth. This point, indicated with a diamond in Figure 6.13, starts from its lowest position at D_0 and moves up. At D_0 the die starts moving up again and starts unloading the sheet. This means that spring back occurs from D_0 up to D_3 and after reaching D_3 the Y translation stays constant. This is conform the results from Figure 6.13.

Springback is quantified as distance from the maximum deformed shape to the final shape. The maximum springback amount is 0.079 mm and occurs in cross-web direction for 0.4 mm shim thickness. Figure 6.15 shows the amount of springback.

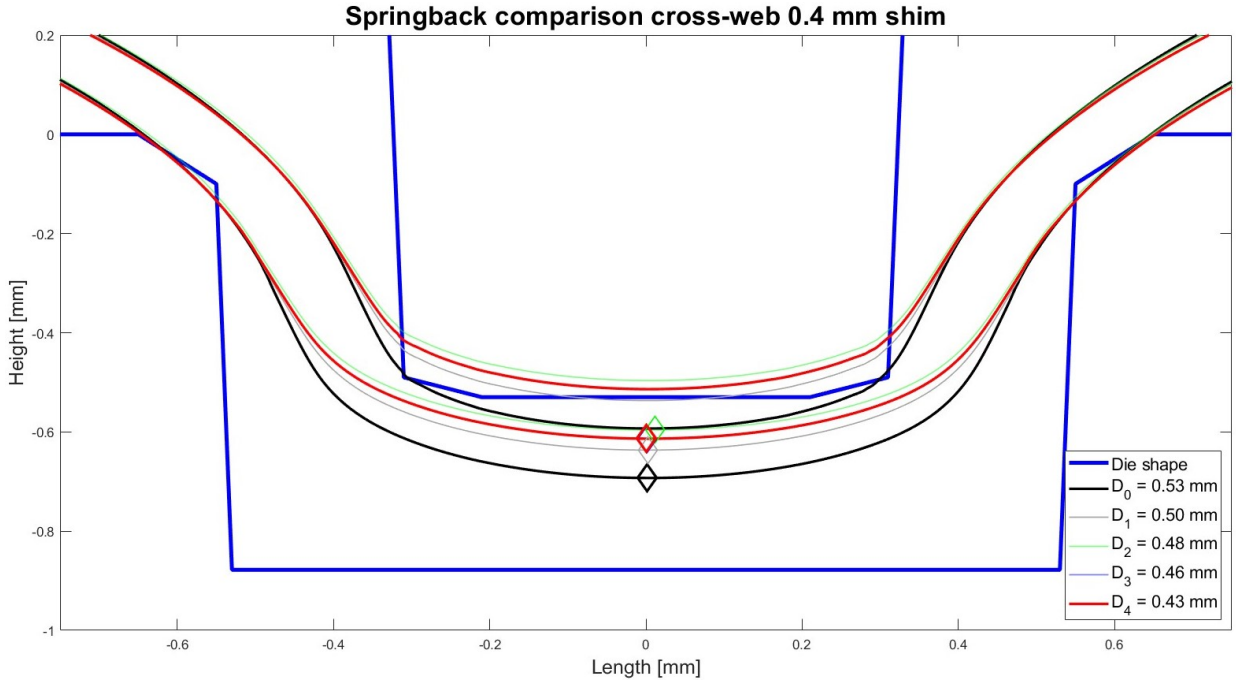

Figure 6.13: *FEA springback comparison for a channel in cross-web direction for 0.4 mm shim.*

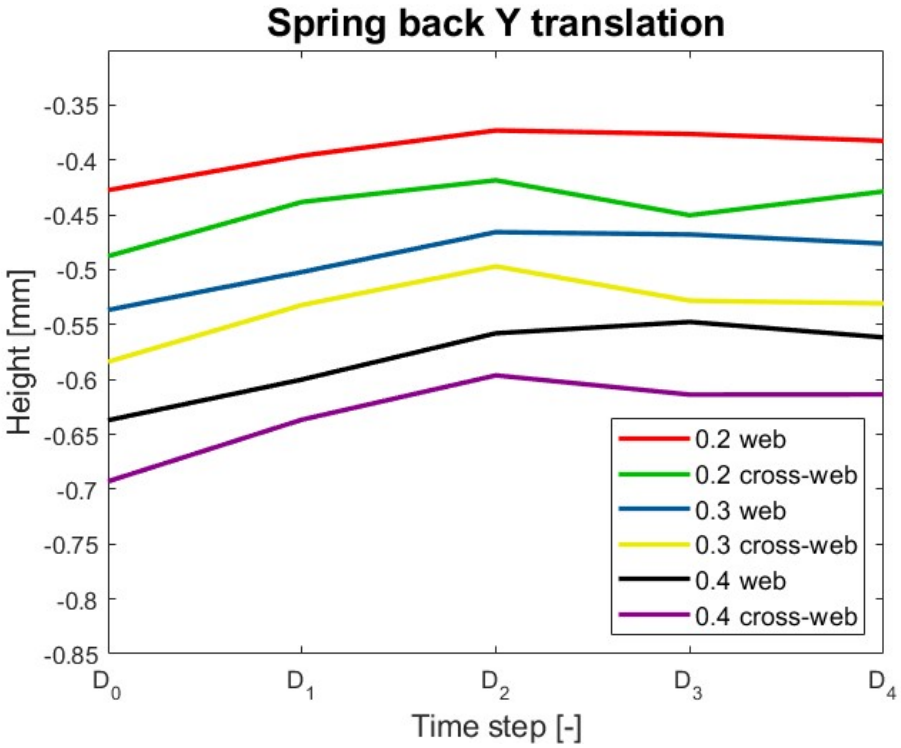

Figure 6.14: *Y translation in time for each configuration.*

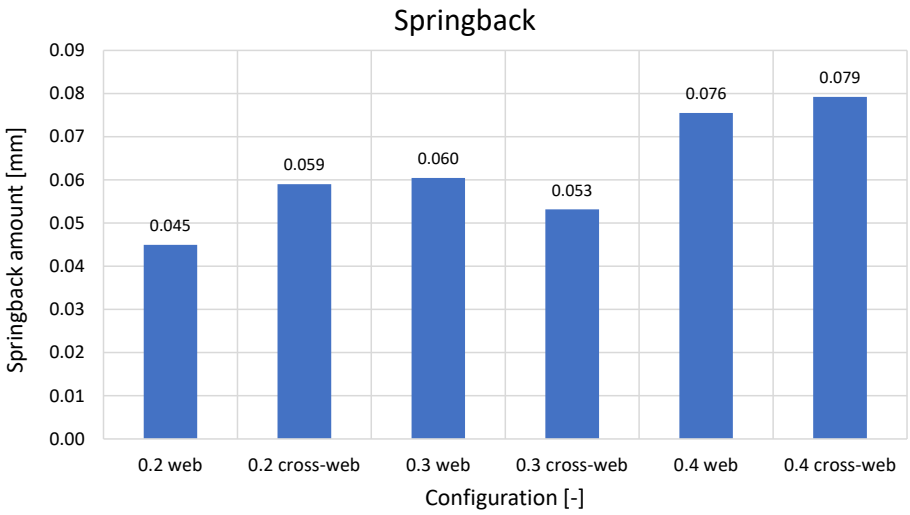

Figure 6.15: *FEA absolute springback amount.*

7 Discussion

The mechanical properties are only tested in tensile tension. Whereas the specimen also encounters compressive bending strain. Large parts of the bending areas are reduced in thickness suggesting that the membrane strain in this bend is positive or tensile. The tensile testing is performed with lower strain rates than the foreseeable production process. The mechanical properties are corrected for the experimental strain rate. However, the final production speed and strain rates are unknown.

The thickness strain measurement accuracy depends on measurement point selection and microscopic resolution. The measurements are point measurements and they are selected by hand on a microscopic picture. The cross-sections are digitised and could also be used for thickness measurements. This would get the thickness over the entire cross-section instead of local point thickness measurements. However, the digitisation is a manual process as well and its accuracy is dependent on the number of points and accuracy of point selection. The areas of interest are the bent areas where bending and membrane strain is measured. Therefore, point measurements are taken in the bent areas. For each corner, three measurement points are selected and averaged for strain calculations. If the area of interest is the whole cross-section, it could be better to measure thickness over the whole cross-section. This means that areas with most material thinning can be identified over the cross-section.

The cross-web bending strain in bend three is always larger than in bend two. This could be due to the misalignment of dies. Looking at figures, Figure B.4, Figure B.5 and Figure B.6, it could be the case that, the die clearance in bend two is larger than in bend three. A larger die clearance leads to a larger bending radius and thus lower strain. The dies are aligned perfectly in FEA and the FEA results shown in Figure 6.11 part b contradict the experimental results. For cross-web, strain in bend two is larger than strain in bend three. It could be because bend two get the initial first touch between sheet and die. As the male die moves down, it is inclined slightly because of the rotary process.

The sheet curvature is only measured over a relatively short distance. It is measured over the distance covered by the microscopic picture that is used to measure the thickness strains. The measurement width is approximately 34 mm. The measurements are taken over the most straight surfaces away from the channel edges. However, it is observed that the sheets are not straight anymore after forming. It could be because bending strains are more dominant than membrane strains. The sheet curvature is only measured for the experiments because the sheets from FEA simulations do not have a straight part to measure the angle.

The membrane strain accuracy entirely depends on the determination accuracy of thickness reduction and conformity to the plane strain assumption. This means that errors in thickness strain are influencing the membrane strain accuracy.

The equivalent plastic strain determined in FEA for web direction in bends one and four are always smaller than the experiment values. This could be up to three times as small. The FEA final and experimental shape are comparable for bends two and three. However, deviations are shown in bends one and four for web direction and less deviations are shown for cross-web directions. This means that web direction FEA results do not resemble the experiments. For FEA simulations, the bending radii in bends one and four are overestimated resulting in less plastic strain. This could be due to final shape deviation or not applicable assumption of plain strain condition.

8 Conclusions and Recommendations

8.1 Conclusions

The research question was introduced in the introduction and defined as: *"What are the bending and membrane strain components of a single channel in 0.1 mm thick SS316L sheet formed by rotary conversion?"*

Overall, the web direction has higher thickness, bending and membrane strains than the cross-web direction. For both directions, the thickness strains are negative because the thickness is reduced. The bending strains are larger than the membrane strains. This would imply that the channels are more bending dominated than membrane dominated.

More bending dominated strain is confirmed by the experiments as well as FEA simulations. The sheet straightness is lost after each experiment. Before the experiments, the sheets were straight and after the experiments, each sheet was curved. The results from Appendix A and Appendix C confirm this phenomenon. The sheet curvature, for both web and cross-web direction, is gradually getting worse with increasing shim thickness. However, the sheet curvature is worse for the cross-web direction. In cross-web direction, the sheet is less restricted to bending because it can follow the cylinder radius. However, in web direction, the sheet is more restricted to bending because it hits the cylinder.

Bending strain domination was expected because the channels are not fixed on the sides. Material draw-in is allowed, which implies that material thinning is less severe than is expected for fixed channels. This phenomenon is as expected, however not experimentally confirmed, because only single channels are experimentally tested.

The plane strain condition is confirmed experimentally. The plane strain experiments confirm material straining in cross channel direction. The engraved grid does not show deformation in channel direction. This is valid for both channels in web and cross-web directions.

The mechanical properties are tested using a tensile test. The stress-strain results are depending on strain rate. The Cowper-Symonds model relates strain rate to stress-strain curve. Therefore, it is important to calculate the desired production process strain rate. The FEA simulations depend on correct mechanical properties because they are used as input.

The FEA simulations for cross-web channels show good comparison for measured thickness reductions, final shape and equivalent plastic strain. However, this is not necessarily the case for web direction channels. The final shape and thickness are deviating more for web channels than for cross-web channels.

8.2 Recommendations

The mechanical properties are determined by tensile testing. The results are corrected for true stress and strain rate. As the thicknesses are very small, it could be beneficial to research the grain size and direction. However, this could be more relevant to the steel manufacturing process and heat treatment of SS316L. In this research, the grain size and direction are not researched due to lack of resources and time. The same accounts for strain hardening, strain hardening due to forming processes can have an influence on the material strength.

For deeper and fixed channels, it is expected that membrane strain increases. This is because they restrict material draw-in and rely more on (deep) drawing than bending. However, when the channels get deeper, the bending radii are reducing as well. This causes bending strain to increase as well, this is especially the case for web direction. Further research could tell if there is an optimum between bending and membrane strain for different channels. Especially with respect to material failure limits.

The FEA simulations are in 2D, which for the uni-directional bending and plane strain assumption, the results are represented very well by 2D simulations. However, when the die geometries become more complex, and therefore also more realistic, 3D simulations could be considered. A simple step could be to simulate or experiment with multiple adjacent channels. The effects of friction and springback could play a more important role in more complex 3D simulations.

Springback is expected to cause problems for the geometric consistency of more complex BPP designs. From the FEA simulations, it is concluded that springback is present. However, it seems to be relatively small and it is not the main goal of this research. Springback is researched with the help of experiments and FEA simulations, but due to lack of time and resources it is not researched in this thesis.

The cylinder rotational speed determines the strain rate. However, for the experiments, the cylinders were turned by hand. It would be better to rotate the cylinders with an electric motor. The electric motor speed should be controlled to reenact the intended production speed. This would take the experiments a step closer to the production process, especially for the strain rate.

The eventual goal is to produce BPPs by rotary conversion. It is expected that geometrical consistency and springback could cause problems for this production process. More research into eventual springback could make a positive impact on the research. However, this does not mean that springback is always present and causes problems.

Appendix A shows sheet curvature for the formed channels. The sheets need to be straight, for its function as BPP. For geometrical consistency, this bending component should be counteracted or removed. Further research should exclude the overall BPP sheet bending.

The eventual goal is to simulate the experiments as closely as possible. When accurate FEA modelling is achieved, the design and process optimisation can start. The purpose is to optimise the rotary forming process and die design with regards to springback, stress, strain, geometry, geometrical consistency and material failure limits. Eventually, the FEA models could be extended to much more complex geometries and 3D simulations. Again, with more complex models, the process and design optimisation can start. However, this is too big a scope for this research. Nevertheless, knowledge gained in this research could be used for future rotary forming process optimisation and FEA modelling.

A | Thickness measurements

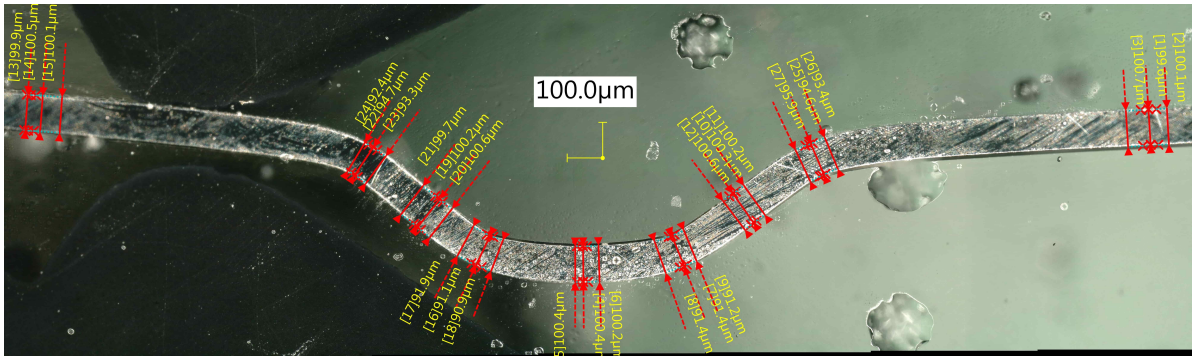

Figure A.1: *Thickness measurement, web, 0.2 mm shim.*

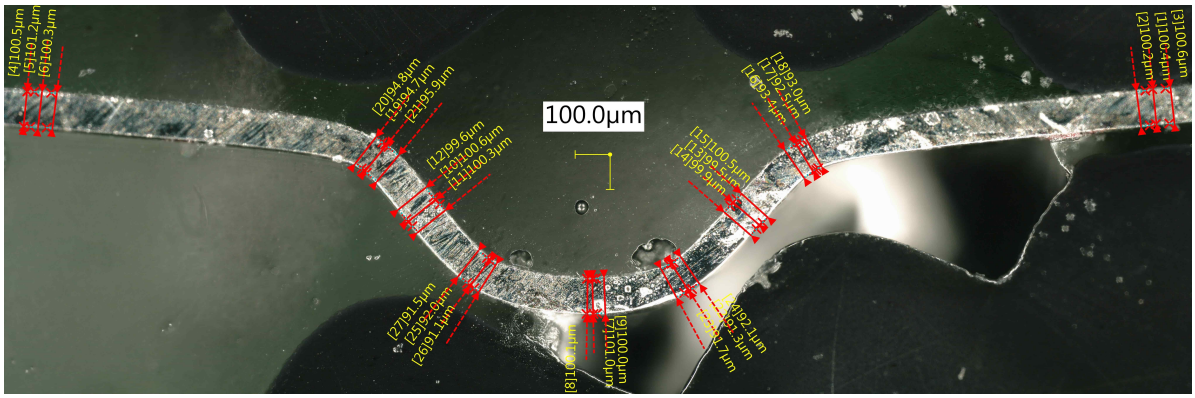

Figure A.2: *Thickness measurement, web, 0.3 mm shim.*

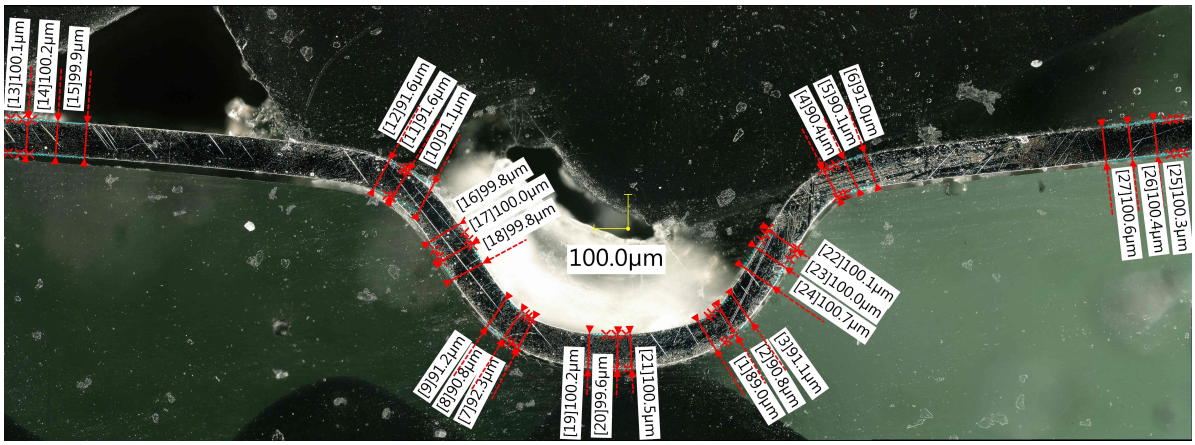

Figure A.3: *Thickness measurement, web, 0.4 mm shim.*

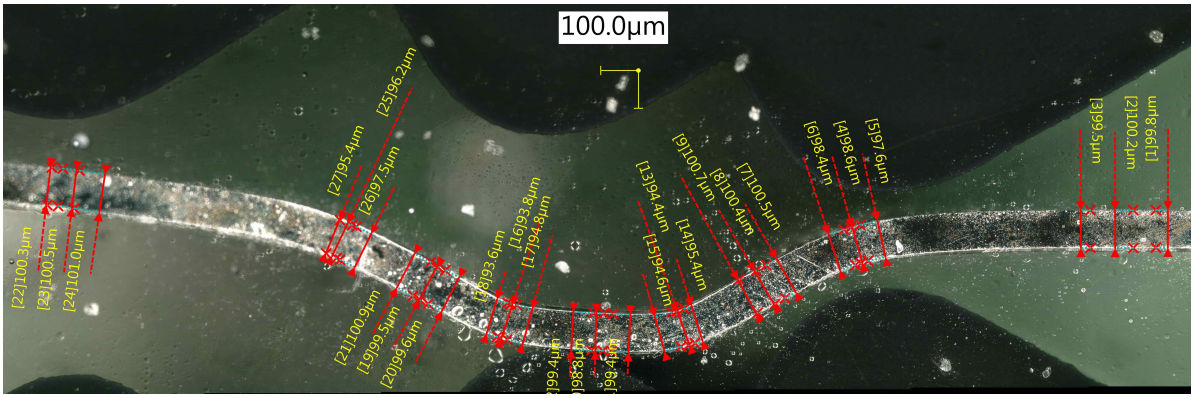

Figure A.4: *Thickness measurement, cross-web, 0.2 mm shim.*

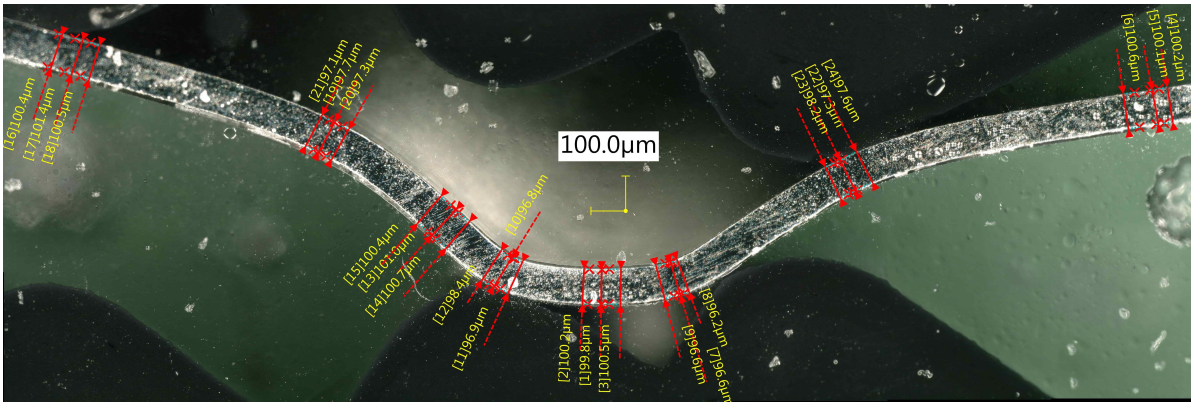

Figure A.5: *Thickness measurement, cross-web, 0.3 mm shim.*

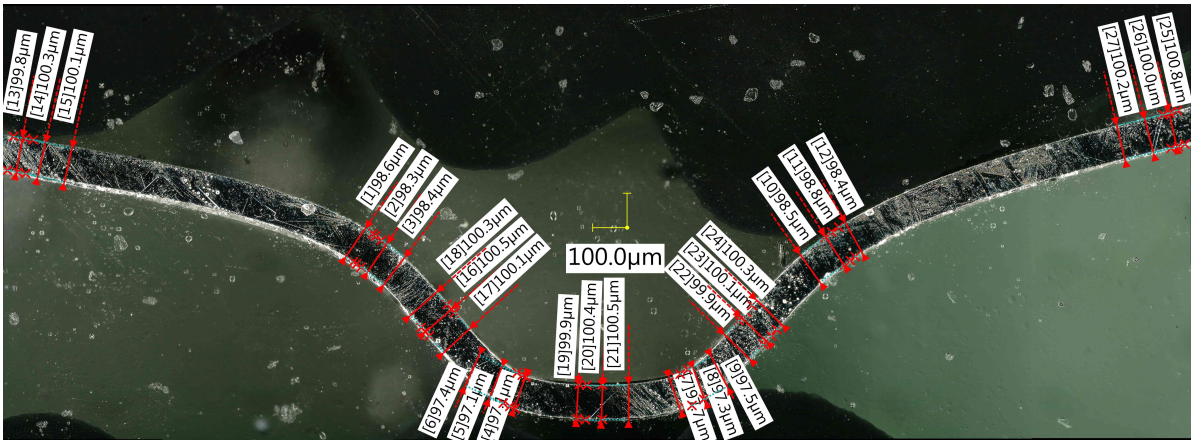

Figure A.6: *Thickness measurement, cross-web, 0.4 mm shim.*

B | Bending radius measurements

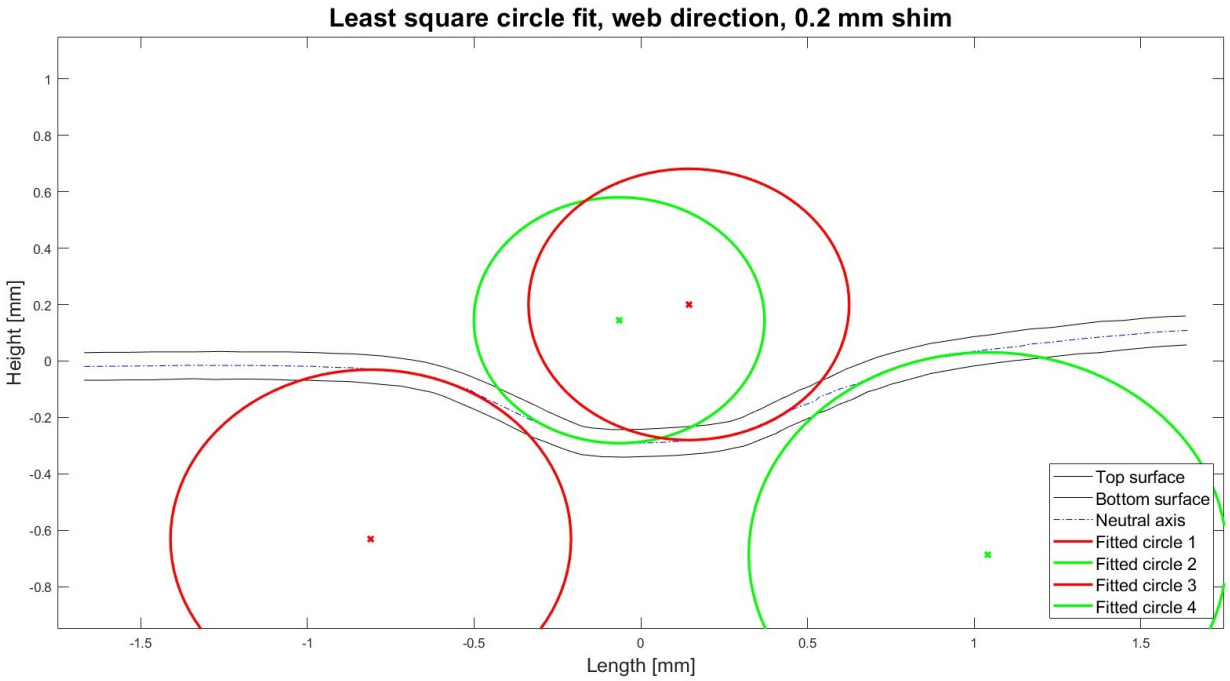

Figure B.1: *Bending strain measurement, web, 0.2 mm shim.*

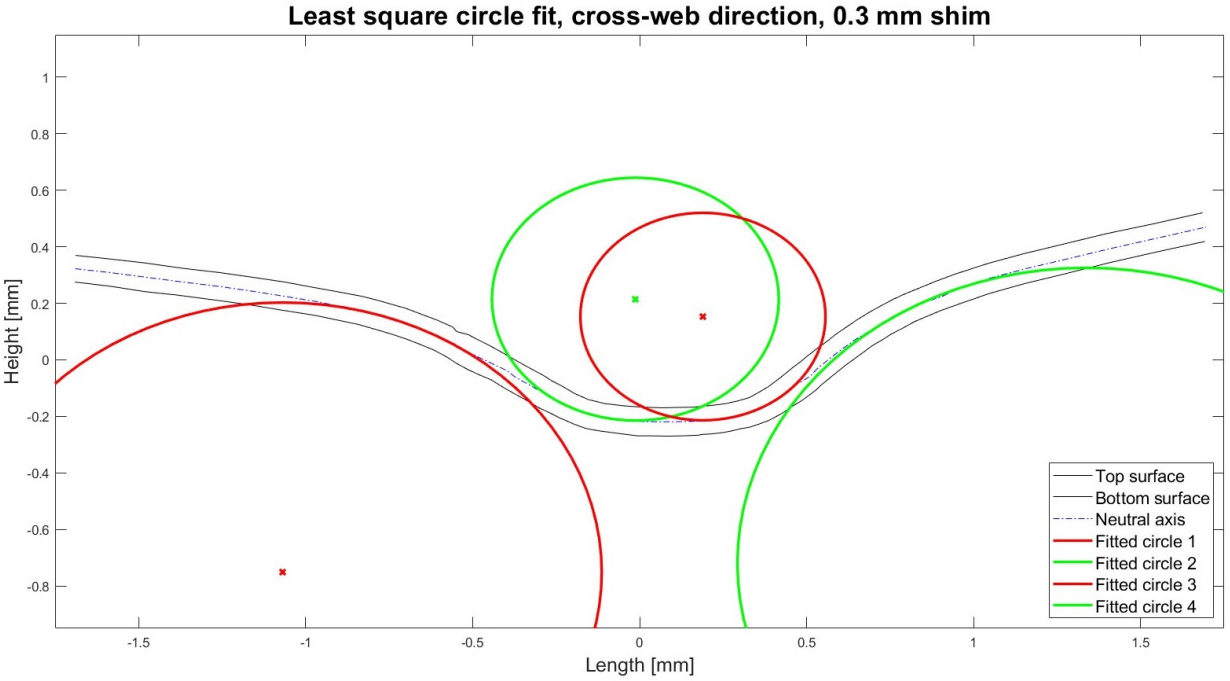

Figure B.2: *Bending strain measurement, web, 0.3 mm shim.*

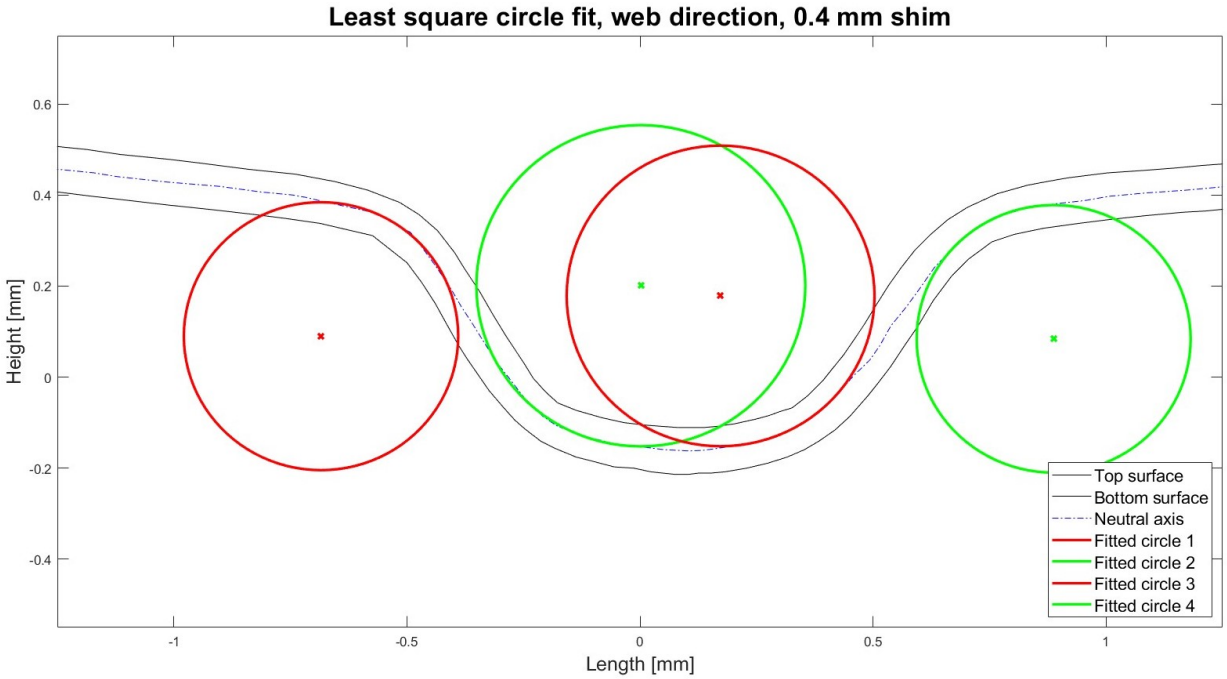

Figure B.3: *Bending strain measurement, web, 0.4 mm shim.*

Table B.1: *Bending radii and strain results for web and 0.2 mm shim.*

# [-]	y $[mm]$	r $[mm]$	ε_{ben} [-]	$interval$ [-]	# $points$ [-]
1	0.0468	0.601	0.078	(-0.85; -0.55)	6
2	0.0457	0.436	-0.105	(-0.3; 0.0)	8
3	0.0457	0.481	-0.095	(0.2; 0.45)	7
4	0.0473	0.717	0.066	(0.75; 1.0)	5

Table B.2: *Bending radii and strain results for web and 0.3 mm shim.*

# [-]	y $[mm]$	r $[mm]$	ε_{ben} [-]	$interval$ [-]	# $points$ [-]
1	0.0476	0.378	0.126	(-0.8; -0.5)	7
2	0.0458	0.462	-0.099	(-0.3; 0.0)	9
3	0.0459	0.426	-0.108	(0.2; 0.6)	12
4	0.0465	0.363	0.128	(0.65; 1.0)	7

Table B.3: *Bending radii and strain results for web and 0.4 mm shim.*

# [-]	y $[mm]$	r $[mm]$	ε_{ben} [-]	$interval$ [-]	# $points$ [-]
1	0.0457	0.294	0.155	(-0.7; -0.4)	6
2	0.0457	0.353	-0.146	(-0.35; 0.05)	11
3	0.0452	0.330	-0.112	(0.2; 0.45)	8
4	0.0453	0.294	0.154	(0.65; 0.9)	5

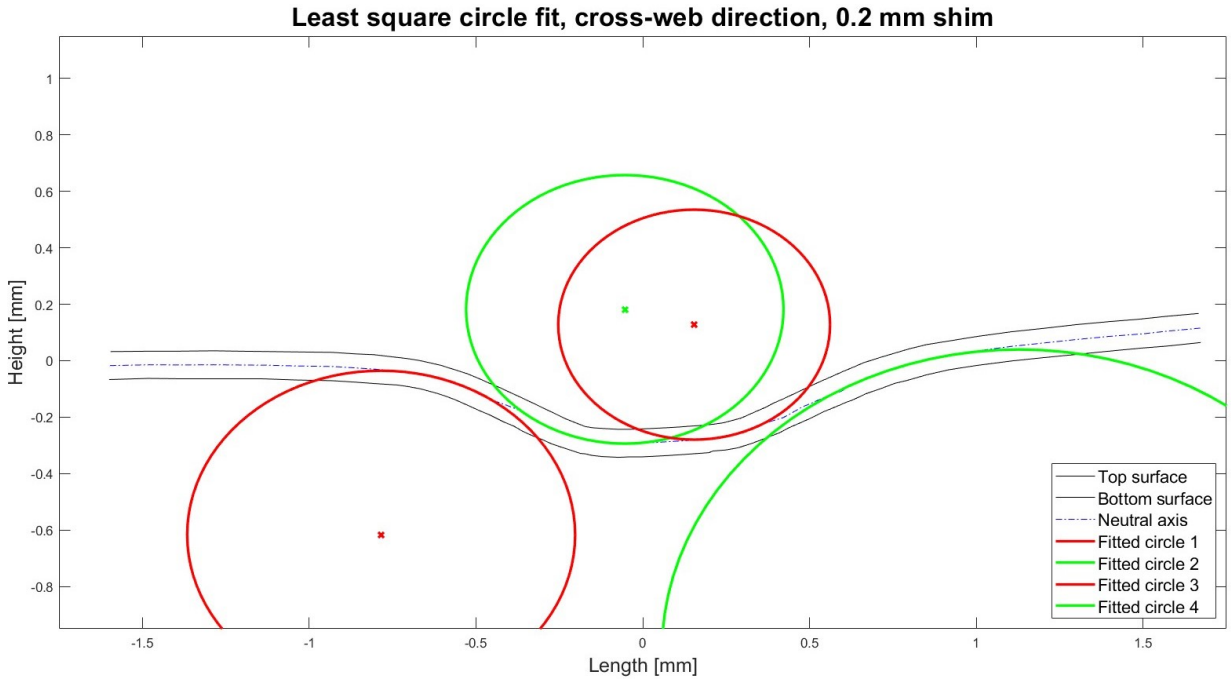

Figure B.4: *Bending strain measurement, cross-web, 0.2 mm shim.*

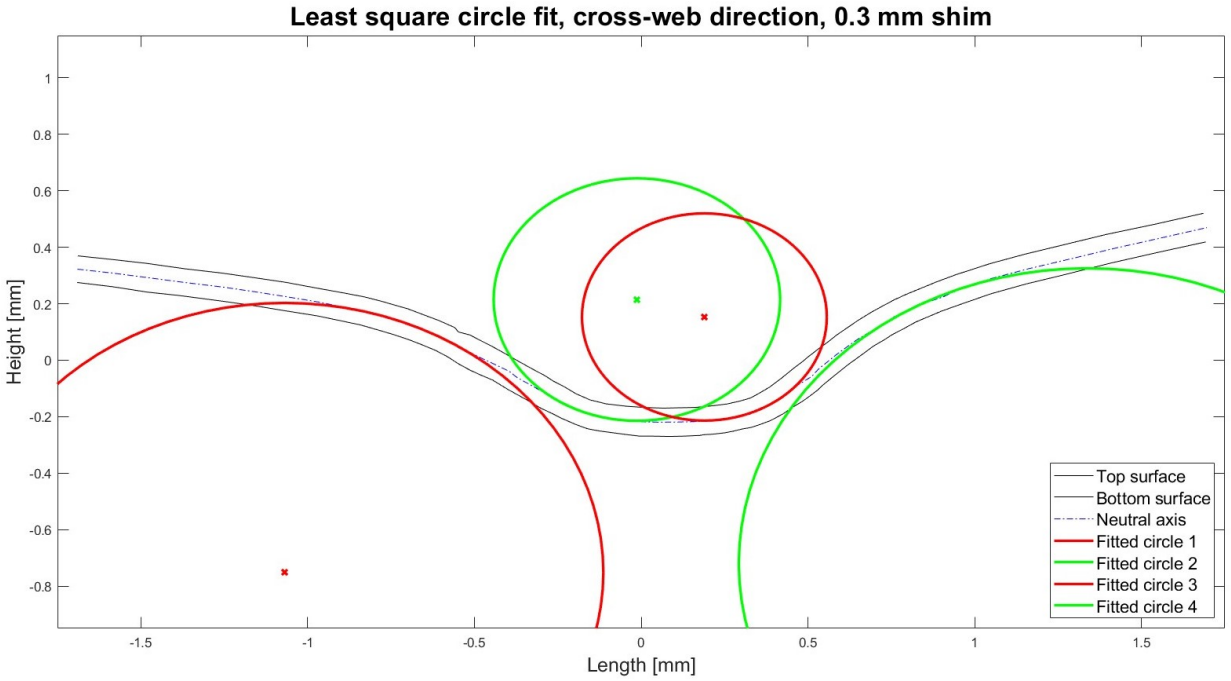

Figure B.5: *Bending strain measurement, cross-web, 0.3 mm shim.*

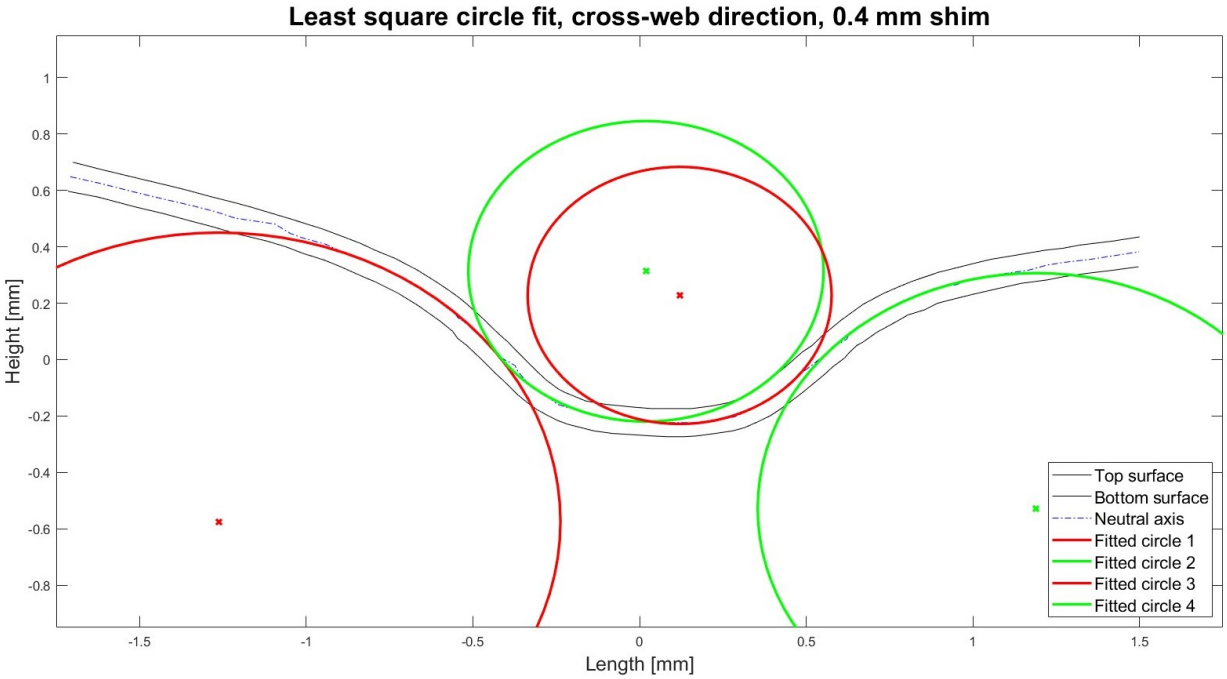

Figure B.6: *Bending strain measurement, cross-web, 0.4 mm shim.*

Table B.4: *Bending radii and strain results for cross-web and 0.2 mm shim.*

# [-]	y $[mm]$	r $[mm]$	ε_{ben} [-]	$interval$ [-]	# $points$ [-]
1	0.0486	0.582	0.083	(-0.8; -0.5)	7
2	0.0471	0.476	-0.099	(-0.4; 0.0)	13
3	0.0474	0.408	-0.116	(0.15; 0.4)	7
4	0.0491	1.071	0.046	(0.75; 1.0)	4

Table B.5: *Bending radii and strain results for cross-web and 0.3 mm shim.*

# [-]	y $[mm]$	r $[mm]$	ε_{ben} [-]	$interval$ [-]	# $points$ [-]
1	0.0487	0.955	0.051	(-0.9; -0.5)	10
2	0.0487	0.430	-0.113	(-0.3; 0.0)	7
3	0.0482	0.367	-0.131	(0.15; 0.45)	10
4	0.0489	1.045	0.047	(0.65; 1.1)	8

Table B.6: *Bending radii and strain results for cross-web and 0.4 mm shim.*

# [-]	y $[mm]$	r $[mm]$	ε_{ben} [-]	$interval$ [-]	# $points$ [-]
1	0.0492	1.025	0.048	(-0.9; -0.55)	7
2	0.0486	0.533	-0.091	(-0.5; 0.05)	14
3	0.0488	0.456	-0.107	(0.0; 0.5)	13
4	0.0493	0.835	0.059	(0.55; 1.1)	15

C | Shape comparison

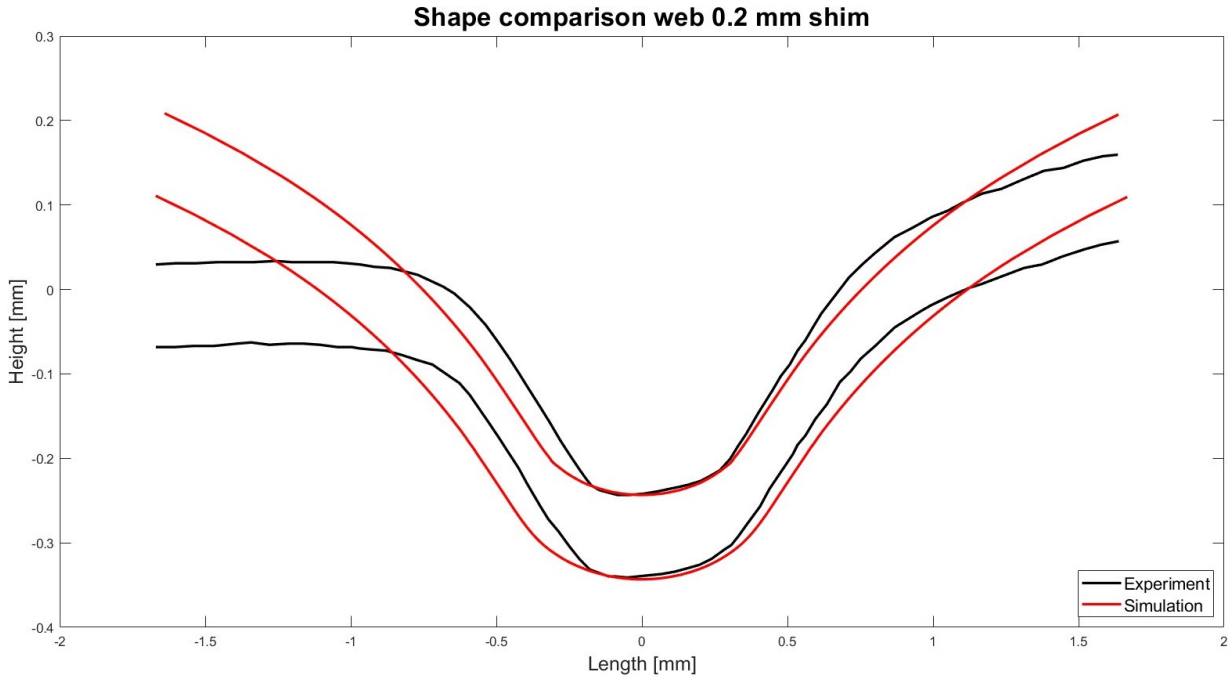

Figure C.1: *Shape comparison, web, 0.2 mm shim.*

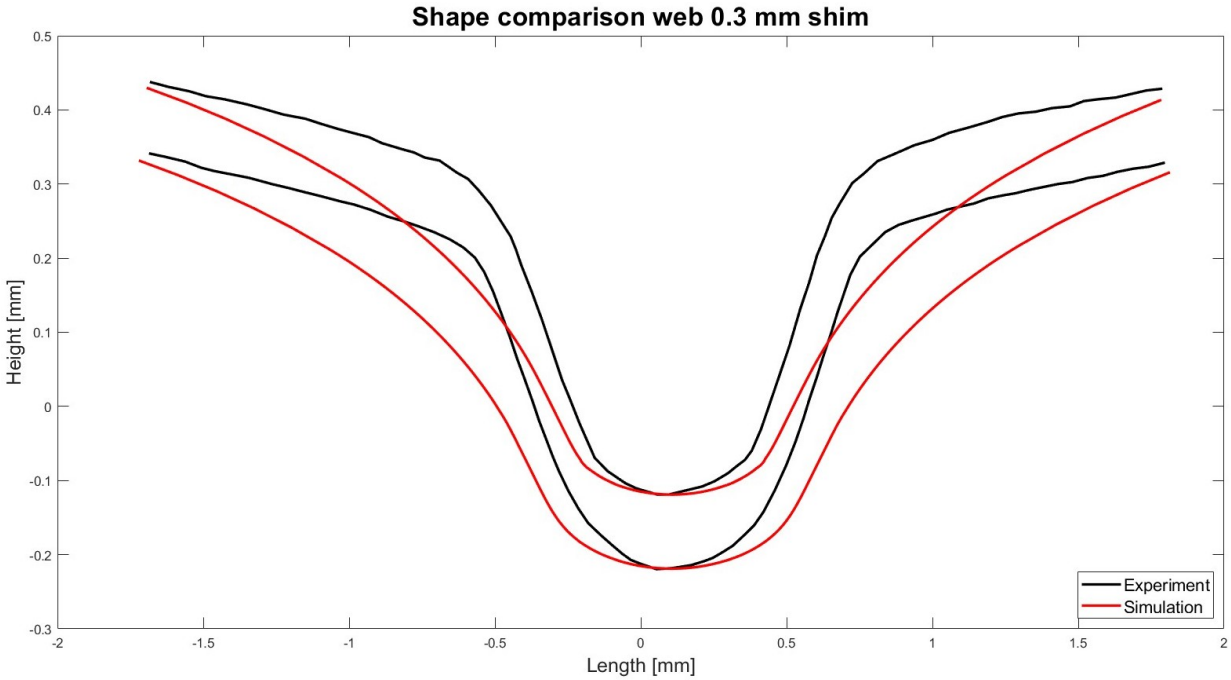

Figure C.2: *Shape comparison, web, 0.3 mm shim.*

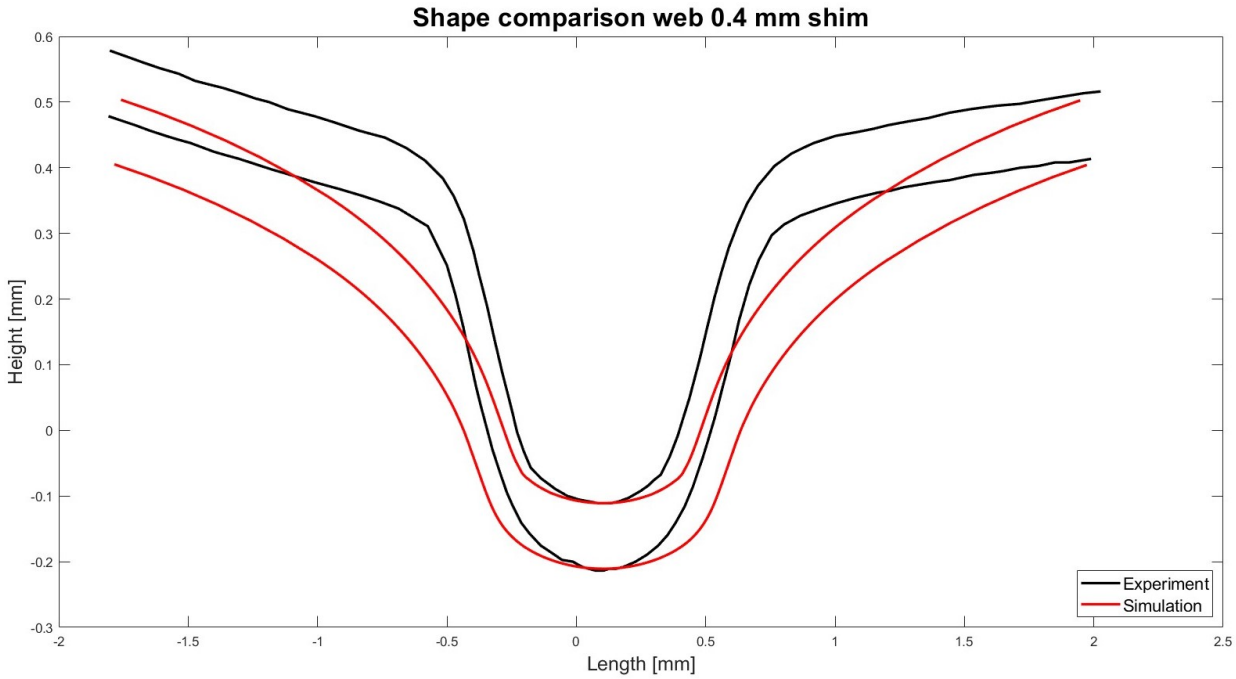

Figure C.3: *Shape comparison, web, 0.4 mm shim.*

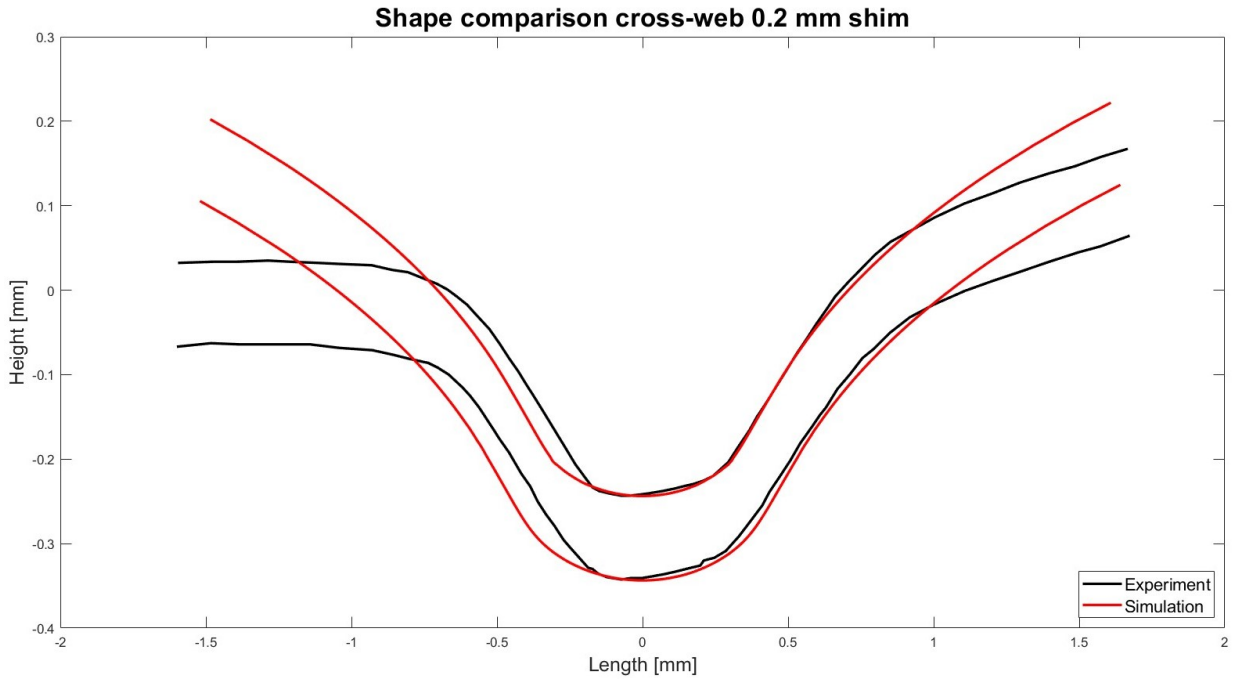

Figure C.4: *Shape comparison, cross-web, 0.2 mm shim.*

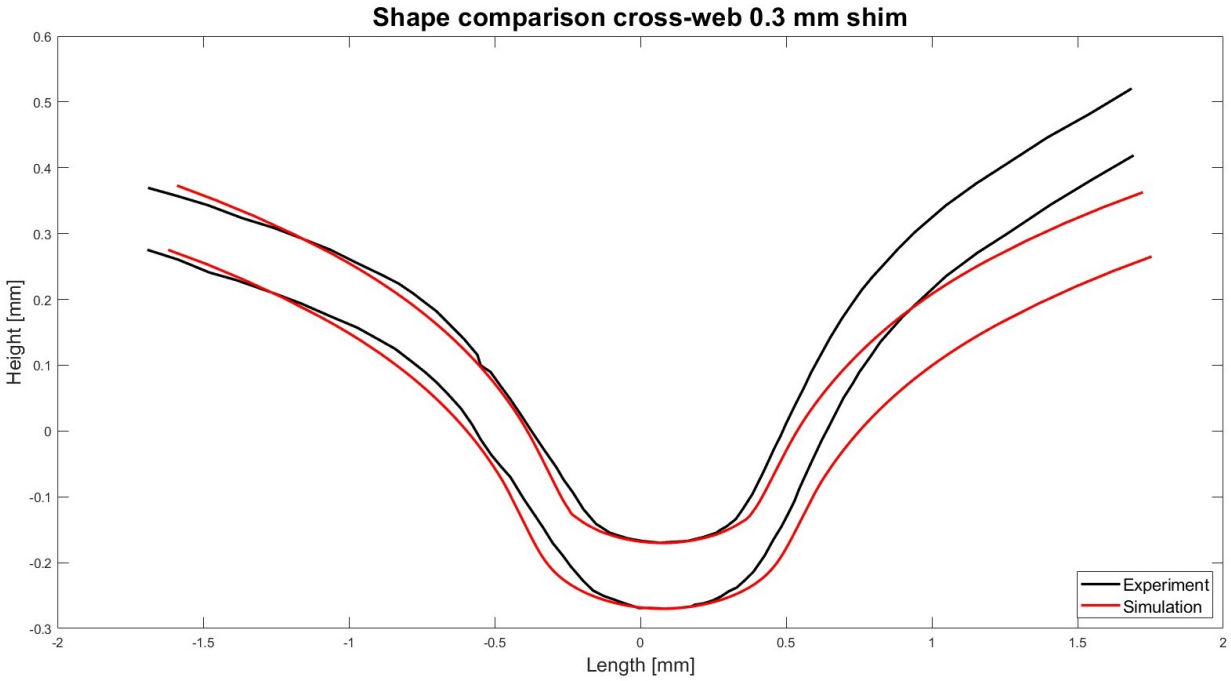

Figure C.5: *Shape comparison, cross-web, 0.3 mm shim.*

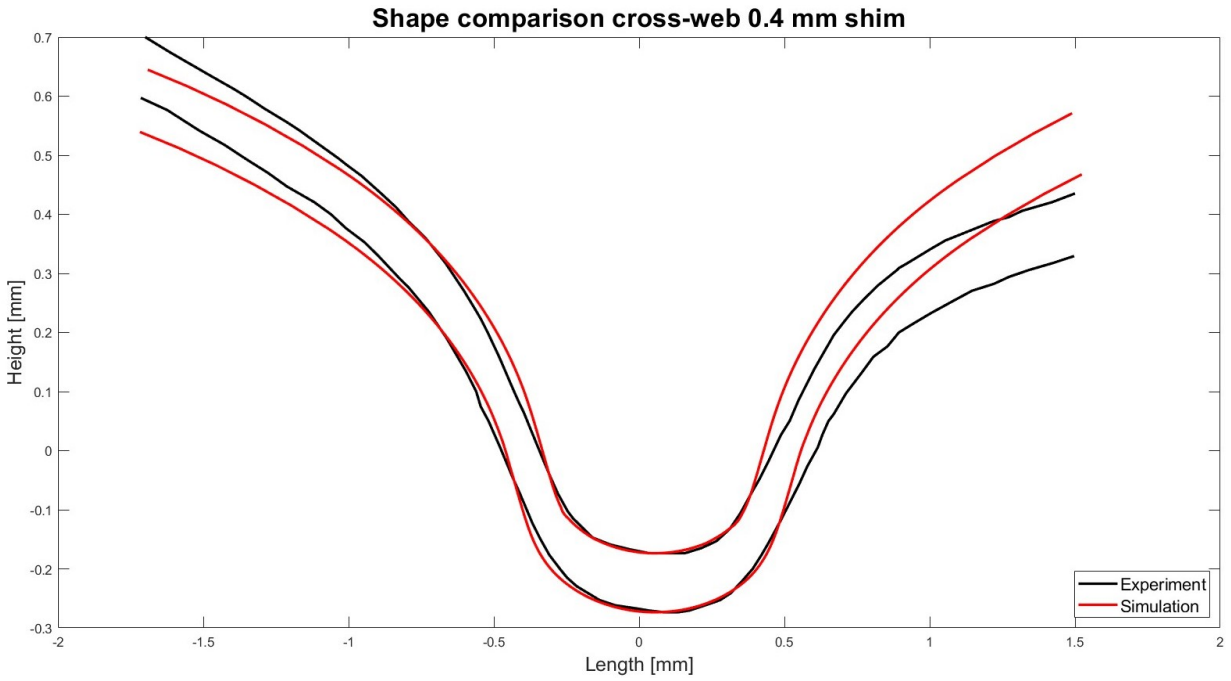

Figure C.6: *Shape comparison, cross-web, 0.4 mm shim.*

D | Springback comparison

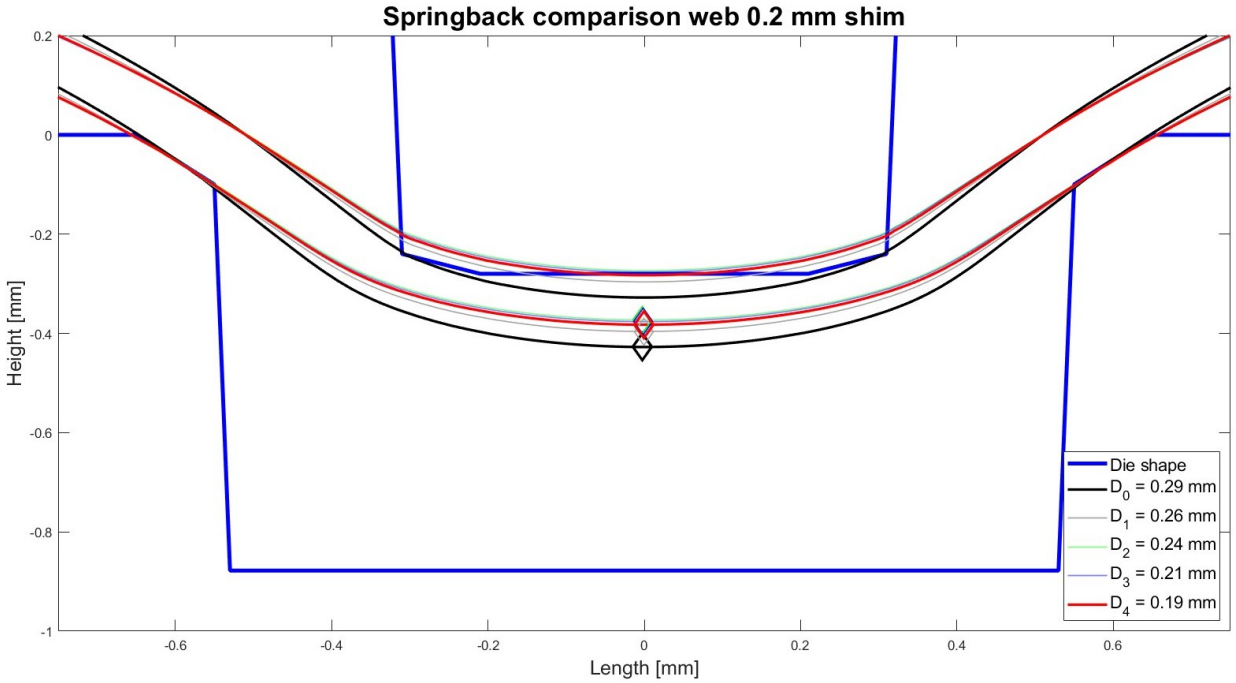

Figure D.1: *FEA springback comparison, web, 0.2 mm shim.*

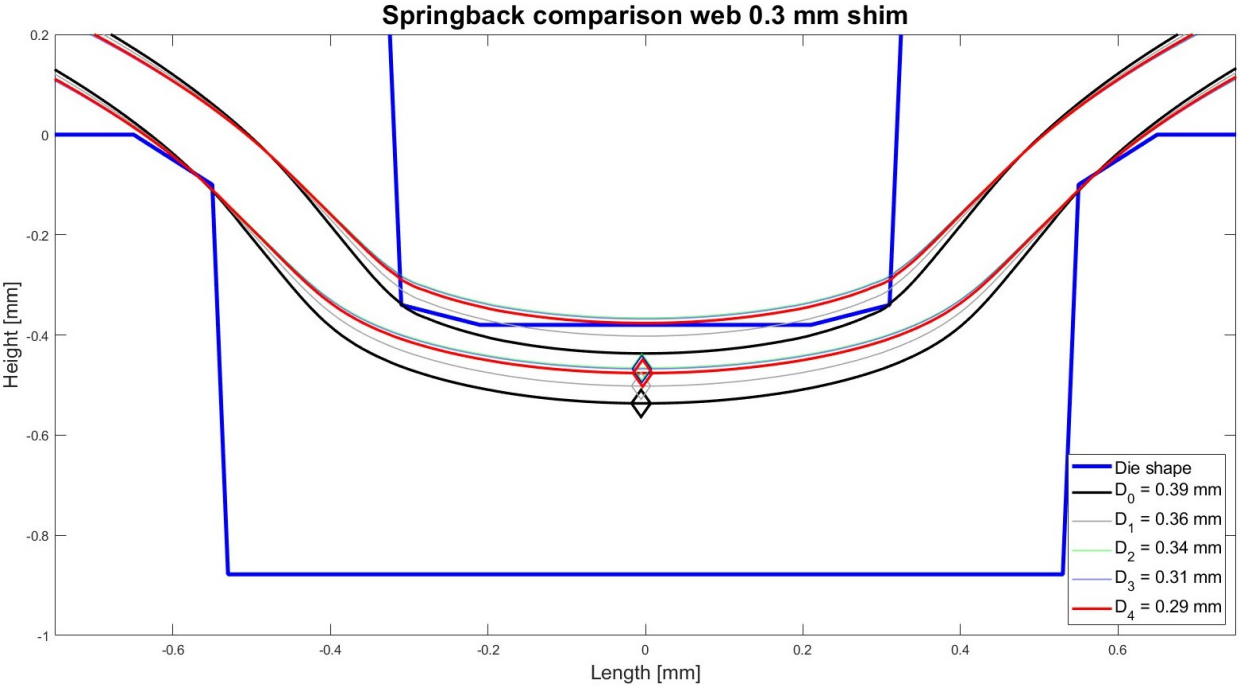

Figure D.2: *FEA springback comparison, web, 0.3 mm shim.*

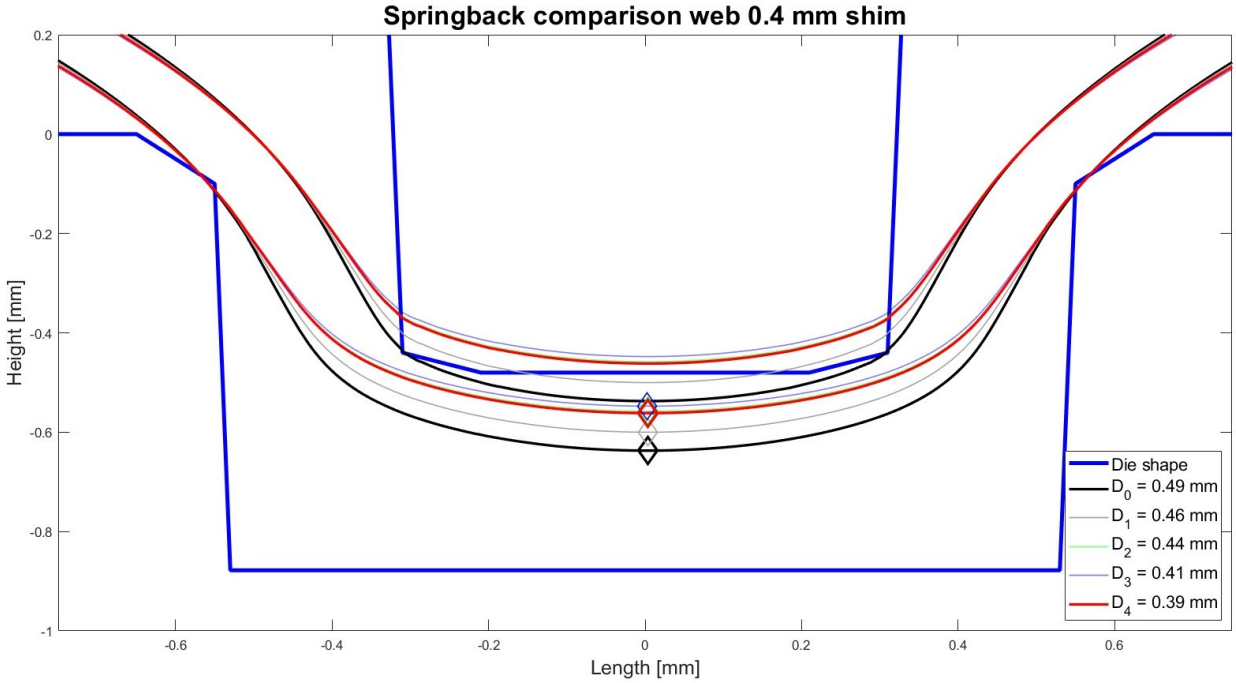

Figure D.3: *FEA springback comparison, web, 0.4 mm shim.*

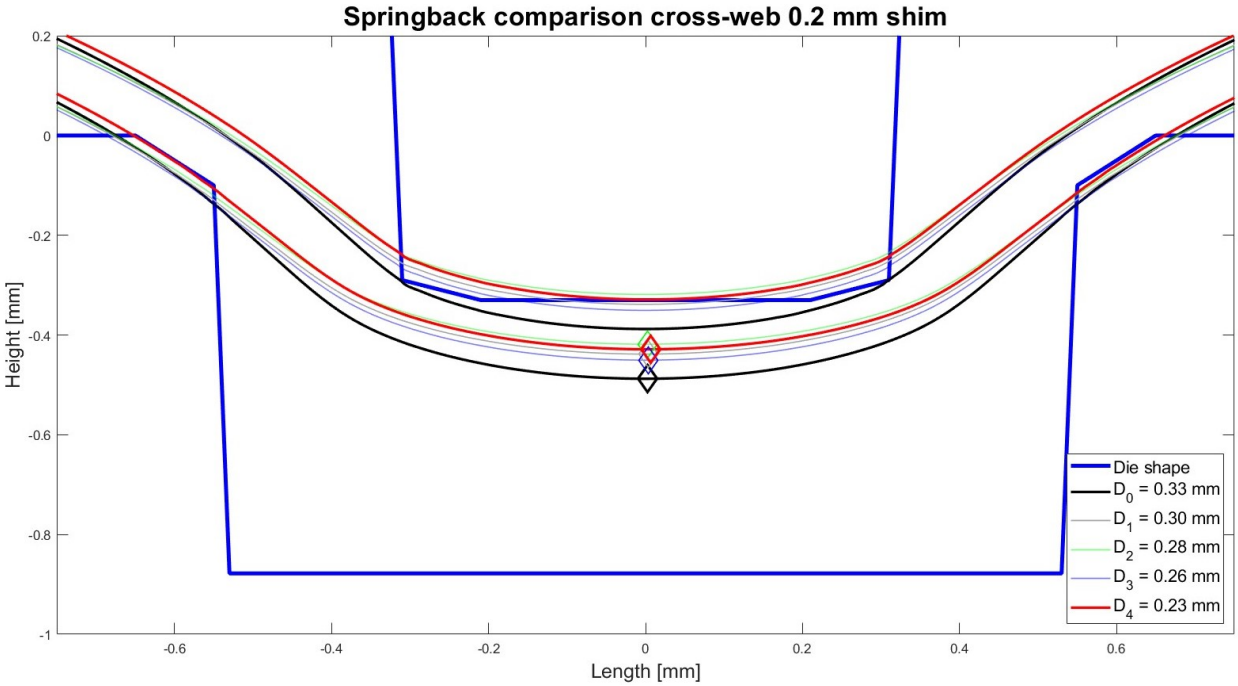

Figure D.4: *FEA springback comparison, cross-web, 0.2 mm shim.*

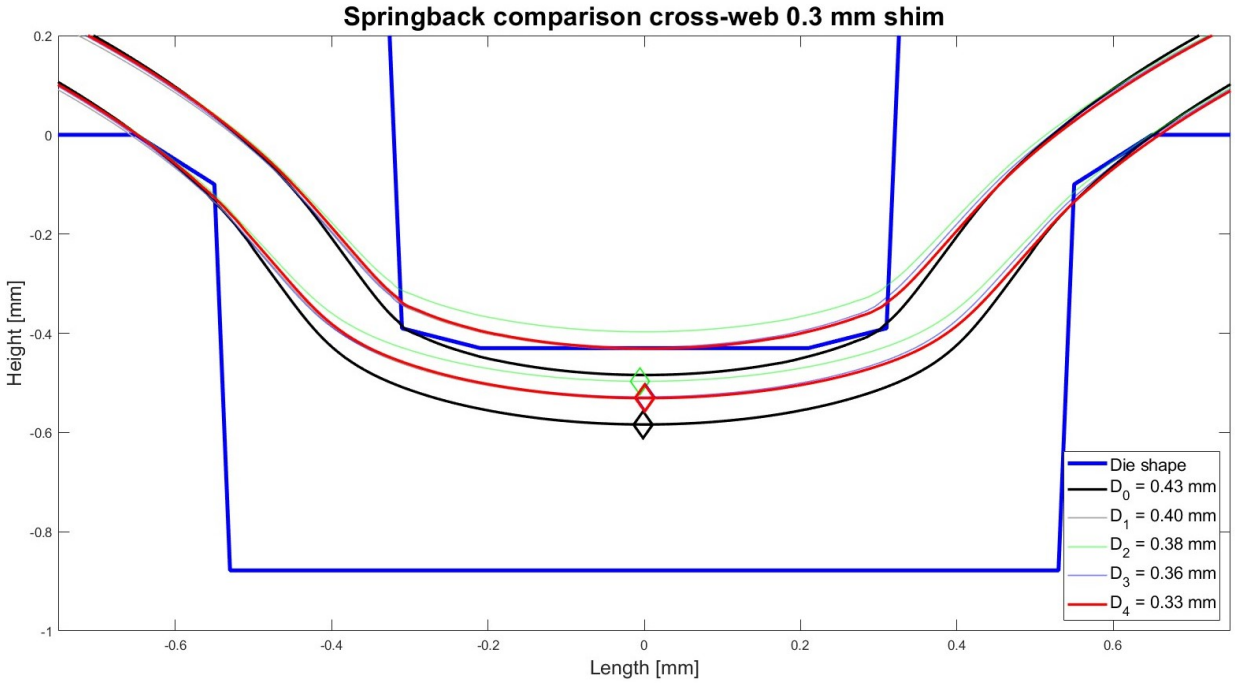

Figure D.5: *FEA springback comparison, cross-web, 0.3 mm shim.*

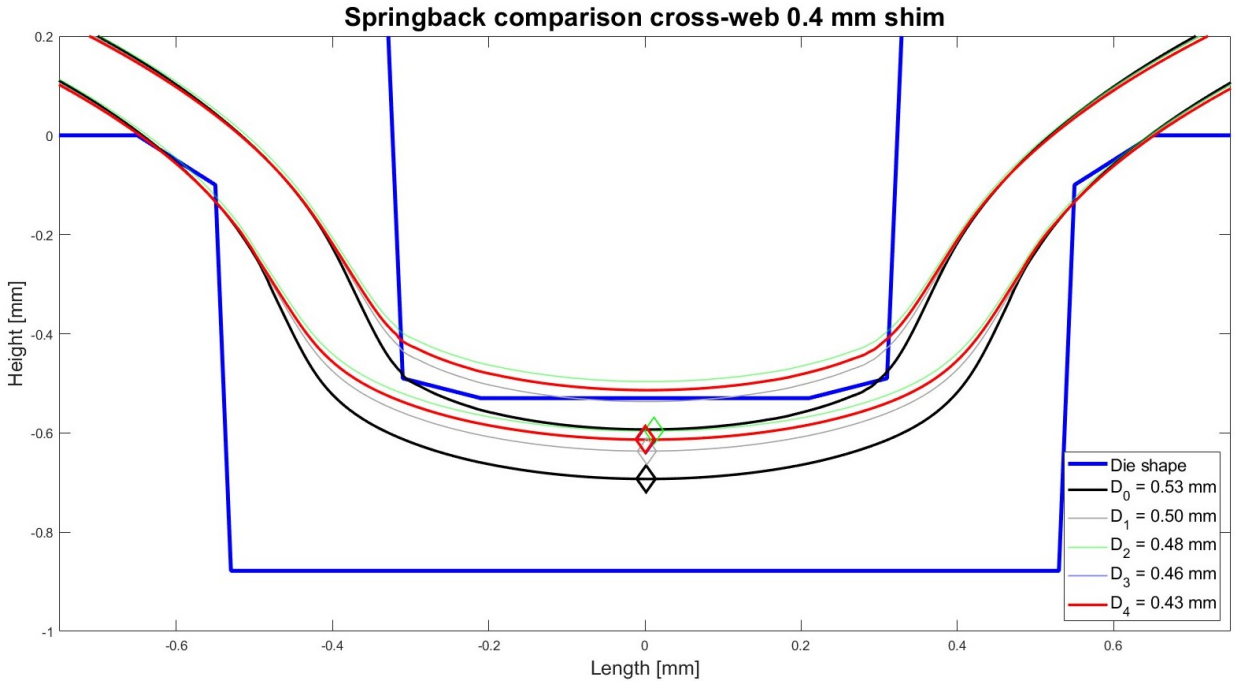

Figure D.6: *FEA springback comparison, cross-web, 0.4 mm shim.*

Bibliography

Abeyrathna, B., Zhang, P., Pereira, M. P., Wilkosz, D., & Weiss, M. (2019). Micro-roll forming of stainless steel bipolar plates for fuel cells. *International journal of hydrogen energy*, *44*(7), 3861–3875. https://doi.org/10.1016/j.ijhydene.2018.12.013

Ahn, S. J., Rauh, W., & Warnecke, H.-J. (2001). Least-squares orthogonal distances fitting of circle, sphere, ellipse, hyperbola, and parabola. *Journal of the Pattern recognition society*, *34*, 2283–2303. https://doi.org/10.1016/S0031-3203(00)00152-7

ASTM E 8M-04. (2022). *Standard Test Methods for Tension Testing of Metallic Materials*, (ASTM International). https://doi.org/10.1520/E0008_E0008M-21

ASTM E290-14. (2019). *Standard Test Methods for Bend Testing of Material for Ductility*, (ASTM International). https://doi.org/10.1520/E0290-14

Badulescu, C., Grédiac, M., Mathias, J. D., & Roux, D. (2009). A procedure for accurate one-dimensional strain measurement using the grid method. *Experimental Mechanics*, *49*, 841–854. https://doi.org/10.1007/s11340-008-9203-8

Banabic, D., Bunge, H. J., Pohlandt, K., & Tekkaya, A. E. (2000). Formability of metallic materials. In D. Banabic (Ed.), *Plastic anisotropy, formability testing, forming limits* (1st). Springer-Verlag Berlin Heidelberg. https://doi.org/10.1007/978-3-662-04013-3

Bauer, A., Härtel, S., & Awiszus, B. (2019). Manufacturing of metallic bipolar plate channels by rolling. *Manufacturing and Materials Processing*, *48*(2). https://doi.org/10.3390/jmmp3020048

Berning, T., & Djilali, N. (2003). Three-dimensional computational analysis of transport phenomena in a pem fuel cell - a parametric study. *Journal of Power Sources*, *124*, 440–452. https://doi.org/10.1016/S0378-7753(03)00816-4

Burgan, B. (2001). *Elevated temperature and high strain rate properties of offshore steels.* HSE Offshore Technology Report 020, Steel Construction Institute.

Carden, W. D., Geng, L. M., Matlock, D. K., & Wagoner, R. H. (2002). Measurement of springback. *International Journal of Mechanical Sciences*, *44*(1), 79–101. https://doi.org/10.1016/S0020-7403(01)00082-0

Chikalthankar, S. B., Belurkar, G. D., & Nandedkar, V. M. (2014). Factors affecting on springback in sheet metal bending: A review. *International Journal of Engineering and Advanced Technology*, *3*(4), 249–251.

Cowper, G. R., & Symonds, P. S. (1957). Strain hardening and strain rate effects in the impact loading of cantilever beams. *Division of Applied Mathematics Brown University Providence, R. I.*

Demeri, M. Y. (1981). The stretch-bend forming of sheet metal. *Journal of Applied Metalworking*, *2*(1), 3–10. https://doi.org/10.1007/BF02833993

Elyasi, M., Khatir, F. A., & Hosseinzadeh, M. (2017). Manufacturing metallic bipolar plate fuel cells through rubber pad forming process. *The International Journal of Advanced Manufacturing Technology*, *89*, 3257–3269. https://doi.org/10.1007/s00170-016-9297-6

Erichsen, A. M. (1914). A new test for thin sheets (in german). *Stahl und Eisen*, *34*, 879–882.

Fu, C., Wang, T., Xu, F., Huo, Y., & Potier-Ferry, M. (2019). A modeling and resolution framework for wrinkling in hyperelastic sheets at finite membrane strain. *Journal of the Mechanics and Physics of Solids*, *124*, 446–470. https://doi.org/10.1016/j.jmps.2018.11.005

Gan, W., & Wagoner, R. H. (2004). Die design method for sheet springback. *International Journal of Mechanical Sciences*, *46*(1), 1097–1113. https://doi.org/10.1016/j.ijmecsci.2004.06.006

Gu, Z.-w., Lü, M.-m., Li, X., & Xu, H. (2016). Stretch bending of z-section stainless steel profile. *Journal of Iron and Steel Research International*, *23*, 525–530. https://doi.org/10.1016/S1006-706X(16)30083-8

Haroush, S., Priel, E., Moreno, D., Busiba, A., Silverman, I., Turgeman, A., Shneck, R., & Gelbstein, Y. (2015). Evaluation of the mechanical properties of ss-316l thin foils by small punch testing and finite element analysis. *Materials and Design*, *83*, 75–84. https://doi.org/10.1016/j.matdes.2015.05.049

H.Chen, W. (1971). Necking of a bar. *International Journal of Solids and Structures*, *7*(7), 685–717. https://doi.org/10.1016/0020-7683(71)90088-6

Hibbeler, R. (2010). *Mechanics of materials* (8th edition). Pearson Prentice Hall.

Hwang, D., Kim, J.-Y., Kim, H.-S., & Lee, M. G. (n.d.). Novel stage with voice coil motor for laser beam direct writing.

James, B. D., Huya-Kouadio, J. M., Houchins, C., & DeSantis, D. A. (2018). *Mass production cost estimation of direct h_2 pem fuel cell systems for transportation applications* (Vol. 2018 update). Strategic Analysis Inc.

Langdon, G. S., & Schleyer, G. K. (2004). Unusual strain rate sensitive behaviour of aisi 316l austenitic stainless steel. *Journal of Strain Analysis for Engineering Design*, *39*(1), 71–86. https://doi.org/10.1177/030932470403900106

Ling, Y. (1996). Uniaxial true stress-strain after necking. *AMP Journal of technology*, *5*(1), 37–48.

Mäntyjärvi, K., Tulonen, J., Saarnivuo, T., Porter, J., & Karjalainen, J. A. (2008). Grid patterns by laser for forming strain analysis. *International Journal of Material Forming*, *1*, 249–252. https://doi.org/10.1007/s12289-008-0355-y

Marciniak, Z., Duncan, J. L., & Hu, S. J. (2002). *Mechanics of sheet metal forming* (Second edition). Butterworth-Heinemann.

Marques, T. J. C. R. D. (2015). *Investigation of the grid methods for accurate strain measurement* (Master's thesis). Instituto Superior Técnico Lisboa.

Metha, V., & Smith-Cooper, J. (2003). Review and analysis of pem fuel cell design and manufacturing. *Journal of Power Sources*, *114*(1), 32–53. https://doi.org/10.1016/S0378-7753(02)00542-6

Middelman, E., Kout, W., Vogelaar, B., Lenssen, J., & de Waal, E. (2003). Bipolar plates for pem fuel cells. *Journal of Power Sources*, *118*, 44–46. https://doi.org/10.1016/S0378-7753(03)00070-3

Narayan, L. R. (2012). *Forming of ferritic stainless steel bipolar plates* (Master's thesis). University of Windsor.

Pollet, B. G., Franco, A. A., Su, H., Liang, H., & Pasupathi, S. (2016). *Compendium of hydrogen energy (chapter 1: Proton exchange membrane fuel cells)* (Vol. 3: Hydrogen Energy Conversion). Woodhead Publishing. https://doi.org/10.1016/B978-1-78242-363-8.00001-3

Porstmann, S., Wannemacher, T., & Drossel, W. G. (2020). A comprehensive comparison of state-of-the-art manufacturing methods for fuel cell bipolar plates including anticipated future industry trends. *Journal of Manufacturing Processes*, *60*, 366–383. https://doi.org/10.1016/j.jmapro.2020.10.041

Sciammarella, C. A., & Kim, T. (2003). Determination of strains from fringe patterns using space-frequency representations. *Optical engineering*, *42*(11), 3182–3193. https://doi.org/10.1117/1.1613276

Shi, B. Q., & Liang, J. (2012). Circular grid pattern based surface strain measurement system for sheet metal forming. *Optics and Lasers in Engineering*, *50*(9), 1186–1195. https://doi.org/10.1016/j.optlaseng.2012.04.007

Sirkis, J. S., & Lim, T. J. (1991). Displacement and strain measurement with automated grid methods. *Experimental Mechanics*, *31*, 382–388. https://doi.org/10.1007/BF02325997

TA Instruments Thermal Analysis. (2010). *DMA Q800 Specifications*. https://tainstruments.com.cn/wp-content/uploads/dma.pdf

Talebi-Ghadikolaee, H., Barzegari, M. M., Khatir, F. A., & Seddighi, S. (2022). Numerical-experimental study on the thickness distribution of metallic bipolar plates for pem fuel cells. *Iranian Journal of Hydrogen and Fuel Cell*, *1*, 1–18. https://doi.org/10.22104/IJHFC.2021.5217.1230

Trzepiecinski, T., & Lemu, H. G. (2017). Effect of computational parameters on springback prediction by numerical simulation. *Metals*, *7*(9), 380. https://doi.org/10.3390/met7090380

Tsuchiya, H., & Kobayashi, O. (2004). Mass production cost of pem fuel cell by learning curve. *International Journal of Hydrogen Energy*, *29*(10), 985–990. https://doi.org/10.1016/j.ijhydene.2003.10.011

Ueda, M., Ueno, K., & Kobayashi, M. (1981). A study of springback in the stretch bending of channels. *Journal of Mechanical Working Technology*, *5*(3-4), 163–179. https://doi.org/10.1016/0378-3804(81)90038-3

Vishnyakov, V. M. (2006). Proton exchange membrane fuel cells. *Vacuum*, *80*(10), 1053–1065. https://doi.org/10.1016/j.vacuum.2006.03.029

Wang, C., Wang, H., Chen, G., Zhu, Q., Zhang, P., & Fu, M. W. (2022). Experiment and modeling based studies of the mesoscaled deformation and forming limit of cu/ni clad foils using a newly developed damage model. *International Journal of Plasticity*, *149*(103173). https://doi.org/10.1016/j.ijplas.2021.103173

Wang, Y., Diaz, D. F. R., Chen, K. S., Wang, Z., & Adroher, X. C. (2020). Materials, technological status, and fundamentals of pem fuel cells – a review. *Materialstoday*, *32*, 178–203. https://doi.org/10.1016/j.mattod.2019.06.005

Wilberforce, T., Hassan, Z. E., Ogungbemi, E., Ijaodola, O., Khatib, F., Durrant, A., Thompson, J., Baroutajib, A., & Olabi, A. (2019). A comprehensive study of the effect of bipolar plate (bp) geometry design on the performance of proton exchange membrane (pem) fuel cells. *Renewable and Sustainable Energy Reviews*, *111*, 236–260. https://doi.org/10.1016/j.rser.2019.04.081

Zhang, P., Pereira, M., Rolfe, B., Daniel, W., & Weiss, M. (2017). Deformation in micro roll forming of bipolar plate. *Journal of Physics: Conference Series*, *896*. https://doi.org/10.1088/1742-6596/896/1/012115